UNIVERSITÀ
DEGLI STUDI
FIRENZE

DOTTORATO DI RICERCA IN
Scienze Chimiche

CICLO XXVII

Massimo Manuelli

Magnetic Nanoparticles as a multivalent scaffold for biomedical applications

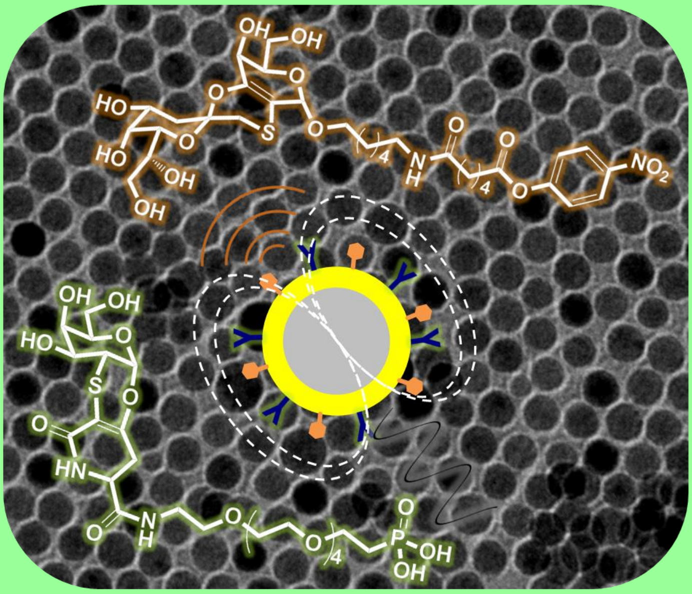

Anni 2012/2014

Index

1. Introduction 1

2. Synthesis of MNPs 16

2.1 Synthesis with FeOOH 17

2.2 Synthesis with iron(III) oleate 22

2.3 Synthesis of magnetite MNPs with Iron Acetylacetonate 31

2.3.1 Synthesis of MNPs exploiting the seed mediated growth process 32

2.3.2 Synthesis of larger magnetite MNPs from iron(III) acetylacetonate 38

3. The α-Tn antigen mimetic and functionalization of MNPs 49

3.1 The α-Tn antigen 49

3.2 Synthesis of the α-Tn antigen mimetic **2** 51

3.3 Synthesis of the linker **5** 57

3.4 Synthesis of the α-Tn like derivative 3 : coupling reaction and phosphonate insertion. 58

3.5 Functionalization of MNPs with the α-Tn antigen mimetic **3** 59

4. Synthesis of negative control for biological tests for macrophage activation 65

4.1 Synthesis of the glucose derivative for MNPs functionalization 66

4.2 Functionalization of MNPs with citrate, glucose and PEG 70

5. Macrophages activation 77

5.1 Macrophages role in the immune response 77

5.2 Biological tests 80

6. Functionalization of MNPs 90

6.1 Aminosilane functionalization 92

6.2 Synthesis of aminophosphonic linker **39** 97

7. Conclusion and perspectives 102

8. Experimental section 105

8.1 Synthesis of MNPs 106

8.2 Functionalization of MNPS 109

8.3 Synthesis of linker **5** 112

8.4 Synthesis of α-Tn antigen mimetic **3** 113

8.5 Synthesis of glucose derivative **24** 122

8.6 Synthesis of amino-phosphonate linker **39** 126

8.7 Biological tests on macrophages activation 130

8.8 Structural characterization of MNPs 134

8.9 Magnetic and hyperthermic characterization 135

8.10 Characterization of organic compounds 137

1. Introduction

The reduction of materials to the nanometric size, in the last decades has been the focus of intense research. Indeed, nanomaterials possess attractive properties which can be used, and in some cases are already in use, in many field of applications: catalysis, data storage, sensors and biomedicine [1]. In particular, the application of nanomaterials in biology and medicine is receiving considerable attention, as they hold great promises on improving health care and advancing medical research [2].

Among the others, magnetic nanoparticles (MNPs) with size below 100 nm represent one of the most promising class of materials, thanks to their peculiar properties. The first prominent feature which makes magnetic *nano-objects* appealing for biomedical applications is represented by their controllable sizes ranging from few nanometres up to tens of nanometres, which are smaller or comparable to those of many biological entities, ranging from a single gene (2 nm wide and 10-100 nm long) to an entire cell (10-100 µm). The possibility of a interaction between such entities at the nanometric scale has progressively attracted the attention of many research groups all over the world [2a-b]. Beside their size, the importance of MNPs in the field of biomedicine relies on their specific properties, the most significant being superparamagnetism [3]. When ferro- or ferrimagnetic particles belong to the nanometric size range they become single domain, i.e. the formation of magnetic domains is no longer energetically favoured, therefore they are characterized by a single magnetic moment given by the sum of all the atomic spins comprised in the nanoparticle [4]. This magnetic moment will freely fluctuate like in a paramagnet (superparamagnetism) or will be blocked along certain favoured crystallographic directions (ferromagnetic-like behaviour) depending on whether the thermal energy is larger or smaller than the energy barrier separating that directions. This energy barrier is determined by the magnetic anisotropy of the material itself and, as a first approximation, is proportional to the volume of the MNPs [3].

These outstanding properties confer to MNPs unique sensing, moving and heating characteristic which can be exploited for bio-analysis or for the early diagnosis and therapy of several diseases.

It is worthy of noting that for biomedical application, biocompatibility is another mandatory requirement, restricting the choice for the inorganic core of the MNPs to iron oxides and in particular magnetite or maghemite [5].

At present, most applications of MNPs are based on the following physical principles [1a, 2b]:

- the application of controlled magnetic field gradients for remotely direct MNPs towards organs or tissues or for moving MNPs tagged biomaterials;
- the utilization of the magnetic moment of the MNPs to modify the nearby proton nuclear resonance (contrast agent (CA) for Magnetic Resonance Imaging (MRI));
- the excitation of MNPs with an external alternating magnetic field inducing an heat release which can be used to selectively destroy tumour cells, exploiting their higher sensitivity to a temperature increase than healthy tissues (magnetic fluid hyperthermia, MFH).

For example, MNPs can help in the separation of selected biological entities from their native environment, so that concentrated samples may be prepared for subsequent analyses or other uses. This process involves two steps: 1) the tagging or labelling of the desired biological entity with the magnetic material and 2) the separation of these tagged entities *via* a fluid-based magnetic separation device. The tagging is possible by coating MNPs with suitable functional groups which in turn can provide a selective linkage to the target site exposed by a cell or a molecule, and at the same time maintain an optimal colloidal stability. A specific binding to the target can be achieved by using antibodies or other biological macromolecules such as hormones or folic acid [6,2b]. The magnetically labelled material can be then separated from its native solution by passing the fluid mixture through a region in which a magnetic field gradient is present, so that the tagged material is immobilized while the unwanted material is removed, as displayed in Figure 1.1.

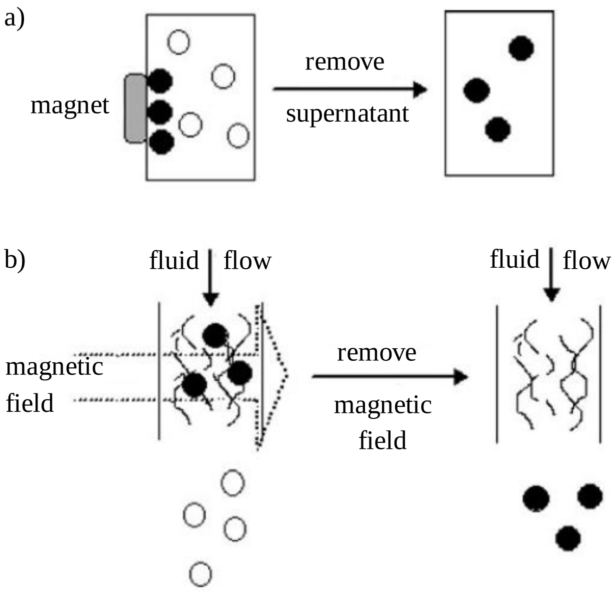

Figure 1.1 : Standard methods for magnetic separation: a) the magnet is attached to the container wall of a solution of magnetically tagged (●) and unwanted (○) biomaterials. b) a solution containing tagged and unwanted biomaterials flows continuously through a region of strong magnetic field gradient, which captures the tagged particles.

In the field of sensing, MRI, is the area in which MNPs have found their major application, since they are capable of enhancing the contrast of the image (contrast agents). MRI provides images of the density distribution of protons or other nuclei through the application of appropriate magnetic field gradients and radiofrequency pulse sequences. MRI exploits the contrast created by different nuclear spin-spin (T2) and spin-lattice (T1) relaxation times found in different parts of the material to obtain images that can evidence specific differences [7]. This technique is widely used in medical clinic to investigate the anatomy and physiology of the body. From the obtained images it is possible to evidence local pathologies and disease like tumour lesions, edemas, soft tissue damages, muscle lesions and many more.

Contrast agents are used in order to increase the natural contrast between healthy and pathological tissues and they normally act decreasing the relaxation times, T1 and T2, of the neighbour protons. At present, the most used CAs are based on paramagnetic gadolinium complexes, [8] which increase the contrast by decreasing T1 [8]. However, CAs based on dextran coated assembly of superparamagnetic maghemite nanoparticles with a total average diameter between 20 and 150 nm are also commercially available. In Table 1.1 some examples of clinically approved CA for MRI are reported [9].

Generic Name	Metal	Trade Name
Ferumoxides	Fe_3O_4	Endorem®, Fedirez®
Ferumoxyl	Fe_3O_4	Lumirem®, GastroMARK
Ferucarbotran	Fe_3O_4	Resovist®
Ferumoxtran	Fe_3O_4	Sinerem®, Combidex®

Table 1.1 : Clinically approved CA for MRI based on magnetite nanoparticles [9a].

Ferrite MNP based CAs perform their function affecting the T2 relaxation time of the protons in the nearby tissues, leading to a better contrast in the acquired images. The advantages offered by MNPs-based CA, in comparison with conventional gadolinium chelates, rely on the enhanced cellular internalization and slower clearance from tumour site [10]. In particular, for MNPs with diameters greater than 50 nm the cellular internalization is essentially due to the uptake by the cells of the reticuloendothelial system (RES), whereas nanoparticles with a diameter lower than 50 nm benefit from slower opsonization and RES clearance [11]. In all of these cases the tissue distribution of the MNPs relies on a passive targeting rather than a direct labelling. Indeed, one of the most challenging opportunities is to functionalize the nanoparticles with specific biomolecules (monoclonal antibodies, peptides, or other target bioactive molecules) in order to direct the CA only to the desired target exploiting a receptor-mediated endocytosis and hence increasing a local accumulation in the diseased tissues [12]. This would allows both the increase of the sensitivity of the technique and the reduction of the amount of contrast agent required to acquire an MRI image.

Finally, MNPs can be used as heat mediators in the hyperthermic treatment of tumour cells, which is a technique that is progressively acquiring more and more relevance in the fight against tumour pathologies [2a,2b]. Hyperthermia is a general term which groups together several techniques, all based on the rise of temperature above the physiologic level (in the range of 40-45°C) within a targeted tumour without damaging the surrounding healthy tissues [9a]. The most extended method for increasing temperature above the systemic values is based on the application of microwaves [13], although therapies involving ionizing radiation [14] have also been successfully applied to destroy malignant tissues. The disadvantages of these strategies are related to undesired collateral effects such as ionization of genetic material (radiation) or lack of selectiveness (microwaves) that affect the surrounding healthy tissues [15]. Another emerging hyperthermic treatment of tumours relies on the application of a radiofrequency on magnetic needles directly implanted into the target site [16.]; although very promising, this technique is invasive and its effectiveness is rather limited.

In this respect inorganic nanoparticles, which, in principle can be localized only at the tumour site, can represent a viable alternative. For example, successful *in vitro* and *in vivo* studies have been reported on the use of functionalized gold nanorods to convert infrared radiation (IR) into heat that selectively destroys cancer cells [17]. The use of these kind of nanostructures for hyperthermia could be useful to avoid damages on healthy cells. On the other hand, IR radiation has a low penetration depth into human tissues, which limits this technique to surface applications, like melanoma cells [9a]. The employment of MNPs as heat mediators for MFH can help to overcome these drawbacks. In this case the temperature increasing is realized by means of an external alternating magnetic field acting on MNPs at the targeted site, which provides to the particle's magnetic moment the energy required to overcome the barrier generated by the magnetic anisotropy. This energy is then released as heat which is dissipated to the surrounding tissues. MNPs can be accumulated in tumour tissues thanks to the so called enhance permeability and retention (EPR) effect [18]. This mechanism relies on leaky vasculature characterizing cancerous tissues, which allows macromolecules and nanoparticles to extravasate and accumulate more readily. This passive targeting can be exploited to induce a local temperature enhancement and, as a consequence to selectively induce tumour cells death. The feasibility of MFH has been already demonstrated in clinical trials by the group of Prof. Jordan at Berlin's Charité Hospital, who reported significant benefits in the treatment of recurrent glioblastoma multiforme and, more recently of prostate and pancreas tumours by using a combination of radiotherapy and heating produced by 12 nm amino-silane coated Fe_3O_4 MNP directly implanted in the tumour mass at high doses (ca. 50 mg/cm^3) [19]. As it can be inferred from the above description, an improvement of the hyperthermic treatment can be accomplished by the use of tumour targeted MNPs in order to increase the selectivity and reach the temperature enhancement with as low as possible amount of MNPs. Furthermore hyperthermia can be used in combination with other cancer therapies like chemotherapy and radiotherapy so as to increase their efficacy during the treatment. Moreover, chemotherapeutic drugs can be eventually linked to the MNPs used for the hyperthermic treatment and released only at the target site [9a, 1a].

We have described the appealing properties offered by MNPs that can be exploited in the field of biomedicine and, in particular, in the treatment and diagnosis of tumour pathologies. However, the most attracting feature is that all the above cited functionalities, i.e. sensing, moving and heating, can be combined in a unique multifunctional nano-object which ideally can ensure early diagnosis, deliver of the treatment to the specific target site at the right dose and time, and monitoring of the therapeutic effect. This kind of system will thus work as a diagnostic tool and as therapeutic agent, paving the way towards the so-called theranostic approach (therapeutic + diagnostic). In Figure 1.2 is provided a schematic representation of multifunctional MNPs, consisting essentially of:

1) a nanometric inorganic magnetic core;
2) an organic biocompatible coating;
3) a biologically active entity (a protein, an antibody, a small molecule)

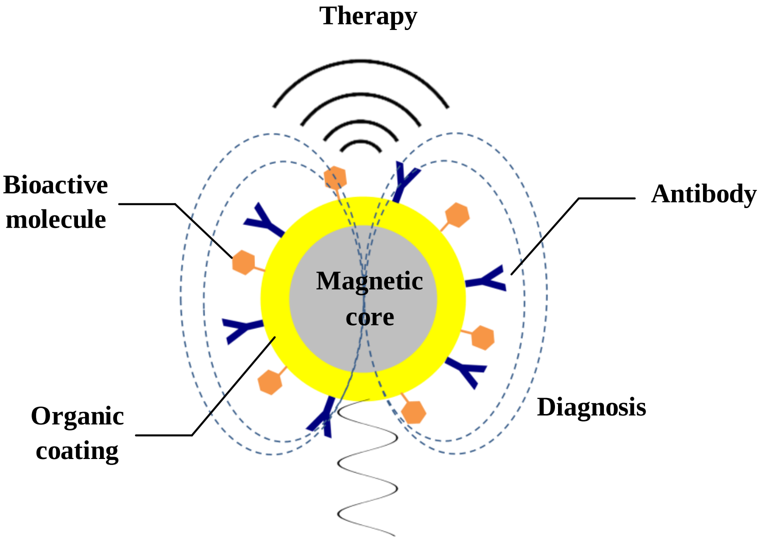

Figure 1.2 : Theranostic multifunctional MNPs can act simultaneously as diagnostic tools and as therapeutic agents.

Considering this particular aspect we can appreciate the importance that a specific functionalization of MNPs could have in the development of an efficient tool for theranostic applications. For this purpose it is fundamental to develop a specific coating capable to make MNPs biocompatible and highly stable in physiological conditions so as to prolong their circulation time and the possibility to reach the target-cells [1a].

Another fundamental feature offered by MNPs is that they can represent a suitable scaffold for the multivalent exposition of biomolecules, which is essential for their interaction with biological entities, as indeed required in biomedicine. Multivalent interactions are characterized by the simultaneous binding of multiple ligands on a biological entity (a molecule or a surface), to multiple receptors on another. These interactions are very common in biology and have a number of characteristics that monovalent interactions do not possess [20]. Multivalent interactions are usually based on not covalent bonds, such as hydrogen bonds, metal-ligand coordination, hydrophobic interactions and ionic bonds, which are all characterized by low energy and low specificity. However, increasing the number of the interactions, they become efficient and specific. Multivalent interactions can be collectively much stronger than the corresponding monovalent interactions thus providing many advantages.

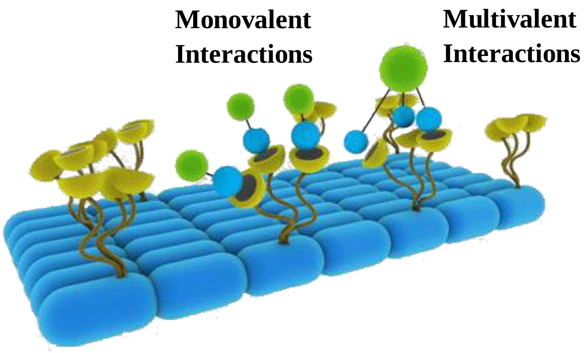

Figure 1.3 : Ligand - Receptors interactions : monovalent interactions compared to multivalent interactions.

In a multivalent system the intensity of the signal can be simply varied by changing the number of ligand-receptors couples involved in the interaction. The signal modulation has a crucial role in biology, because the communications between biological entities do not rely on a *on-off* mechanism, and the biological answer to any environment alteration must be finely tuned. Moreover, multivalent interactions can induce morphological macroscopic modifications in cells during communication, thus improving the efficiency of the process.

A perfect example of this signal modulation is represented by the role that macrophages play in the immune response towards pathogenic organism. Indeed, macrophages, are able to engulf and then digest a bacterium only after the interaction with two or more antibodies takes place, (Figure 1.4) avoiding an immune response in the case of a single antibody bonding.

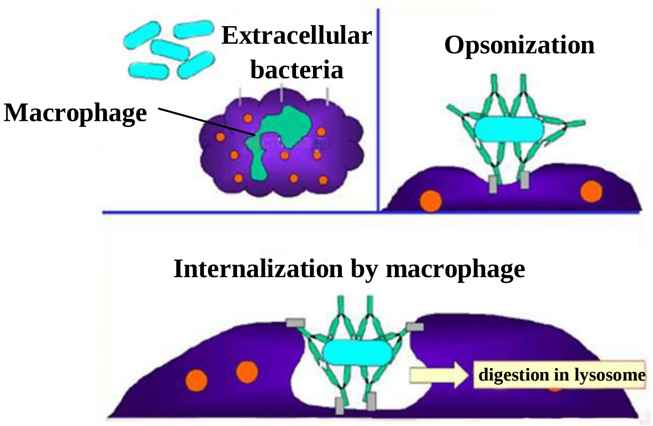

Figure 1.4 : Macrophages engulf pathogen organism after an antibodies multivalent interaction. The opsonization process *marks* the bacterium with specific opsonins enhancing phagocytosis. After the internalization, the bacteria will be digested in lysosomes (see Chapter 5).

Besides the adhesion of a bacteria to the surface of a cell, multivalent interactions are involved in many other biological processes, as for example, the adhesion of viruses to host cells, the interaction with toxins or antibodies, or the cell-cell communication (Figure 1.5). Some notable practical examples are provided by the interaction of influenza virus with bronchial epithelia cells [21] or the lectine-carbohydrate recognition which is the basis of most of the cell-cell recognition processes [22].

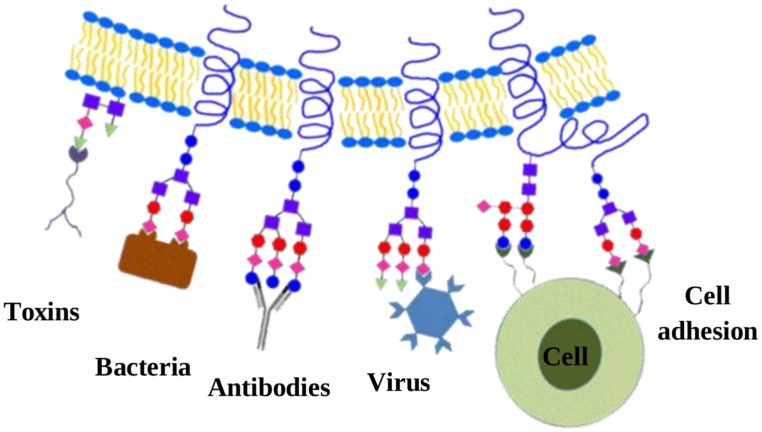

Figure 1.5 : Examples of multivalent interactions in biological systems between a cell and toxins, bacteria, antibodies, viruses or other cells.

From the scenario described above it clearly emerges that MNPs decorated in a multivalent manner with biologically active molecules may hold great importance in selective targeting and in the development of novel theranostic tools for specific pathologies. In fact the magnetic core of MNPs represents a very promising multivalent scaffold. Indeed, if on one hand the multivalent presentation of specific epitopes to the immune cells can pave the way towards the application in immunotherapy and in particular in the development of antigen-specific vaccines [23], on the other the combination with the unique sensing, moving and heating properties provided by MNPs, can significantly enlarge the number of diagnostic and therapeutic functionalities conjugated in the same nanosystem.

As a matter of fact, immunotherapy has emerged as a powerful strategy in the fight against tumours and, the development of therapeutic vaccines using synthetic antigens, as immunogens, is becoming the ultimate goal in this field. Indeed, tumours uniquely or excessively express antigens (Tumour-Associated Antigens, TAAs) and, in particular, glycan antigens (Tumour-Associated Carbohydrate Antigens, TACAs), which can be useful targets for vaccines. TACAs are indeed widely exposed on cancer cell surfaces and their expression often correlates with cancer developmental stages, including invasion and metastasis. Furthermore, an abnormal glycosylation in the primary tumours is considered a signal of poor prognosis [24]. Despite the large numbers of TAAs/TACAs so far described, their use in tumour therapy remains limited and needs some improvements. This is not only because immune responses in cancer patients can be relatively weak, but also because TACAs are poorly immunogenic antigens. Moreover, most TACAs are recognized as self and, according to their saccharidic nature, they cannot be presented to T cells for T cell responses (T cell independent type II antigens). Consequently, the class switch from IgM to IgG and the recall memory response are not generated [25]. IgM (immunoglobulin M) is a type of antibody produced by B cells, and it is the first antibody elicited in response to initial exposure to an antigen; IgG (immunoglobulin G) are also produced by B cells but represent the long term response of the body to a disease. IgM are short term, disappear after a few weeks and they are then replaced by IgG that provide a long lasting immunity [26]. A successful strategy to overcome the limitations mentioned above, might be mimicking the natural multivalent approach of the molecular biosystems by binding carbohydrate antigens to multivalent scaffolds, such as nanomaterials. TACA multivalent display, indeed, mimicking the natural multivalent carbohydrate presentation on a cell surface, can lead to B cell activation and antibody production [27]. Furthermore, a nanomaterial, as antigen delivery system, can provide an adjuvant activity, inducing the activation and maturation of antigen presenting cells (APCs), [28] thus promoting the antigen cross-presentation [29]. All these events are essential for the induction of an efficient antitumour immune response.

In this context, the main target of this thesis has been the synthesis and characterization of a novel glycoconjugate nanosystem composed by magnetite MNPs functionalized with a synthetic, conformationally rigid mimetic of the α-Tn antigen [30], that is a TACA expressed in carcinoma-associated mucins [31], for application in immunotherapy. The evaluation of the immunoactivity of the glycosylated MNPs was accomplished by means of *in vitro* tests on the activation of macrophages. The choice of macrophages is based on the fact that they represent a perfect "bridge" between the innate immunity and the adaptive immunity and play a crucial role in the activation and amplification of the immune response [26].

In addition, since this work was aimed at the development of a multifunctional magnetic nanosystem, important efforts were devoted to the development of a suitable synthetic procedure for obtaining MNPs with optimized physical and chemical properties for their application in nanomedicine.

For the synthesis of MNPs we exploited the thermal decomposition of metal-organic precursors in high boiling solvent [32]. Several attempts were performed in order to obtain highly crystalline, pure magnetite MNPs with a size in the 12-15 nm range varying the experimental parameters like the nature of the metal-organic precursor, the amount and kind of surfactants, the solvent, or the heating ramp. This particular size corresponds to the best compromise between a large heating efficiency in magnetic fluid hyperthermia and colloidal stability.

Finally, in order to make the proposed approach more versatile, we explored diverse functionalization methods, by changing the bifunctional linker used to link the saccharidic epitope onto the surface of the MNPs. We thus obtained nanosystems with suitable water solubility and suitable to be further coupled with bioactive molecules. In particular, we synthesized a new bifunctional linker derived from hexaethylene glycol to confer to MNPs the desired solubility and reactivity towards further functionalization.

For a better comprehension of this PhD work a brief summary is reported here after:

- in Chapter 2, the experiments performed for MNPs synthesis, changing the precursor for the thermal decomposition and the reaction conditions, in order to optimize their structural and physical properties, are described;
- Chapter 3 is dedicated to the α-Tn antigen mimetic, from its synthesis to the bonding to the magnetite MNPs;
- in Chapter 4 it is described the preparation of functionalized MNPs samples used as negative controls for the biological tests on the macrophages activation, in order to better evaluate the effect of **MNP**s decorated with the α-Tn antigen mimetic on immune cells;
- in Chapter 5 the above mentioned biological tests on macrophages activation are described in detail;
- Chapter 6 is focused on the study of bifunctional ligands for MNPs functionalization in order to render them suitable for further decoration with bioactive molecules. We describe the functionalization of MNPs with an aminosilane ligand and then the synthesis of a new bifunctional ligand derived from hexaethylene glycol bearing two diverse functional groups: a phosphonate group at one end and an amino group at the other;
- conclusions and future perspective are exposed in Chapter 7;
- in Chapter 8 all the experimental data and the descriptions of the characterization techniques are reported.

References

[1] (a) A. G. Roca, R. Costo *et al., J. Phys. D:Appl. Phys.*, **2009**, *42*, 224002; (b) P. Tartaj, M.P. Morales et al., *J. Phys. D: Appl. Phys.*, **2003**, *36* R182.

[2] (a) Q. A. Pankhurst, N. K.T. Thanh *et al., J. Phys. D: Appl. Phys.*, **2009** *42*, 224001; (b) Q.A. Pankhurst, J. Connolly *et al., J. Phys. D: Appl.Phys.*, **2003**, *36*, R167; (c) for magnetic biosensors: J.B. Haun,T.J. Yoon *et al., Nanomed. Nanobiotechnol.*, **2010**, *2*, 291; (d) C.T.Yavuz, J.T. Mayo *et al.*, *Science*, **2006**, *314*, 964.

[3] (a) D. Jiles, *Introduction to Magnetism and MagneticMaterials* (London: Chapman and Hall), **1991**; (b) A. H. Morrish, *The Physical Principles of Magnetism*,(New York: IEEE Press), **2001**; (c) J. M. D. Coey, *Magnetism and Magnetic Materials*, Cambridge Univ. Pr. (**2010**).

[4] E. C. Stoner, E. P. Wohlfarth; *Philosophical Transaction of the Royal Society A*, **1948**, *240*, 599.

[5] J. Sun *et al, J. Biomed. Mater. Res.* A, **2007,** *80A*, 333; (b) A. K. Gupta and S. Wells, *IEEE Trans. Nanobiosci*, **2004**, *3*, 66; (c) B. Ankamwar; T. C. Lai; J. H. Huang; R. S. Liu; M. Hsiao; C. H. Chen and Y. K. Hwu, *Nanotechnology*, **2010**, *21* 075102 (9pp).

[6] D. Högemann; L. Josephson; R. Weissleder and J. P. Basilion, *Bioconjugate Chem.* **2000,** *11*, 941; (b) L. Levy, Y. Sahoo; K. S. Kim; E. J. Bergey and P. N. Prasad, *Chem. Mater.*, 2002, *14*, 3715; (c) Y. Zhang, N. Kohler and M. Zhang, *Biomaterials*, **2002,** *23*, 1553.

[7] (a) P. C. Lauterbur, *Nature*, **1973**, *242*, 190; (b) P. Mansfield; P. G. Morris, *NMR imaging in biomedicine*, Suppl.2 Adv. Mag. Res., Academic Press, **1982**; (c) C. Guy; D. Ffytche, *An introduction to the principles of medical imaging*, Imperial College Press eds.London, **2000**.

[8] (a) S. Laurent; L.Van der Elst *et al.*, *Helv.Chim.Acta*, **2000**, *83*, 394; (b) S. Laurent; D. Forge *et al.*, *Chem. Rev.*, **2008**, *108*, 2064; (c) E. Taboada; R. Solanas *et al.*, *Adv. Funct. Mater.*, **2009**, *19*, 2319.

[9] (a) G. F. Goya; V. Grazú; M. R. and Ibarra, *Current Nanoscience*, **2008,** *4,* 1 **(**b) D. Pouliquen, H. Perroud et al., *Mag.Res.Med*., **24**, p. 75 (1992); b) W. Reith, M. Forsting et al., *Am. J. Neuroradiol*., **16**, p. 53 (1995).

[10] (a) W. S. Enochs; F. Harsh; F. Hochberg and R. Weissledher, *J. Magn. Reson. Imaging*, **1999**, *9*, 228; (b) P. Varallyay; G. Nesbit; L. L. Muldoon; R. R. Nixon; J. I. Delashaw; J. I. Cohen; A. Petrillo; D. Rink and E. A. Neuwelt, *AJNR Am. J. Neuroradiol.*, **2002**, *23***,** 10.

[11] S. E. Barry, *Int. J. Hyperthermia.*, **2008**, *24***,** 451.

[12] C. Sun; J. S. H. Lee and M. Zhang, *Adv. Drug Del. Rev.*, **2008**, *60***,** 1252.

[13] R. A. Gardner; H. I. Vargas; J. B. Block; C. L. Vogel; A. J. Fenn; G. V. Kuehl; M. Doval, *Ann. Surg. Oncol.*, **2002**, *9*, 326.

[14] (a) H. H. Kampinga, *Int. J. Hyperthermia*, **2006**, *22*, 191; (b) C. F. Gottlieb; G. B. Seibert; N. L. Block, *Radiology*, **1988**, *169*, 243.

[15] (a) D. L. Cockroft,; D. A. T. New, *Nature*, **1975**, *258*, 604; (b) X. He; S. McGee; J. E. Coad; F. Schmidlin; P. A. Iaizzo; D. J. Swanlund; S. Kluge; E. Rudie; J. C. Bischof, *Int. J. Hyperthermia*, **2004**, *20*, 567.

[16] K. F. Chu and D. E. Dupuy, *Nature Reviews Cancer*, **2014**, *14*, 199.

[17] (a) L. F. de Freitas; L. C. Zanelatto; L. M. S. Mantovani; P. B. G. Silva; R. Ceccini; C. Grecco; L. T. Moriyama; C. Kurachi; V. C. A. Martins and A. M. G. Plepis, *Laser Phys.*, **2013**, *23*, 066003; (b) X. Huang; I. H. El-Sayed; W. Qian; M. A. El-Sayed, *J. Amer. Chem. Soc.*, **2006**, *128*, 2115.

[18] (a) H. Maeda; *Advances in Enzyme Regulation*, **2001**, *41*, 189; (b) O. Clement; N. Siauve; M. Lewin; E. de Kerviler; C.A. Cuenod; G. Frija, *Biomedicine and Pharmacotherapy*, **1998**, 52, 51.

[19] K. Maier-Hauff; F. Ulrich; D. Nestler; H. Niehoff; P. Wust; B. Thiesen; H. Orawa; V. Budach and A. Jordan, *J. Neurooncol.*, **2011**, *103*, 2, 317.

[20] M. Mammen; S.-K. Choi; G. M. Whitesides, *Angew. Chem., Int. Ed.*, **1998**, *37*, 2754.

[21] a) W. J. Lees; A. Spaltenstein; W. J. E. Kingery; G. M. Whitesides, *J. Med. Chem.*, **1994**, *37*, 3419.

[22] H. Lis; N. Sharon, *Chem. Rev.*, **1998**, *98*, 637.

[23] (a) B. L. Wilkinson; S. Day; L. R. Malins; V. Apostolopoulos; R. J. Payne, *Angew. Chem. Int. Ed.*, **2011**, *50*, 1635; (b) S. Grigalevicius; S. Chierici; O. Renaudet; R. Lo-Man; E. De´riaud; C. Leclerc; P. Dumy, *Bioconjugate Chemistry*, **2005**, *16*, 1149; (c) Q. Li; M. R. Anver; D. O. Butcher; J. C. Gildersleeve; *Mol.Cancer Ther.*, **2009**, *8*, 971; (d) G. F. Springer; P. R. Desai; H. Tegtmeyer; B. D. Spencer; E. F.Scanlon, *Ann. N. Y. Acad. Sci*. **1993**, *690*, 355; (d) G. F. Springer; P. R. Desai; W. Wise; S. C. Carlstedt; H.Tegtmeyer; H. Stein, E. F. Scanlon in *Immunodiagnosis of Cancer*, 2nd ed. (Eds.: R. B. Herberman, D.W. Mercer), MarcelDekker, New York, **1990**, 587.

[24] Z. Guo and Q. Wang, *Curr. Opin.Chem. Biol.*, **2009**, *13*, 608.

[25] C. C. Liu and X. S. Ye, *Glycoconjugate J.*, **2012**, *29*, 259.

[26] A. K. Abbas; A. H. Lichtman, *Basic Immunology: : Functions and Disorders of the Immune System*, Saunders; 3 edition (February 12, **2010**).

[27] A. L. Parry; N. A. Clemson; J. Ellis; S. S. Bernhard; B. G. Davis and N. R. Cameron; *J. Am. Chem. Soc.*, **2013**, *135*, 9362.

[28] S. T. Reddy; M. A. Swartz and J. A. Hubbell, *Trends Immunol.*, **2006**, *27*, 573.

[29] S. Hirosue; I. C. Kourtis; A. J. van der Vlies; J. A. Hubbell and M. A. Swartz; *Vaccine*, **2010**, *28*, 7897.

[30] T. Ju; V. I. Otto; R. D. Cummings, *Angew. Chem. Int. Ed.*, **2011**, *50*, 1770.

[31] M. A.Hollingsworth; B. J. Swanson, *Nature Reviews Cancer*, **2004**, *4*, 45.

[32] S. Sun; H. Zeng; *J. Am. Chem. Soc.*, **2002**, *124* (28), 8204.

2. Synthesis of MNPs

Nowadays, there is a great interest in the use of MNPs in various field of application, from engineering to nanobiotecnology and biomedicine [1]. The critical dependence of their physical properties on the particle size, shape and structure if on one hand allows for a fine tuning of their behaviour, on the other requires a tight control at the synthetic level. As a consequence, a wealth of methods of synthesis has been developed to answer to the different need arising from the different applications meanwhile granting a fine control on the morphological properties. In the literature many procedures are described concerning the *bottom-up* approach and most of them are focused on the thermal decomposition of a precursor (metal-organic or inorganic salts) in the presence of surfactants in high boiling solvents [2]. It is worth to note that the thermal decomposition method is one of the best in terms of crystallinity, size distribution and magnetic properties of the final product, particularly if compared with the co-precipitation method, the sol-gel processes or the synthesis in reverse micelles. Thanks to these advantages thermal decomposition has rapidly gained a large popularity, becoming one of the most common method for the production of MNPs [3]. However, despite of its large popularity, this technique is still suffering some drawbacks in terms of reproducibility, phase homogeneity and size or composition control. The main hurdle found by each "nanoparticle-chemist" is to reproduce in his own laboratory the procedure illustrated in a paper getting the same results. This is mainly due to the great number of experimental variables that must be simultaneously controlled in the reaction set-up, like the temperature increasing rate, the stirring rate, the nitrogen flow and many others. Each one of them affects the nature and the quality of the final product, thus it is essential to set all the parameters in order to obtain the desired product [4].

In this work the thermal decomposition process has been chosen as the principal way to obtain good quality magnetite MNPs exploitable for our purpose. In the following paragraph the attempts to synthesize iron oxide MNPs with a diameter of about 12-15 nm varying the nature of the precursor and the experimental conditions will be described. For each precursor many experiments were performed in order to analyze the dependence of the MNPs behaviours on the experimental parameters and thus find the best reaction conditions.

2.1 Synthesis with FeOOH

The first precursor tested for the thermal decomposition reaction was the iron (III) oxide hydrate, FeOOH in the presence of oleic acid as surfactant and 1-

octadecene as high boiling solvent (b.p. 320°C). The MNPs were prepared following a procedure similar to that reported by Xue *et al* [5].

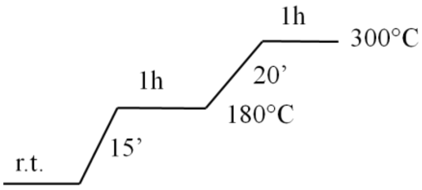

Precursor	Surfactant	Solvent
FeOOH	Oleic Acid	1-Octadecene

Figure 2.1: Heating rate ramp for the thermal decomposition reaction of FeOOH.

Sample	$\frac{\text{precursor}}{\text{surfactant}}$	Precursor conc. (mg/mL)	Reaction atmosphere
IOMNP1	1/4	28.5	Inert (N_2)
IOMNP2	1/5.5	7.2	Inert (N_2)
IOMNP3	1/5.5	7.2	Air
IOMNP4	1/5.5	7.2	bubbling air

Table 2.1: Experimental conditions used for to thermal decomposition of FeOOH

Different samples were prepared by varying the reaction conditions (Table 2.1). However the increasing temperature rate and the length of the final step at 300°C were always kept constant in all syntheses and equal to 10°C/min up to 180°C and 6°C/min up to 300°C (Figure 2.1). All samples were recovered from the reaction mixture by magnetic decantation followed by several washing/precipitating steps. Details of the preparation are given in the experimental section.

The reaction was first carried out at a 1:4 precursor/surfactant concentration ratio under inert atmosphere. The as prepared MNPs **IOMNP1** have an XRD pattern compatible with a mixed phase composed by a 53% of the cubic inverse spinel structure of magnetite (PDF 89-0691) maghemite (PDF 39-1346) or any partially oxidized intermediate ferrite phase, which cannot be discriminated from each other by this technique and by a 47% of the rhombohedral structure of hematite (PDF 24-0072) (Figure 2.2). The quantification of each phase was obtained analyzing the diffraction pattern by the Rietveld method. The same procedure was followed for all the phase quantification data reported in this chapter.

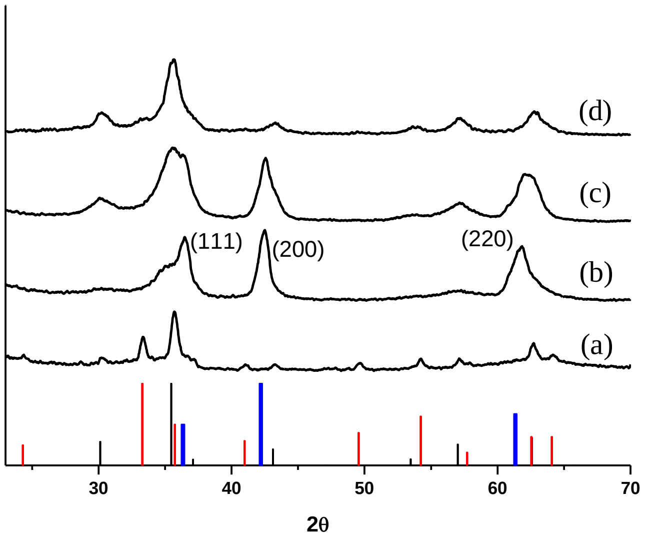

Figure 2.2: XRD patterns of samples a) IOMNP1, b) IOMNP2, c) IOMNP3, d) IOMNP4. The black bars correspond to the reference magnetite pattern (PDF 89-0691), the red bars correspond to the reference hematite pattern (PDF 24-0072), the blue bars correspond to the reference wüstite pattern (PDF 01-1223).

The presence of the hematite phase is undesired since it negatively affects the magnetic properties of the final product; indeed, hematite is characterized by a transition temperature, known as Morin transition, at T_M=263-267 K; below T_M hematite is purely antiferromagnetic and above T_M is weakly ferromagnetic [6]. Since for biomedical application we need MNPs with a high magnetic moment, the presence of the hematite phase represents a great drawback.

In order to obtain the magnetite phase only, the reaction was repeated by performing three experiments in a four-fold diluted reaction mixture at a 1:5.5 precursor/surfactant ratio and varying the atmosphere reaction.

Sample **IOMNP2** was obtained by accomplishing the reaction under inert N_2 atmosphere. In this case no evidence of the hematite secondary phase was observed in the XRD pattern. However, the pattern reveals the presence of a large amount of another parasitic phase: in fact the Rietveld analysis reveals the nanopowder is composed by a 63% of magnetite and 37% of wüstite, as it clearly appears from the appearance of three peaks, which can be attributed to the (111),

(200) and (220) families of planes of the cubic face centered structure of wüstite over the characteristic pattern of magnetite. The disappearance of the hematite (Fe_2O_3) phase replaced by wüstite (FeO) can be imputed to the higher amount of reducing agents, like CO and H_2 produced during the thermal decomposition of the organic ligand due to the lower precursor/surfactant ratio [7]. Since bulk wüstite is paramagnetic at room temperature and presents an antiferromagnetic ordering below 200 K, similarly to hematite it reduces the magnetic moment of the MNPs.

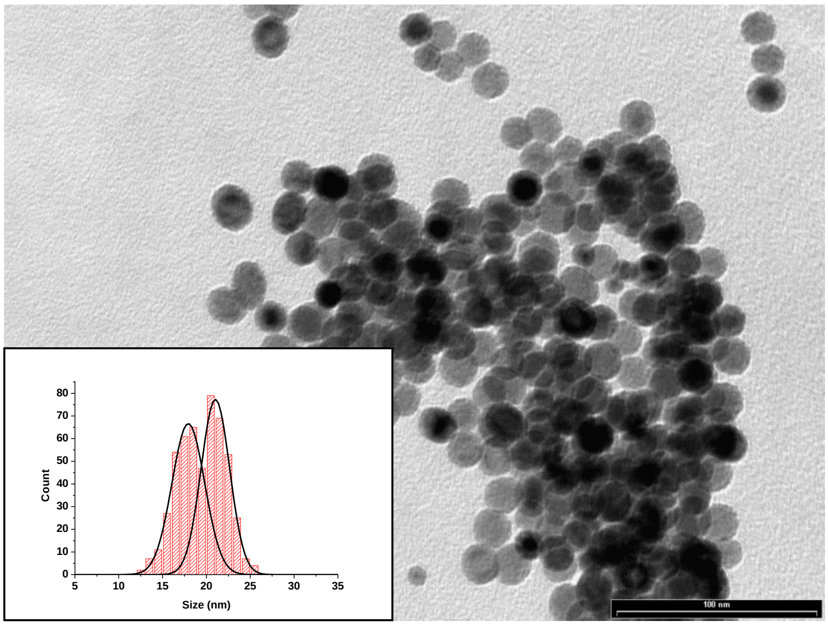

Figure 2.3 : TEM image of sample IOMNP2. In the inset the size distribution evaluated over 550 MNPs is reported. The two distributions are centered at 17.9 ± 3.8 nm and 21.0 ± 3.3 nm.

Sample **IOMNP2** showed the presence of a double population with two distributions centered at 17.9 ± 3.8 nm and 21.0 ± 3.3 nm, respectively, as highlighted in the inset of Figure 2.3. Despite the sample displayed a good homogeneity in terms of shape (almost all the MNPs are spherical), the presence of a double population and the large size are not appropriate to our purposes.

In order to promote the oxidation of Fe(II) to Fe(III) the reaction was first repeated under air atmosphere (sample **IOMNP3**) and then with air bubbled directly into the reaction mixture (sample **IOMNP4**).

The XRD pattern of sample **IOMNP3** still shows the presence of the mixed phase magnetite/wüstite but the percentage of magnetite phase increased to 78% (the rest 22% being wüstite). The efficacy of a more oxidant atmosphere was demonstrated by the XRD pattern of sample **IOMNP4** that displays the complete disappearance of wüstite phase, albeit it is possible to find a 17% of hematite detectable from the peak assigned to (104) family of planes while the percentage of the magnetite phase was found equal to 83%.

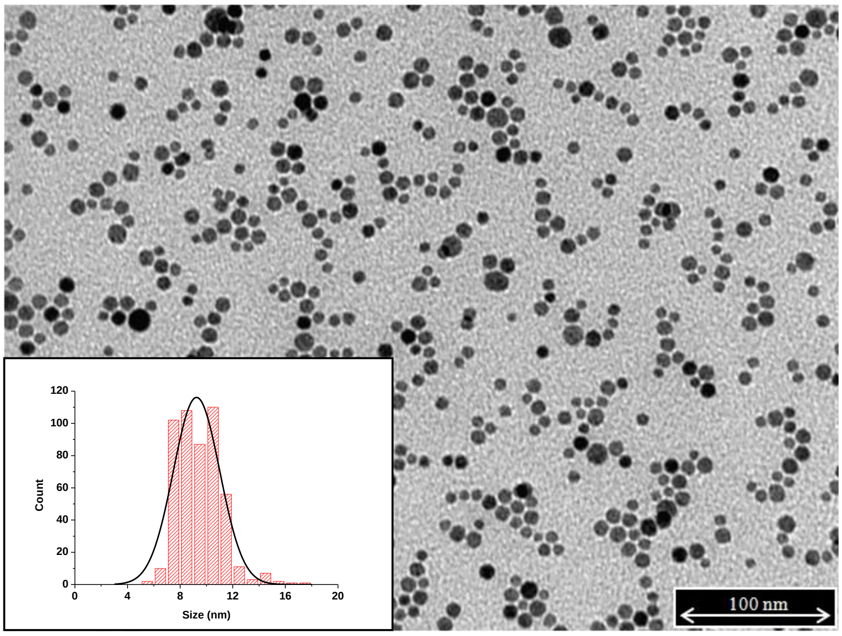

Figure 2.4 : Representative TEM image of sample IOMNP3 (d= 9.5 ± 1.7 nm). In the inset the size distribution evaluated over 500 MNPs is reported.

Interestingly, sample **IOMNP3** retained an almost spherical shape such as sample **IOMNP2**, but the mean size decreased to 9.5 ± 1.7 nm despite the reaction atmosphere was the only experimental parameter changed (Figure 2.4). This result confirmed the strong dependence of the product's properties on the adopted experimental conditions.

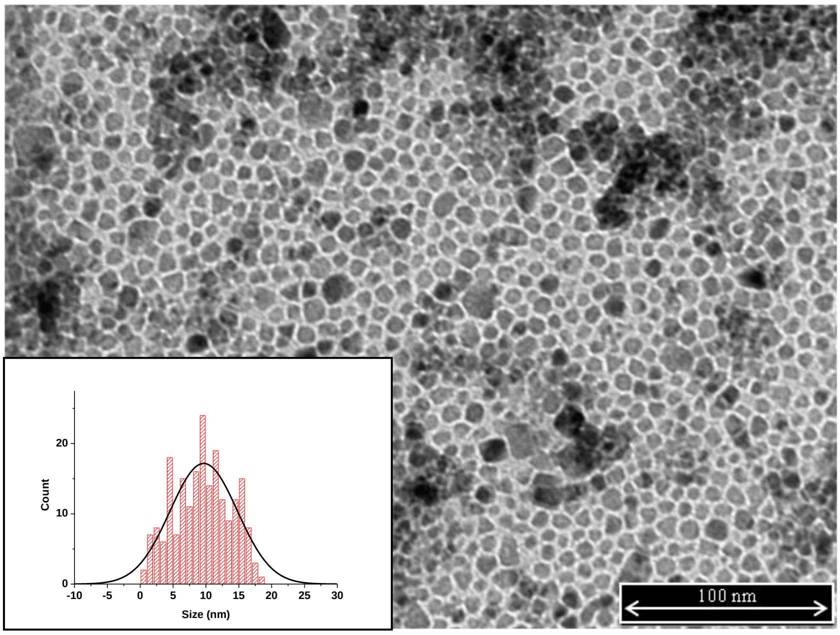

Figure 2.5 : TEM image of sample IOMNP4 (d= 9.4 ± 4.3 nm). In the inset the size distribution evaluated over 300 MNPs is reported.

In Figure 2.5 a representative TEM image of sample **IOMNP4** is shown. In this case the shape is very irregular and many large aggregates were formed. The inset in Figure 2.5 is a proof of the great polydispersity achieved in this sample (the mean size measured was found equal to 9.4 ± 4.3 nm). In conclusion, although the "bubbling-air" method has proven useful to avoid the formation of wüstite, it still presents some problems: indeed, the flow of air into the reaction mixture interfered with the correct increasing temperature rate causing a lowering of the temperature up to 250°C, which in turns produced a bad control on MNPs growth. Also the stirring rate is negatively affected, worsening the control on the final size and size distribution of the MNPs. Moreover, neither the use of bubbling air during the reaction led to the formation of a unique crystal phase.

2.2 Synthesis with iron(III) oleate

Since the results obtained using FeOOH were not satisfactory, an attempt was performed by replacing the substrate for the thermal decomposition reaction with iron(III) oleate ($Fe(ole)_3$). The use of this precursor is a versatile method which allows tuning the mean size of MNPs by simply varying the experimental parameters like the heating rate ramp, the $Fe(ole)_3$/oleic acid ratio and the reagents concentration. It is worth to note that $Fe(ole)_3$ is not commercially available and thus need to be synthesized [8]. In our case we used a well established procedure based on the reaction of $FeCl_3 \cdot 6H_2O$ with sodium oleate (NaOle) according to the scheme below:

$$FeCl_3 \cdot 6H_2O \quad + \quad NaOle \xrightarrow[\text{70°C, 4h}]{H_2O \text{ / Ethanol / Hexane}} Fe(Ole)_3$$

Scheme 2.1 : Scheme for the synthesis of iron (III) oleate.

$Fe(ole)_3$ was used in the thermal decomposition reaction in the presence of oleic acid as surfactant in a 1:3 precursor/surfactant ratio, using 1-octadecene as solvent.

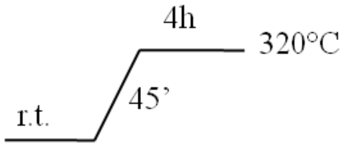

Figure 2.6: Heating rate ramp for the thermal decomposition reaction of $Fe(ole)_3$.

The reaction was performed under inert atmosphere (N_2) and after 4h of reflux the MNPs were recovered by magnetic decantation and purified by several washing/precipitating steps (sample **OlMNP1**).

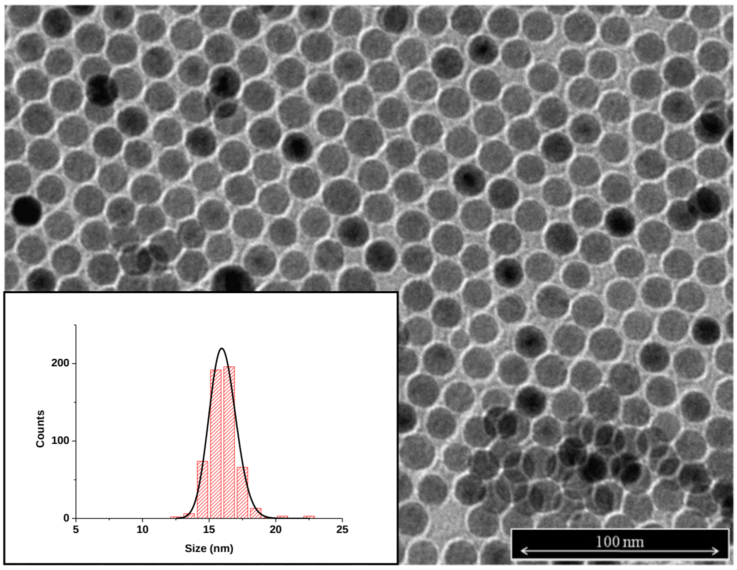

Figure 2.7 : TEM image of OlMNP1 (d = 16.1± 1.1 nm) . In the inset the size distribution evaluated over 550 MNPs is reported.

TEM images (a typical example is shown in Figure 2.7) demonstrate that the synthesized MNPs have a spherical shape and a mean diameter of 16.1±1.1 nm with a extremely narrow size distribution.

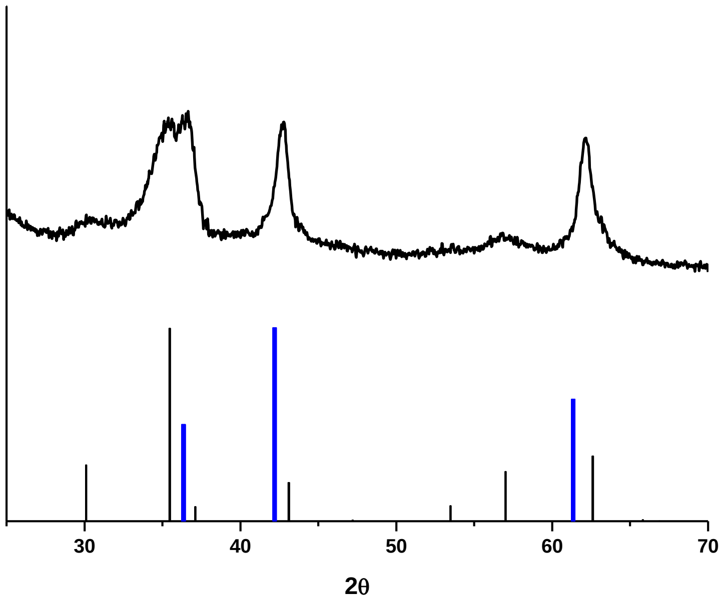

Figure 2.8 : XRD pattern of OlMNP1. The the black bars correspond to the reference magnetite pattern (PDF 89-0691), the blue bars correspond to the reference wüstite pattern (PDF 01-1223).

However, the XRD pattern of sample **OlMNP1**, reported in Figure 2.8 shows, also in this case the presence of two phases, which after the Rietveld analysis can be attributed to magnetite (74%) and wüstite (26%). As previously stated, wüstite affects negatively the magnetic properties of the MNPs since, due to his antiferromagnetic character, it lowers the total magnetic moment of the MNPs. In order to eliminate this parasitic product, an attempt of oxidizing wüstite by a heating treatment of the MNPs in an oven under air atmosphere at different temperatures, (T = 65°C, 90°C, 140°C), and different time (t = 24 h, 48 h at T = 65 °C) was performed. The obtained results are resumed in Table 2.2, where the phase content evaluated from the analysis of the XRD patterns is reported.

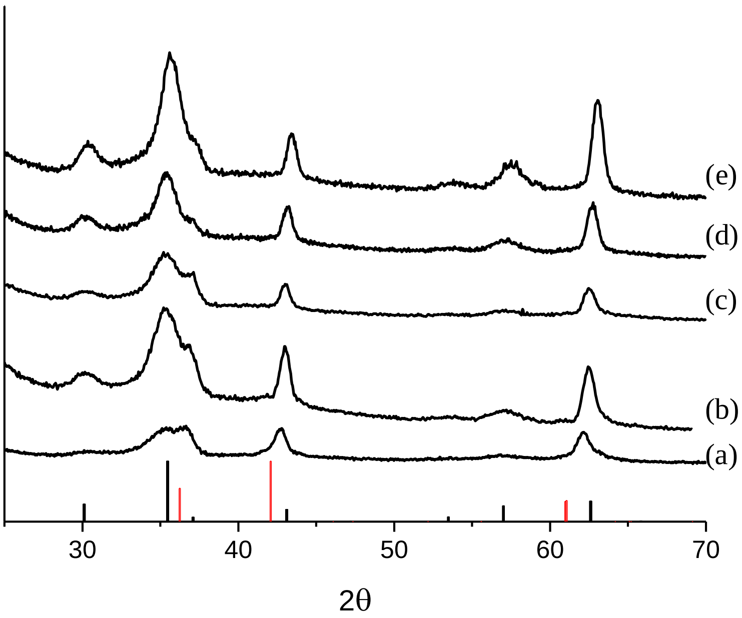

Figure 2.9 : XRD pattern of sample OlMNP1 before and after the heating treatment. a) as prepared MNPs; b) after heating treatment at 65°C for 24h; c) after heating treatment at 65°C for 48h; d) after heating treatment at 90°C for 24h; e) after heating treatment at 140°C for 24h. The black bars correspond to the reference magnetite pattern (PDF 89-0691), the red bars correspond to the reference wüstite pattern (PDF 01-1223)

Comparing the XRD patterns of sample **OlMNP1** before and after the heating treatments it is possible to observe a gradual increase of the magnetite phase on increasing temperature up to 90°C (Figure 2.9). Indeed, heating the sample at that temperature, the wustite content decreases to 7%. Then, a further increase in temperature does not produce any significant variation in the relative amounts of the two magnetic phases. On the other hand, also increasing the heating time does not allow to completely eliminate wüstite (Table 2.2).

Heating treatment	Magnetite content	Wüstite content
65°C - 24h	85%	15%
65°C - 48 h	90%	10%
90°C - 24h	93%	7%
140°C - 24h	92%	8%

Table 2.2 : Magnetite and wüstite contents in sample OlMNP1 after the heating treatment..

Moreover, the average diameter of the sample oxidized at 90°C, evaluated by using the Scherrer's formula, was 8.3(2.4) nm pointing out that the temperature at which oxidation take place is not large enough to convert the iron oxide into crystalline ferrite [9]. It is worth to note that the peak broadening of the XRD pattern negatively affected the quality of the fit used for determination of crystallites size as well as indicated the low crystallinity of this sample.

The magnetic properties of **OlMNP1** treated at 90°C, **OlMNP1@90**, for 24h were investigated recording the hysteresis loop at 2.5 K and 300 K in the ± 5 T range (Figure 2.10) An open hysteresis loop was measured at 2.5 K with a coercive field μ_0H of 52 mT and a reduced remnant magnetization M_{0T}/M_{5T}, of 0.30. No magnetic irreversibility was observed at 300 K, indicating that the blocking temperature, i.e. the temperature at which the nanosystem switches from a blocked to a superparamagnetic state is smaller than room temperature. The magnetization was almost saturated at the highest measuring field of 5T reaching a value of 53 Am^2Kg^{-1} at 2.5 K and then it slightly decreases at room temperature down to 50.5 Am^2Kg^{-1}.

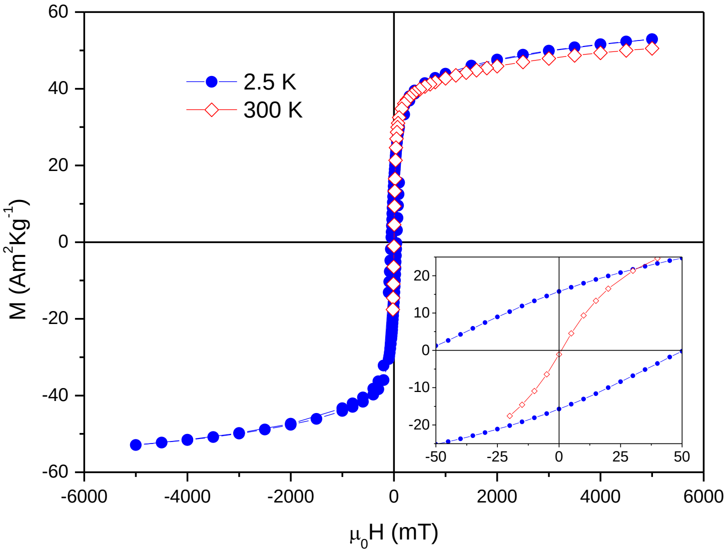

Figure 2.10 : Hysteresis loop recorded at 2.5K (blue dotted line) and at 300 K (red dotted line) and corresponding enlargement of the low field region for sample OlMNP1@90.

The saturation magnetization is lower than the bulk value of 90 Am^{2}Kg^{-1} [10]. This effect can be attributed both to the presence of the antiferromagnetic wüstite phase and to the occurrence of surface structure defects that can lead to magnetic disorder and hence to a global decrease of the magnetization.

In order to obtain MNPs with a higher magnetic moment the oxidation procedure was then modified replacing the heating treatment in oven with one in solution. To this aim sample **OlMNP1** was dissolved in 1-octadecene in the presence of oleic acid so as to obtain a stable suspension. A flux of air was then bubbled into the reaction mixture which was heated up to T = 290°C at a rate of 17°C/min. At the end of the oxidation treatment the MNPs were magnetically decanted and washed several times in order to remove the excess of surfactant.

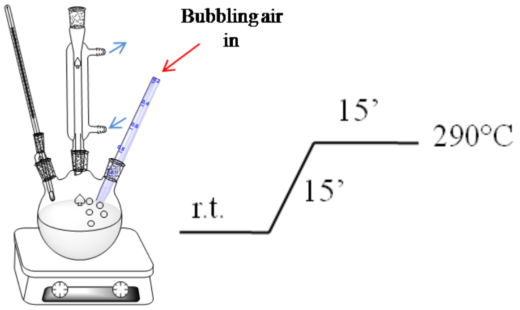

Substrate	Mixed phase MNPs
Surfactant	Oleic acid
Solvent	1-octadecene

Figure 2.11 : Experimental conditions adopted for the oxidation of the mixed phase MNPs.

The XRD pattern of the as obtained MNPs confirmed the efficacy of the oxidation process showing the complete disappearance of the wüstite phase (Figure 2.12).

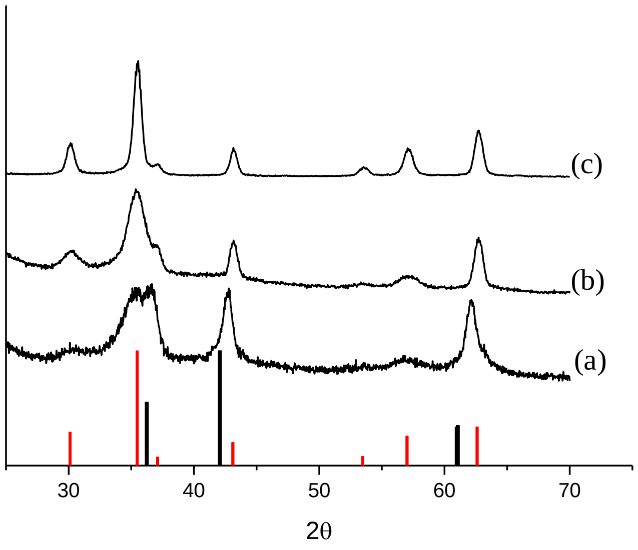

Figure 2.12 : Comparison between XRD patterns of (a) mixed phase MNPs synthesized from Fe(ole)$_3$, (b) OlMNP1@90, oxidized in oven at 90°C for 24h, (c) OlMNP1@290, oxidized in 1-octadecene solution at 290°C with bubbling air.

Moreover, the peak broadening is significantly reduced in this last sample, (the average size of the coherent scattering dominion was estimated to be 12.5(0.3) indicating the crystal quality was significantly improved by the heating treatment carried out in solution.

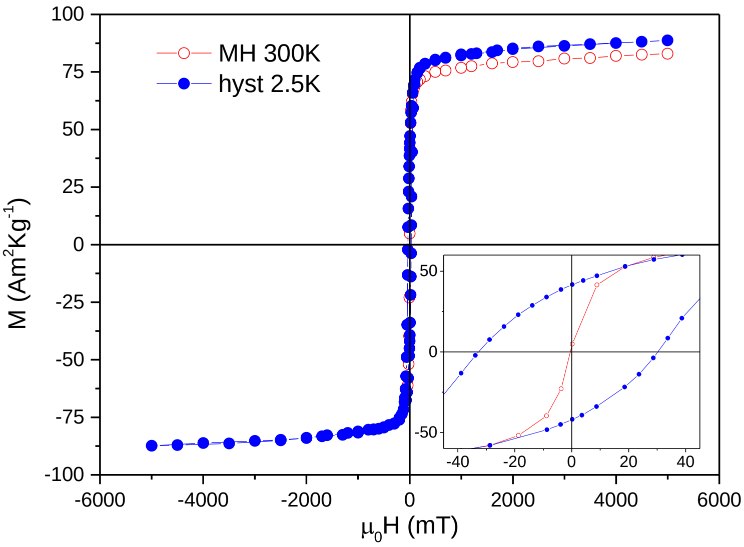

Figure 2.13 : Hysteresis loop of OlMNP1@290, oxidized in 1-octadecene solution at 290°C with bubbling air, recorded at 2.5K (blue dotted line) and at 300 K (red dotted line) and corresponding enlargement of the low field region.

The hysteresis loop at 2.5 and 300 K of **OlMNP1@290** are shown in Figure 2.13. An open hysteresis loop was measured at 2.5 K with a coercive field $\mu_0 H$ of 31 mT and a reduced remnant magnetization M_{0T}/M_{5T}, of 0.47, while no magnetic irreversibility was observed at 300 K. Unlike **OlMNP1@90**, the magnetization is almost saturated at the highest measuring field of 5 T reaching a value of 89 Am^2Kg^{-1} at 2.5 K and 83 Am^2Kg^{-1} at 300 K, very close to value of bulk magnetite, confirming the high crystallinity of the MNPs achieved by this method.

The hyperthermic properties of both oxidized samples, **OlMNP1@90** and **OlMNP1@290**, were investigated recording the temperature kinetic curve of a toluene solution when exposed to an alternating magnetic field with amplitude 17 KAm^{-1} and frequency 183 KHz. The field parameters were set to stay below the human tolerance threshold, commonly assumed to be given by $H_0 \cdot \nu < 2 - 5 \cdot 10^9$ $A \cdot m^{-1} \cdot s^{-1}$ [11]. Larger amplitude or frequency may induce deleterious responses of living tissues and undesired side effects.

The hyperthermic efficiency of a given material is normally evaluate by the so-called Specific Absorption Rate, SAR, which is a measure of the absorbed power for mass unit [12]. The SAR can be evaluated by calorimetric technique, i.e. by measuring the temperature increase ΔT in the interval of time Δt of field application, using the formula $SAR = \frac{\sum_i m_i c_{pi}}{m_{Me}} \Delta T / \Delta t$, where, m_{Me} is the total mass of metal, m_i is the mass of the i-species present in the sample and C_{pi} its specific heat. Since the measurements are carried out in non adiabatic conditions, the ΔT / Δt values were extrapolated from the initial slope ($t \rightarrow 0$) of the temperature kinetic curves. Moreover, the time elapse Δt is chosen much shorter than the time constant of the external thermalization circuit.

The SAR values found for **OlMNP1@90** and **OlMNP1@290** were 4 Wg^{-1} and 24 Wg^{-1}, respectively (Figure 2.14). The difference in the heat dissipation efficacy among the two samples is a further confirmation that the oxidation process carried out at low temperature led to poor crystallinity, low magnetic moment and hence to bad hyperthermic properties.

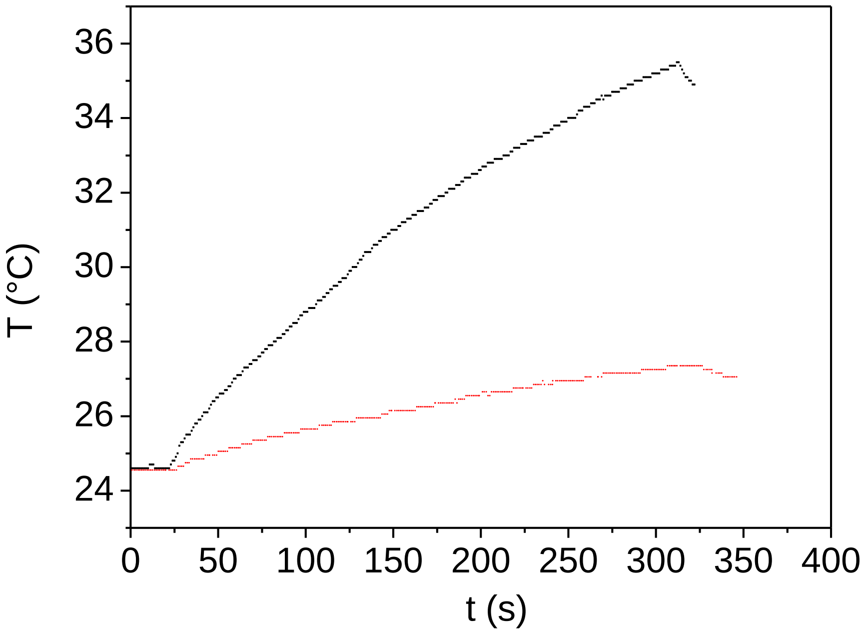

Figure 2.14 : Temperature kinetics of MNPs colloidal solutions in toluene : OlMNP1@90 (red, 1.2 % w/w) and OlMNP1@290 (black, 0.9 % w/w) during the exposure to the alternating magnetic field (17.0 kA/m, 183 kHz).

2.3 Synthesis of magnetite MNPs with Iron Acetylacetonate

As we have previously seen, the thermal decomposition of Fe(ole)$_3$ followed by an oxidation step can provide a final product with suitable structural an physical properties. However, despite of this positive aspect, this method still had some drawbacks that may affect its reproducibility. For instance, it has been recently shown that the properties of the final MNPs are dependent upon aging of the precursor [13]. Moreover, the use of a two steps process may be critical for the reproducibility. Therefore, we explored a third approach which uses iron(III) acetylacetonate as a precursor.

Iron(III) acetylacetonate (Fe(acac)$_3$) is a widely used precursor for the synthesis of magnetite MNPs [14]. However, a major drawback is represented by the difficulties in obtaining MNPs with size larger than 8-9 nm, in a single reaction step. However, it is known from the literature that, in order to have a sizable heating at magnetic field tolerable by human being, iron oxide MNPs must be at least larger than 10 nm [15]. In order to overcome this limitation we first attempted to increase the average size using the so-called seed mediated growth approach. This method consists in preparing small MNPs to be used as seeds to grow larger MNPs in a following thermal decomposition reaction with a further addiction of Fe(acac)$_3$ [16].

As an alternative approach, we explored the modification of experimental parameters from the solvent to the heating rate ramp, to increase the average size without compromising neither the crystalline quality, nor the magnetic properties.

2.3.1 Synthesis of MNPs exploiting the seed mediated growth process

The synthesis of magnetite MNPs exploiting the seed mediated approach starting from Fe(acac)$_3$ as precursor was performed as follows: first nearly cubic iron oxide MNPs, **IAMNP1**, with an average size of 7.6 ± 0.7 (Figure 2.15) nm were synthesized by thermal decomposition of Fe(acac)$_3$ in 1-octadecene and with oleic acid and oleylamine as surfactants.

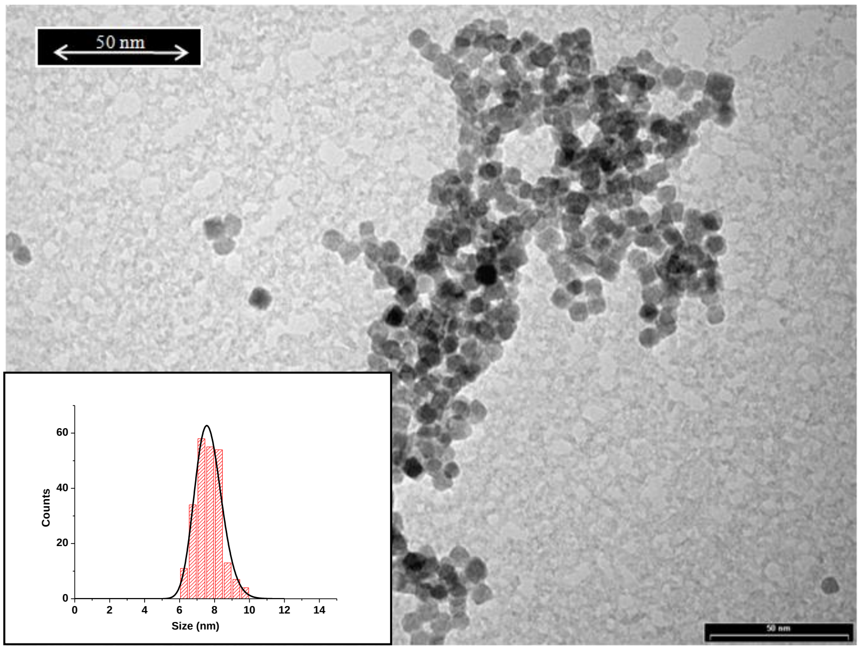

Figure 2.15 : TEM image of IAMNP1 (d = 7.6 ± 0.7 nm) used for the seed mediated growth process. In the inset, the size distribution evaluated over 300 MNPs is reported.

Then, the size of the inorganic core was increased by reacting the former MNPs with more Fe(acac)$_3$ under the same experimental conditions. TEM images of the final product **IAMNP2** show that an almost cubic shape was retained while the average size calculated along the diagonal increased to 11.3 ± 1.3 nm (Figure 2.16).

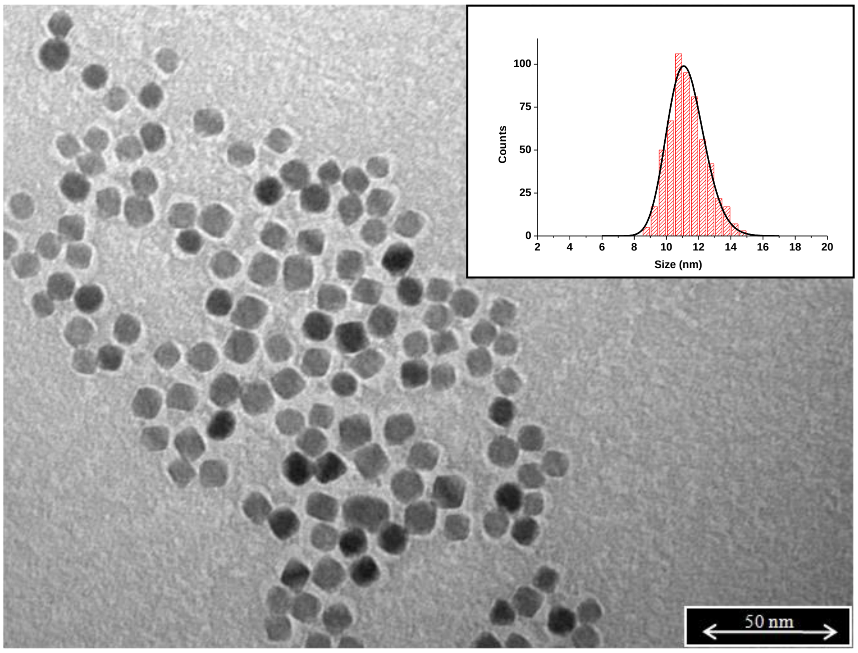

Figure 2.16 : image of IAMNP2 (d = 11.3 ± 1.2 nm) after the seed mediated growth process. In the inset the size distribution evaluated over 600 MNPs is reported.

The position and the relative intensity of all peaks observed in the powder XRD pattern (Figure 2.17) well match those of the fcc spinel structure of standard magnetite (PDF 19-0629), However, the lattice parameter, *a*, is 8.382(5) Å, much closer to that of magnetite (8.396 Å) than to maghemite (8.346 Å). Notably, no evidence of the presence of wüstite was found in the XRD pattern. The average diameter, evaluated by using the Scherrer's formula, was 11.5±0.8 in a good agreement with the particle sizes observed in TEM images, pointing out the single crystal nature and the high crystallinity of the MNPs.

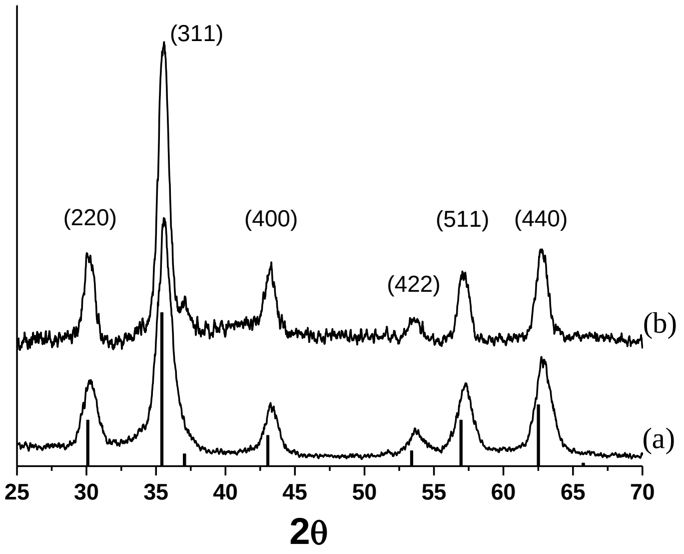

Figure 2.17 : Powder X-Ray Diffraction patterns of MNPs (a) IAMNP1, before and (b) IAMNP2, after the seed-mediated growth step. The black bars correspond to the reference magnetite pattern (PDF 19-0629).

The magnetic properties of a colloidal solution of the MNPs in heptane were investigated both as a function of temperature and magnetic field. Since these MNPs were used as multivalent scaffold for the functionalization with the α-Tn antigen mimetic, as it will be described in detail Chapter 3, their magnetic behaviours were deeply investigated. The temperature dependence of the magnetization recorded after zero-field cooling (ZFC) and field-cooling (FC) procedures is reported in Figure 2.18a. It displays the thermal irreversibility characteristic of an ensemble of randomly oriented single domain MNPs [17]: at room temperature all the particles are in the superparamagnetic regime, consistently with the relatively small size of the MNPs, while below ca. 100 K the two magnetization curves split, indicating the beginning of the freezing process of the MNPs magnetic moment. The blocking temperature, which at first approximation can be identified with the temperature of the maximum of the ZFC curve, was 50 K, which well agrees with that expected for magnetite MNPs of 11-12 nm [18]. Accordingly, an open hysteresis loop with a coercive field, H_C, of 34 mT, and reduced remnant magnetization, M_{0T}/M_{5T}, equal to 0.49 was measured at low temperature (2.5 K), while no magnetic irreversibility appears when the loop was measured above the blocking temperature (at 150 K and at room temperature, Figure 2.18b).

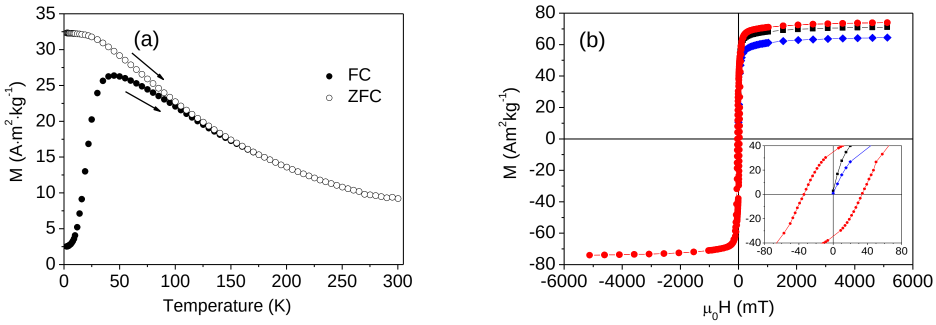

Figure 2.18 : (a) Temperature dependence of the ZFC and FC magnetizations collected on a colloidal solution of the surfactant coated MNPs in heptane with a probe field of 5 mT. (b) Hysteresis loops recorded at 2.5 K (red), 150 K (black) and 300 K (blue curve) and corresponding enlargement of the low field region (inset).

The magnetization was almost saturated at the highest measuring field of 5 T (the difference between the values measured at 5 T and those extrapolated from the fit of the high field data point to the empirical law $M = M_S + a/H + b/H^2$ is ca. 1 %) reaching 75 Am^2/kg at 2.5 K and then slightly decreasing on increasing temperature. The saturation magnetization resulted close to the literature value of the corresponding bulk materials confirming the single crystal nature and the high cristallinity of the inorganic cores.

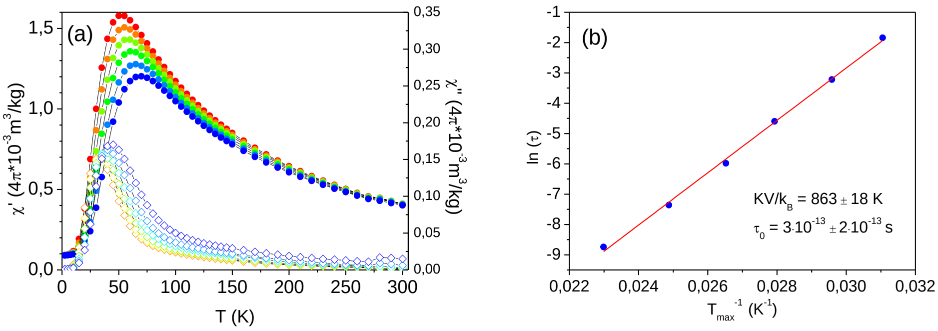

Figure 2.19 : AC susceptibilities and Arrhenius plot. (a) Temperature dependence of in-phase, χ', (full symbols) and out-of-phase, χ", (open symbols) AC susceptibilities. Data were collected at 6 log-spaced frequencies in the 1-1000 Hz range. (b) Arrhenius plot of the experimental relaxation time and best fit line.

The relaxation dynamics of the magnetic moment was further investigated by temperature-dependent AC susceptibility measurements at variable frequency (1-1000 Hz, Figure 2.19). Both the in- and out-of-phase components of the magnetic susceptibility exhibited frequency-dependent maxima characteristic of a blocking process. The blocking temperatures obtained from the maxima of the out-of-phase component of the magnetic susceptibility, χ”, for different observation times $\tau = 1/2\pi\nu$, where ν is the frequency of the ac field, can be effectively fitted to an Arrhenius law, $\tau = \tau_0 \exp(KV/k_BT)$, where K is the magnetic anisotropy energy density, V is the particle volume, τ_0 the attempt time and k_B the Boltzmann constant. The best-fit parameters found were $3\cdot10^{-13} \pm 2\cdot10^{-13}$s for the pre-exponential factor, τ_0, and 863 ± 18 K for the reversal energy barrier, KV/k_B, which, considering the average volume obtained from the analysis of TEM images, corresponds to $K \approx 2.2\cdot10^4$ J/m^3. Interestingly, no anomalies in the χ' *vs.* T curves were observed nor at the melting point of heptane (183 K), or at higher temperature, a result which indicates that at room temperature, at least in the investigated time window, the reversal of the magnetization is mainly driven by the Néel mechanism, rather than by the mechanical rotation of the whole MNPs. This result is particularly important in view of the possible application of these nanosystems in clinics. Indeed, since in our case the relaxation is determined by intrinsic magnetic parameters rather than on extrinsic parameters, as it would have been if the relaxation were dominated by Brownian motion of the nanoparticle, we can reasonably assume the observed behaviour will not change once the particles will be introduced in human tissue.

In order to evaluate the heat dissipation efficiency we recorded the temperature kinetic curve of the heptane colloidal solution when exposed to an alternating magnetic field with amplitude H_0 = 11.0 kA/m and frequency ν = 183 kHz. Also in this case, the field parameters were set to stay below the human tolerance threshold, commonly assumed to be given by $H_0\cdot\nu < 2 - 5\cdot10^9$ A$\cdot$m$^{-1}\cdot$s^{-1} [11]. The application of this alternating field on a 1.9 % w/w solution of the MNPs for 5 minutes produced a sizable temperature increase of ca. 9°C corresponding to a SAR value of ca. 10 W/g, as shown in Figure 2.20. Although this value is low if compared to data reported in the literature (which are however, commonly obtained using much higher, clinically unexploitable field amplitudes) it corresponds to a sizable heating efficiency, which suggests this material can be possibly used as heat mediator in adjuvant antitumoral therapy.

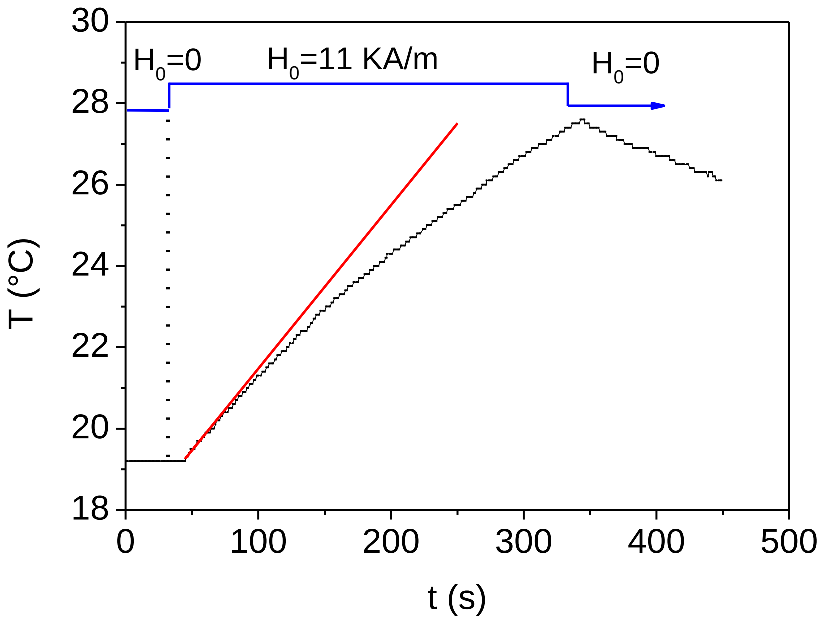

Figure 2.20 : Temperature kinetics of a colloidal solution of iron oxide MNPs during the exposure to the alternating magnetic field (11.0 kA/m, 183 kHz).

The low SAR value can be attributed both to the small size of the MNPs (which, for magnetite is close to the lower limit for producing sizable heat dissipation at these field parameters) and the presence of strained lattice regions that can alter the magnetic structure of the crystals creating a discrepancy between the crystal size and the effective magnetic volume. Pellegrino *et al.* had demonstrated that the origin of this crystal strain is strictly correlated with the seed mediated growth method [19]. This particular drawback turned our efforts toward the development of a procedure to synthesize larger magnetite MNPs in a single reaction avoiding any seeded process.

2.3.2 Synthesis of larger magnetite MNPs from iron(III) acetylacetonate

As mentioned in the previous paragraph, the synthesis of magnetite MNPs with size above 10 nm without exploiting the seed mediated growth process is often challenging and hard to achieve. Nevertheless, due to the intrinsic limitation of the seed growth method, we decide to make an effort to verify if by changing various experimental parameters in the thermal decomposition of $Fe(acac)_3$, ranging from the composition of the reaction mixture to the heating rate ramp, were possible to get magnetite MNPs with average size above 10 nm.

To realize this goal we maintained oleic acid and oleylamine as surfactants but changed the precursor/surfactant ratio and the reagents concentration. Both parameters are important in the nucleation and growing phase [20]. Differently from the previously described synthesis, in this case the employment of 1,2-hexadecanediol was avoided because, as demonstrated by Barron *et al.*, it promotes the formation of small sized MNPs, meanwhile not providing any advantage in terms of polydispersity index [21]. Moreover, the reaction solvent was changed from 1-octadecene (b.p. 320°C) to benzyl ether (b.p. 298°C) thus facilitating the MNPs purification from the reaction mixture. The removal of octadecene residues is indeed more difficult causing a larger consumption of hexane and ethanol for the purification process.

The first two experiments were performed with a Fe(acac)$_3$/oleic acid/oleylamine ratio equal to 1 : 4.5 : 3.5 in 50 mL of benzylether, varying t_i (the time spent to reach reflux condition) and t_r (reflux time) in the heating rate ramp as described in Figure 2.21.

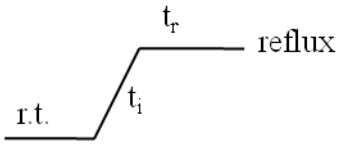

IAMNP3 : t_i=50' and t_r=50'

IAMNP4 : t_i=20' and t_r=40'

Figure 2.21: Heating ramp employed for the synthesis of samples IAMNP3 and IAMNP4 where t_i represents the time spent to reach reflux condition and t_r the reflux time.

The XRD patterns of both samples, shown in Figure 2.22, well match that of the fcc spinel structure of magnetite (PDF 88-0315) and no traces of any other crystal phase appears confirming that the use of Fe(acac)$_3$ as precursor avoid the formation of any undesired phase like wüstite or hematite.

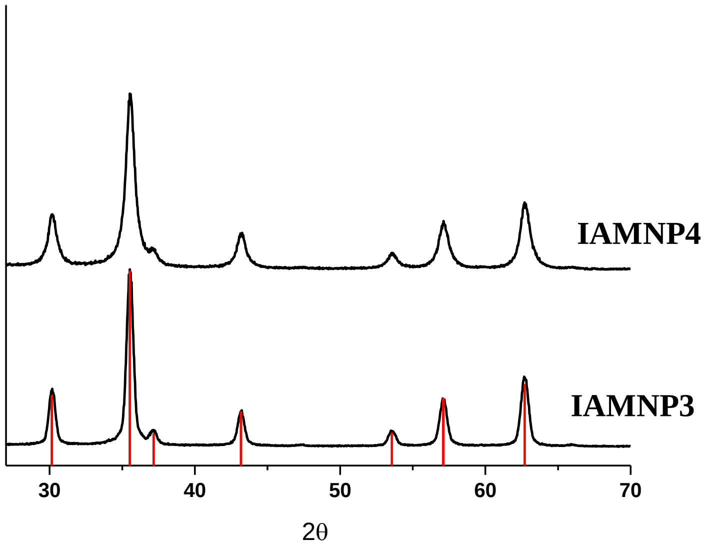

Figure 2.22 : XRD patterns of samples IAMNP3 and IAMNP4. In red the reference pattern of magnetite (PDF 88-0315) is shown.

From the TEM images shown in Figure 2.23 it is possible to observe that sample **IAMNP3** was mostly composed by faceted polyhedral nanocrystals with an average size of 20.7 ± 2.6 nm whereas MNPs in sample **IAMNP4** had an almost spherical shape with a mean size of 7.3 ± 2.0 nm: the transition from the spherical to a faceted polyhedral morphology is usually found in MNPs bigger than 15-16 nm. In the case of sample **IAMNP3** the longest t_i and t_r times favored the growth step with respect to nucleation, thus leading to the formation of MNPs bigger than 20 nm, grown along the most favorable crystallographic directions. Conversely, the shortening of t_i in sample **IAMNP4**, smaller MNPs were achieved. In both cases the large size distribution can be attributed to the inadequate separation between the nucleation and the growing phases.

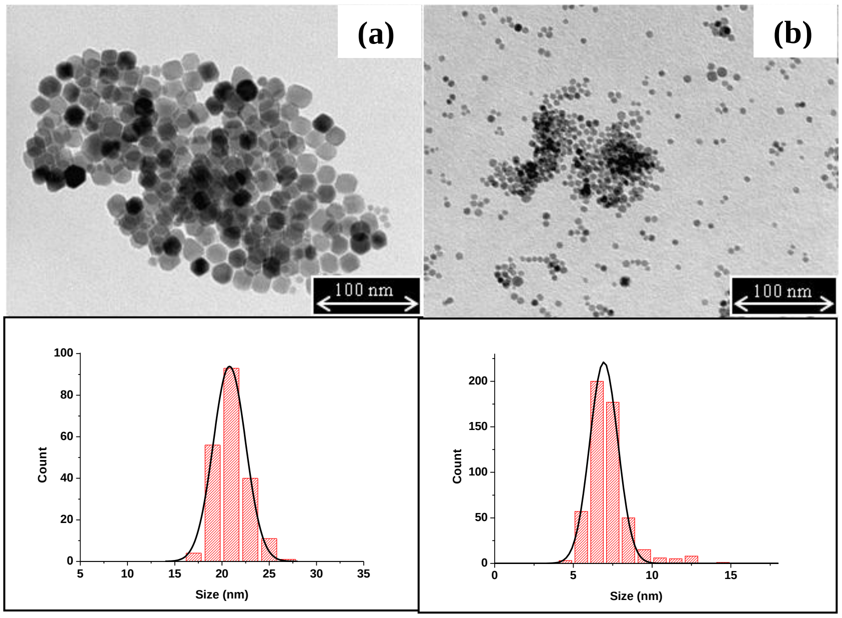

Figure 2.23 : TEM images ad size distribution of samples a) IAMNP3 (d=20.7 ± 2.6 nm) and b) IAMNP4 (7.3 ± 2.0 nm). The size distribution was evaluated over 300 MNPs.

Therefore, an intermediate, 20 minutes long, step at 200°C was added in order to improve the monodispersity of the MNPs [22]. The separation between nucleation and growth phases, which occur at different temperatures, is a critical issue for the formation of nanocrystals of the desired size. Three experiments were performed maintaining the same Fe(acac)$_3$/oleic acid/oleylamine ratio equal to 1 : 4.5 : 3.5 in a two-fold more diluted reaction mixture in comparison to the previous experiments. The time t_r at which each reaction was maintained at the reflux temperature was increased from 15' to 1.5 h as described in Figure 2.24.

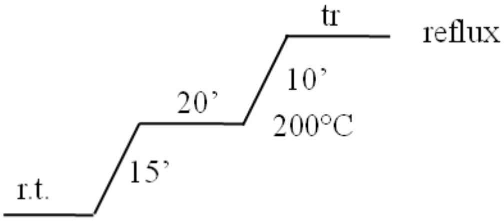

IAMNP5 : t_r=15'

IAMNP6 : t_r=40'

IAMNP7 : t_r=1.5 h

Figure 2.24 : Heating rating ramp employed for the synthesis of samples IAMNP5, IAMNP6 and IAMNP7. t_r represents the reflux time.

The three XRD patterns of the as synthesized samples well match the reference pattern of magnetite (PDF 88-0315) as shown in Figure 2.25.

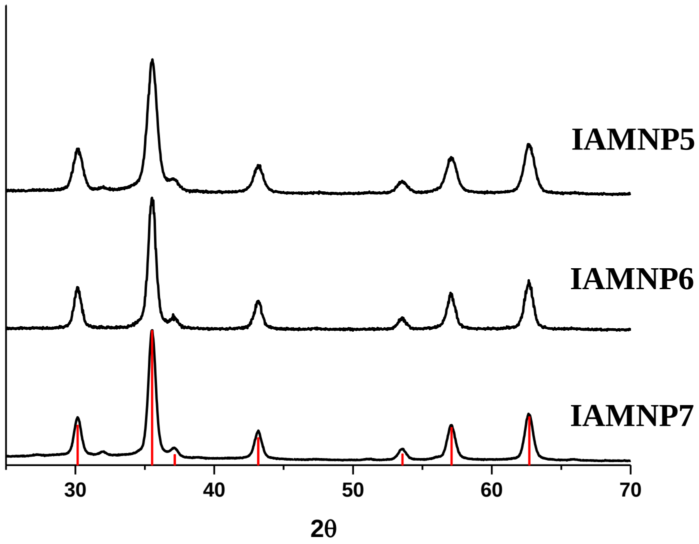

Figure 2.25 : XRD patterns of samples IAMNP5, IAMNP6 and IAMNP7. In red the reference pattern of magnetite (PDF 88-0315).

The average diameters, evaluated by using the Scherrer's formula for samples **IAMNP5**, **IAMNP6** and **IAMNP7** were respectively 10.8±0.2 nm 13.8±0.2 nm, and 14.5±0.2 nm, in a good agreement with the particle sizes observed in TEM images, pointing out the single crystal nature and the high crystallinity of the MNPs.

In Figure 2.26 are shown the TEM images of the three samples and their size distributions.

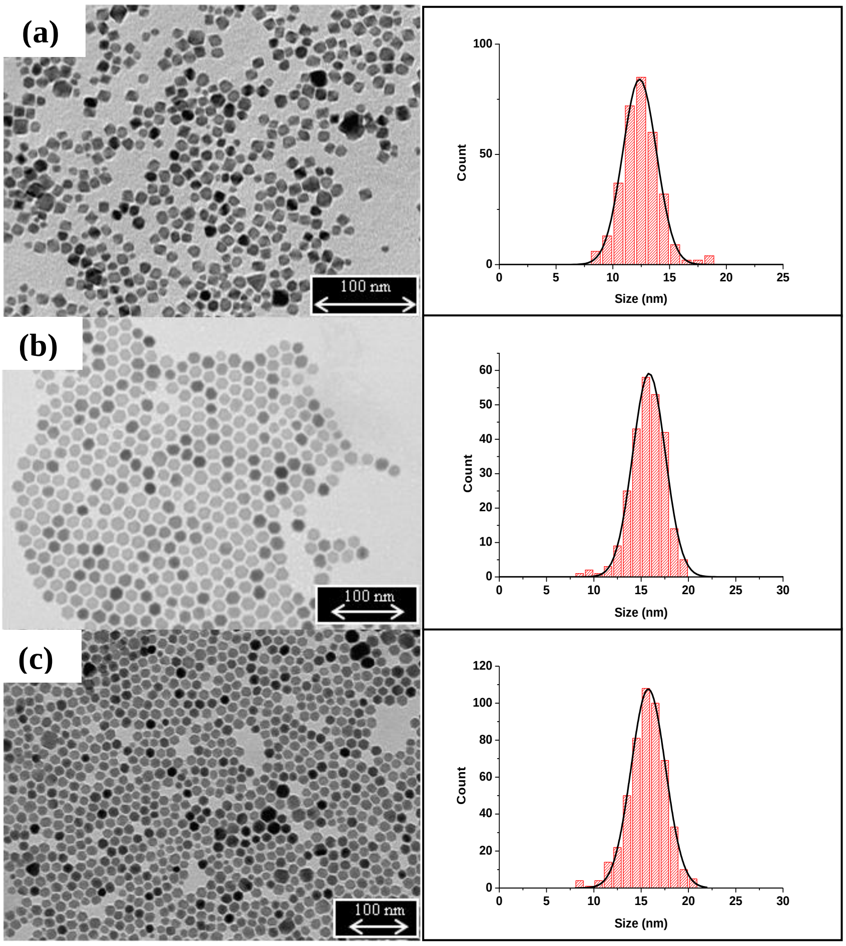

Figure 2.26 : TEM images and size distributions of samples a) IAMNP5 (d = 12.4 ± 1.6 nm) b) IAMNP6 (d = 15.7 ± 1.7 nm) and c) IAMNP7 (d = 15.6 ± 1.9 nm) . The size distribution was evaluated over more than 300 MNPs for samples a and b, and over 500 MNPs for sample c.

The size increase was achieved increasing the t_r from 15' to 40' going from 12.4 ± 1.6 nm for sample **IAMNP5** to 15.7 ± 1.7 nm for sample **IAMNP6**. A further increase of t_r to 1.5h did not affect the size of the synthesized MNPs. A better size distribution was obtained for these samples in comparison to carrying on the reaction set up without the intermediate step at 200°C. Moreover, a heating ramp divided in two steps allowed for a better control on MNPs size and size distributions.

Based on these last results, the reaction was modified by the introduction of a longer heating step at 200°C in order to promote only the formation of nuclei and better separating it from the growth step which occurs in the following step at a higher temperature. In this way the final size is determined by the length of the reflux time only.

The intermediate step was thus extended to one hour and t_r was equal to 30'. The other experimental parameters were kept unaltered.

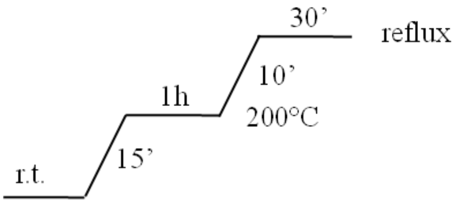

Figure 2.27 : Heating rate ramp used for the synthesis of sample IAMNP9.

The MNPs **IAMNP9** obtained using this heating ramp were structurally characterized by x-ray diffraction spectroscopy and transmission electron microscopy. Also in this case the XRD pattern, displayed in Figure 2.28, well match those of the fcc spinel structure of magnetite (standard: PDF 88-0315) and no traces of wüstite or hematite were found.

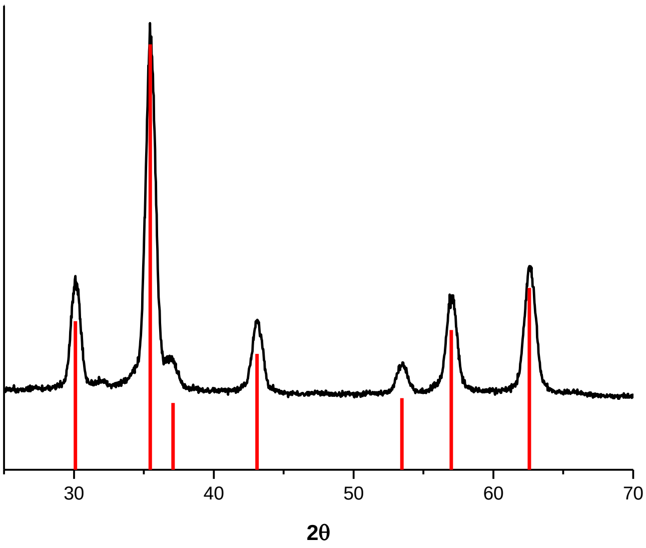

Figure 2.28 : Pattern of sample IAMNP9. The red lines corresponds to the magnetite reference (PDF 88-0315).

The TEM images showed uniform MNPs with an average diameter of 13.9 ± 1.0 nm and a highly narrow size distribution. All the MPs had a regular, almost spherical, faceted shape, which suggested a slow growth of the nanocrystals and a high crystallinity (Figure 2.29). Indeed, the Scherrer analysis of peak broadening of XRD pattern revealed an average crystal size of 10.9(0.2) nm.

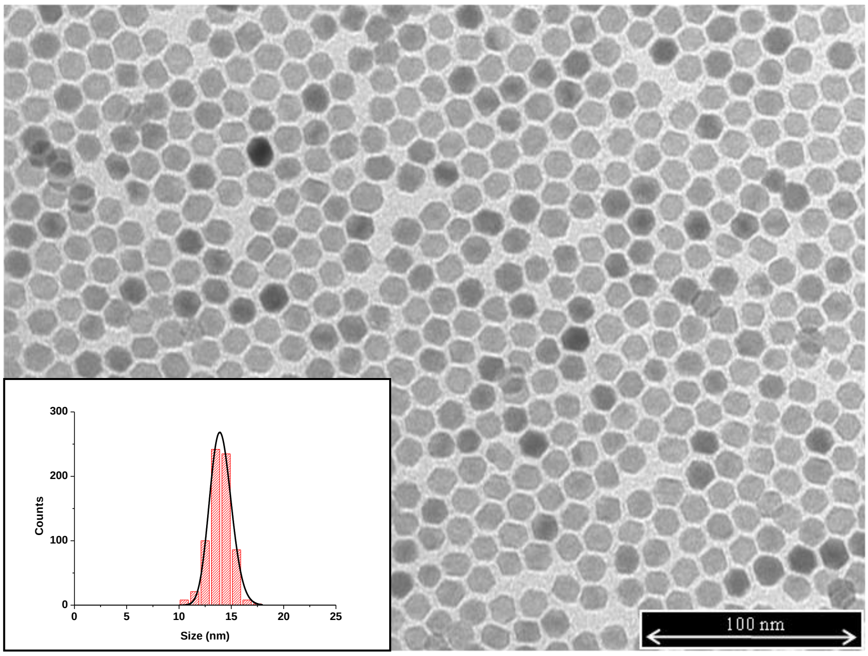

Figure 2.29 : TEM image of IAMNP9 (d = 13.9 ± 1.0 nm). In the inset the size distribution evaluated over 700 MNPs is reported.

In this case the good size distribution can be attributed to the adequate length of the intermediate step employed, which guarantee the separation between the nucleation and the growth phases. Moreover, using a reflux time of 30' allowed to stop the growth of the MNPs at the optimal size of ca. 14 nm, before they could become bigger and thus less soluble because of the increased interparticle dipolar interaction.

In Figure 2.30 the hysteresis loop recorded between ±5 T are shown. An open hysteresis loop was measured at 2.5K with a coercive field H_C of 24 mT, and a reduced remnant magnetization, M_{0T}/M_{5T}, equal to 0.37. No magnetic irreversibility was observed in the hysteresis loop measured at 300K. The magnetization was saturated from 2 T and reached 88 Am^2/kg at 2.5 K, close to the corresponding value of the bulk material. These magnetic behaviours confirmed the single crystal nature and the high crystallinity of the as prepared magnetite MNPs.

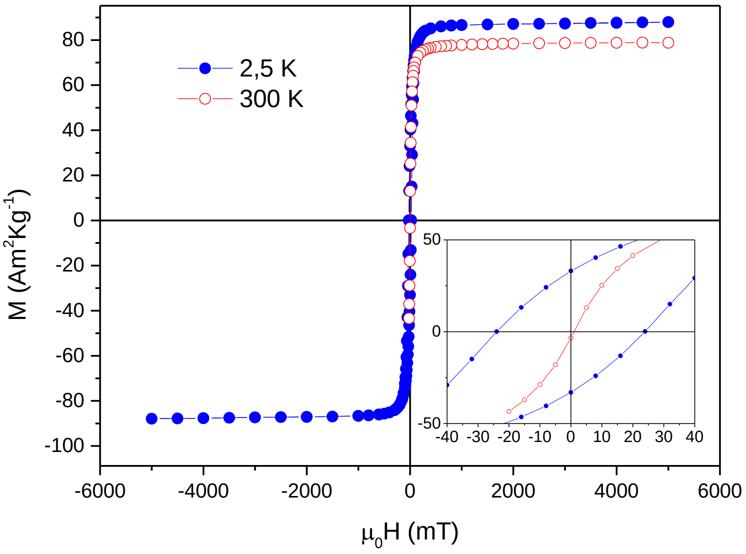

Figure 2.30: Hysteresis loop of MNPs IAMNP9 recorded at 2.5K (blue dotted line) and at 300 K (red dotted line) and corresponding enlargement of the low field region.

In order to have a complete characterization of this sample, the heat dissipation efficiency under an alternating magnetic field with an amplitude of 17 KAm^{-1} and a frequency of 183 KHz was measured giving a SAR value of 16 W/g, a good result if the relatively small size of the MNPs (14 nm) is taken into account (Figure 2.31).

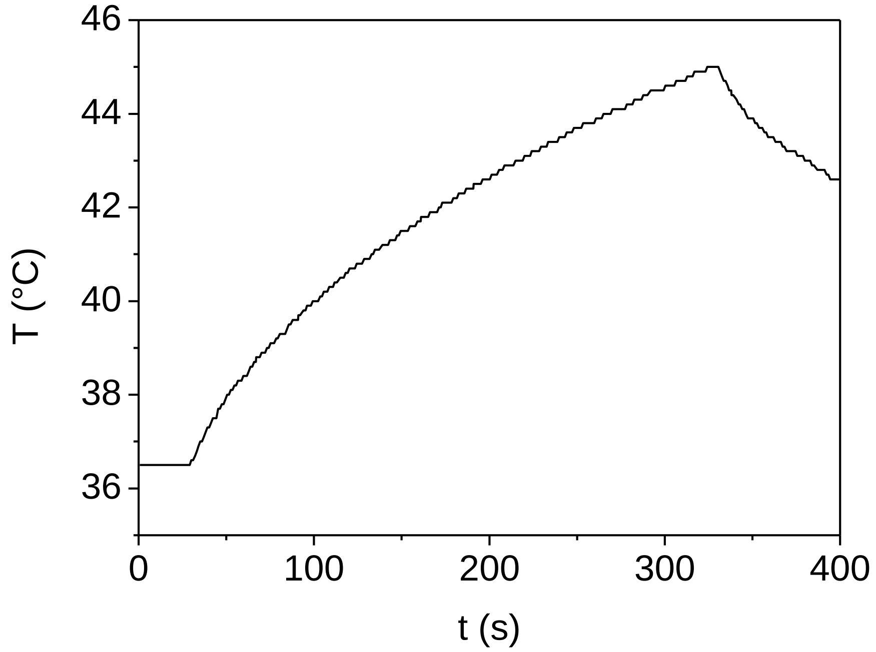

Figure 2.31 : Temperature kinetics of IAMNP9 colloidal solutions in toluene (1.2% w/w) during the exposure to the alternating magnetic field (17.0 kA/m, 183 kHz).

We can thus conclude that the last experimental conditions correspond to the best suited setting to obtain magnetite MNPs to be used for the application proposed in this work. As a matter of fact, this particular size represents the best compromise between magnetic/hyperthermic properties and colloidal stability. Indeed, it has been shown that for fixed field parameters, the specific loss power is strongly size-dependent and it reaches a maximum for a size that, for magnetite MNPs is ca. 18 nm . However, the stability of magnetite MNPs with size over 15-16 nm is low affecting the following ligand exchange reactions.

References

[1] (a) A.G. Roca; R. Costo *et al.*, *J. Phys. D:Appl. Phys.*, **2009**, *42*, 224002; (b) P. Tartaj; M.P. Morales et al., *J. Phys. D: Appl. Phys.*, **2003**, *36* R182.

[2] (a) P. Saravanan; R. Gopalan; V. Chandrasekaran; *Defence Science Journal*, **2008**, *58*, 4, 504; (b) S. Sun; H. Zeng; *J. Am. Chem. Soc.*, **2002**, *124* (28), 8204.

[3] (a) T. Hyeon, *Chem. Commun.*, **2003**, *927* and cited articles; (b) T. Hyeon *et al.*, *Angew. Chem. Int. Ed.*, **2005**, *44*, 2872 e and cited articles.

[4] L. Calero-DdelC; A. N. Gonzalez; C. Rinaldi; *Journal of Manufacturing Science and Engineering*, **2010**, *132*, 030914-1 e and cited articles.

[5] E. Peng; J. Ding; J. M. Xue; *J. Mater. Chem.*, **2012**, *22*, 13832.

[6] (a) F. J. Morin, *Phys. Rev.*, **1950**, *78*, 819; (b) Ö. Özdemir, D. J. Dunlop, T. S. Berquò, *Geochem. Geophys. Geocyst*, **2008**, *9*, 10, 1.

[7] (a) S.G. Kwon; Y. Piao; J. Park; S. Angappane; Y. Jo; N.-M. Hwang; J.-G. Park; T. Hyeon, *J. Am. Chem. Soc.* **2007**, *129*, 12571; (b) S. G. Kwon; T. Hyeon, *Acc. Chem. Res.* **2008**, *41*, 1696; (c) C.-J. Chen; R.-K. Chiang; H.-Y. Lai; C.-R. Lin, *J. Phys. Chem. C*, **2010**, *114*, 4258.

[8] T. Hyeon *et al.*, *Nature Materials*, **2004**, *3*, 891.

[9] P. Scherrer, *Göttinger Nachrichten*, **1918**.

[10] R. M. Cornell; U. Schwertmann, *The Iron Oxides*; VCH: Weinheim, Germany, **1996**.

[11] R. Hergt, S. Dutz *et al.*, *J. Phys.: Condens. Matter.*, **2008**, *20*, 385214.

[12] W. Andrä; H. Nowak, (Eds.), *Magnetism in Medicine. A Handbook*, Wiley-VCH Verlag, Berlin, **1998**.

[13] A. P. Herrera; L. Polo-Corrales; E. Chavez; J. Cabarcas-Bolivar; O. N. C. Uwakweh; C. Rinaldi, *J. Magn. Magn. Mater.*, **2013**, *328*, 41.

[14] (a) Q. A. Pankhurst, N .K. T. Thanh *et al.*, *J. Phys. D: Appl. Phys.*, **2009**, *42*, 224001; (b) S. Sun and H. Zeng, *J. Am. Chem. Soc.*, **2002**, *124*, 8204.

[15] L. Lartigue; C. Innocenti; T. Kalaivani; A. Awwad; M. del Mar Sanchez; Y. Guari; J. Larinova; C. Guérin; J. L. G. Montero; V. Barragan-Montero; P. Arosio; A. Lascialfari; D. Gatteschi, C. Sangregorio, *J. Am. Chem. Soc. J. Am. Chem. Soc.* **2011,** *133*, 10459.

[16] S. Sun; H. Zeng; *J. Am. Chem. Soc.*, **2002**, *124* (28), 8204.

[17] L. Néel, , *Ann. Geophys.* **1949**, *5*, 99.

[18] M. F. Casula; P. Floris; C. Innocenti; A. Lascialfari; M. Marinone; M. Corti; R. A. Sperling; W. J. Parak; C. Sangregorio, *Chem. Mater.*, **2010**, *22*, 1739.

[19] M. Levy; A. Quarta; A. Espinosa; A. Figuerola; C. Wilhelm; M. García-Hernandez; A. Genovese; A. Falqui; D. Alloyeau; R. Buonsanti; P. D. Cozzoli; M. A. García; F. Gazeau and T. Pellegrino, *Chem. Mater.*, **2011**, *23*, 4170.

[20] (a) W. W. Yu, J. C. Falkner, C. T. Yavuz, V. L. Colvin, *Chem. Commun.*, **2004**, 2306. (b) M. Yin, A. Willis, F. Redl, N. J. Turro, S. P. O'Brien, *J. Mater. Res.*, **2004**, *19* (4), 1208. (c) E. Kang, J. Park, Y. Hwang, M. Kang, J. G. Park, T. Hyeon, *J. Phys. Chem. B*, **2004**, *108*, 13932. (d) X. Teng, H. Yang, *J. Mater. Chem.*, **2004**, *14*, 774.

[21] C. A. Crouse; A. R. Barron, *J. Mater. Chem.*, **2008**, *18*, 4146.

[22] P. Guardia; J. Pérez-Juste; A. Labarta; X. Batllea and L. M. Liz-Marzan, *Chem. Commun.*, **2010**, *46*, 6108.

3. The α-Tn antigen mimetic and functionalization of MNPs

As previously mentioned in Chapter 1, one of the main goal of this work was to realize a nanostructured system for the multivalent presentation of the TACA α-Tn antigen [1] exploiting a versatile scaffold represented by MNPs. In paragraph 3.1, the nature and role of α-Tn antigen is discussed, whereas in the following paragraphs 3.2, 3.3, 3.4 we describe the synthesis of the α-Tn antigen mimetic modified so as to be anchored to the MNPs surface, and in paragraph 3.5, details concerning the functionalization of MNPs with the mimetic are reported.

3.1 The α-Tn antigen

Tumours uniquely or excessively express antigens (tumour associated antigens, TAAs) and, in particular, glycan antigens (tumour associated carbohydrate antigens, TACAs), which can be exploited as targets for vaccines. Among the large numbers of TACAs we focused our efforts on the study of the α-Tn antigen which is expressed in carcinoma associated mucins [2]. Structurally the α-Tn antigen is a *N*-acetylgalactoseamine (GalNAc) bound through an α-*O*-glycosidic linkage to a serine (Ser) or a threonine (Thr) residue (Figure 3.1) of the protein backbone of a particular family of glycoprotein, called mucins. Mucins are heavily O-glycosilated extracellular proteins forming a major part of the protective biofilm on epithelial cells and providing a protective barrier against dangerous chemicals or microbials [3].

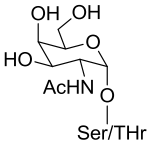

Figure 3.1 : Structure of the α-Tn antigen.

Mucins play several physiological roles acting as a "lubricant" towards the internal organs thanks to their density and viscosity: Moreover, they can play the role of receptor/sensor transmitting signals in response to external stimuli and inducing a proper cellular reaction. However, a mucin over expression matches the pathogenesis of cancer, particularly of adenocarcinomas, and harmfully influences cellular growth, adhesion, and also the immune surveillance [3]. Mucins, when abnormally over expressed, can undergo an incomplete glycosylation leading to an exposure of tumour associated epitopes on the surface of the tumour cells. The α-Tn antigen is one of the truncated forms of the *O*-glycan chains expressed on cancer cells as displayed in Figure 3.2, and this is why it is considered a promising target for cancer immunotherapy. Noteworthy the α-Tn antigen due to its structural simplicity has been a privileged synthetic target for vaccine development [2].

a) Mucins in healthy cells

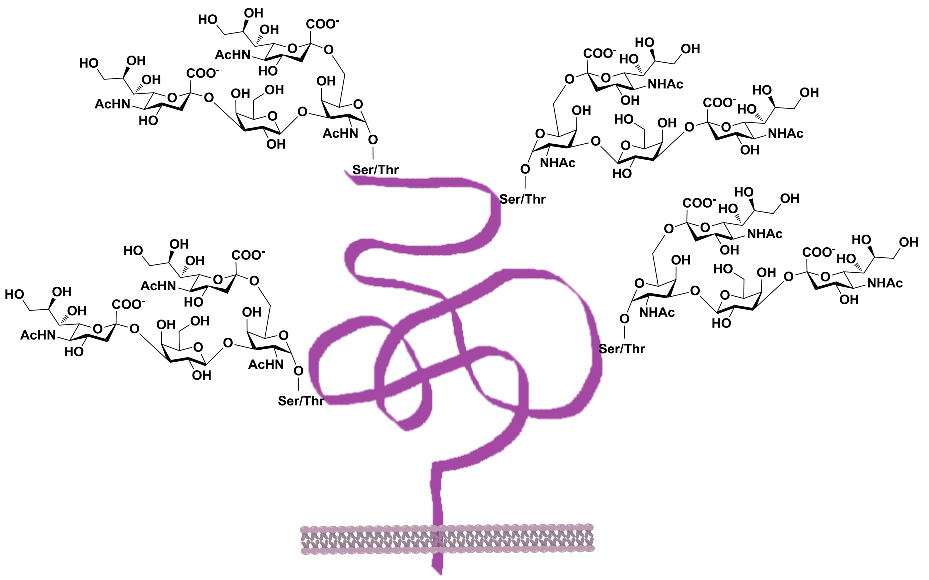

b) Mucins in cancer cells

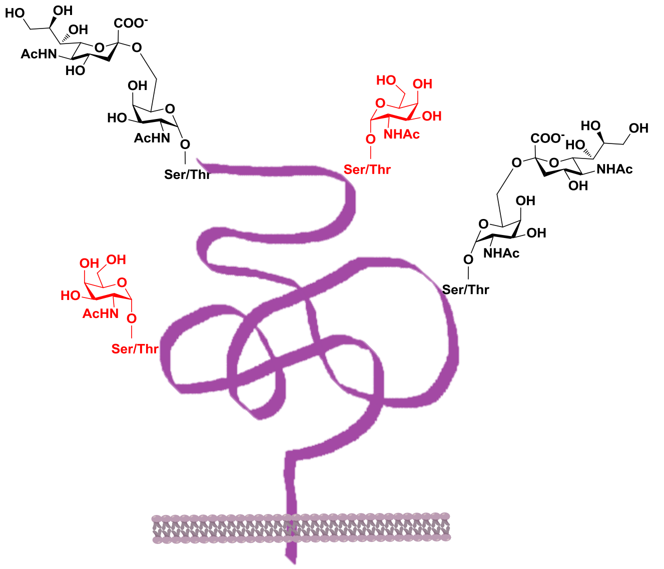

Figure 3.2 : Mucins are heavily glycosylated proteins but during carcinogenesis incomplete glycosylation occurs resulting in TACAs exposure. Certain types of cancer cells express truncated forms of *O*-glycan chains and one of them is the α-Tn antigen.

Our efforts in this field have been directed towards the binding of a stable mimetic of the α-Tn antigen **2** (Figure 3.3) to multivalent scaffolds mimicking the natural multivalent approach of the biosystems in order to induce an efficient antitumour immune response. The development of bioactive mimetics relies on the fact that a variety of vaccines based on native TACAs, such as α-Tn, have shown low immunogenicity, low *in vivo* stability and poor bioavailability, giving rise to the necessity of improving their stability against chemical and enzymatic hydrolysis, as well as of their bioavailability compared to natural materials.

3.2 Synthesis of the α-Tn antigen mimetic 2

As described in the previous paragraph the native form of the α-Tn antigen **1** consists of a N-acetyl galactosamine α-O-linked to a serine (Ser) or a threonine (Thr) residue to the peptide backbone. The main challenge of any synthetic approach reported for the α-Tn antigen was represented by the stereoselective formation of the α-*O*-glycosidic linkage between the GalNAc and Ser/Thr derivatives [4].

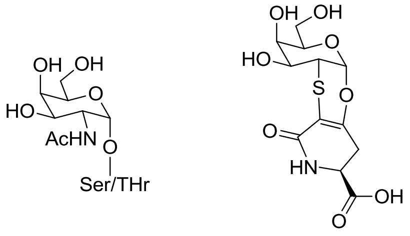

1 **2**

Figure 3.3 : Structures of the α-Tn antigen 1 and the α-Tn antigen mimetic 2.

The research group of Prof. C. Nativi has recently developed a diastereoselective synthesis of a rigid mimetic of the α-Tn antigen, **2**, (Figure 3.3) relying on the efficient inverse electron-demand Diels-Alder reaction between the glycals and the α-α'-dioxothiones, as outlined in Scheme 3.1 [5]**.** This mimetic maintains the key structural features of the natural α-O-glycopeptide and presents a suitable carboxylic functional group for the insertion of a desired linker or carrier [6]. Furthermore, the structurally rigid compound **2** preserves the $^4C_1$ conformation and it is recognized by viscumin album agglutinin (VAA), a lectin which selectively binds galactose residues and competes with lactose, a common ligand for VAA known to enter the lectin sites, in competitive STD experiments [6]. Moreover, it has been recently demonstrated that the mimetic **2** if properly functionalized, was able to induce a strong and long-lasting Tn-specific response, with IgM/IgG antibodies able to recognize native carbohydrate antigens, confirming its importance in the development of anticancer vaccines [7].

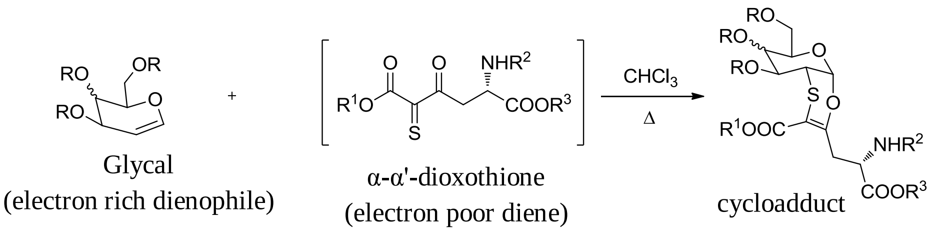

Scheme 3.1 : Inverse electron-demand Diels-Alder reaction between glycals and α-α'-dioxothiones leading to the diastereoselective formation of the α-*O*-glycosides.

The strategy adopted to decorate the MNPs in a multivalent manner with the α-Tn like epitope **2,** is based on the synthesis of compound **3** starting from the peracetylated Tn-like derivative **4.** Then in order to exploit the large affinity of phosphonate group [8] for the iron oxide surface of the MNPs, compound **3** was coupled with the hexaethylene glycol derived linker **5**, whose terminal amino group was later replaced by a phosphonate moiety, as outlined in the Scheme 3.2.

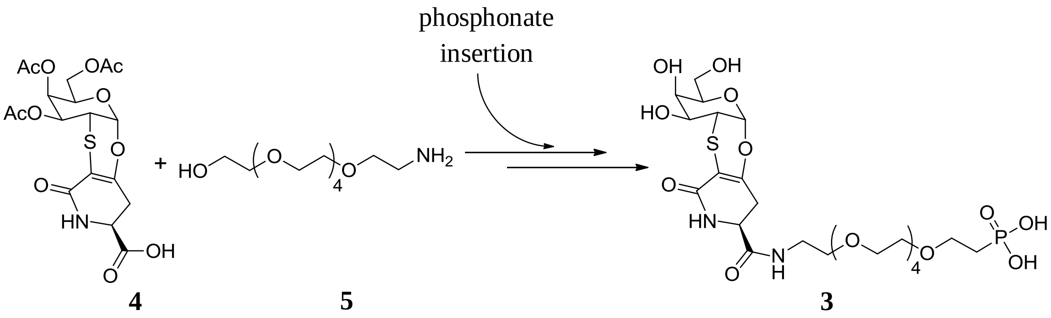

Scheme 3.2 : General scheme for the synthesis of the α-Tn like derivative 3 from the peracetylated Tn-like derivative 4 and the linker 5.

In this paragraph the synthesis of compound **4** will be described, whereas the synthesis of compounds **5** and **3** will be described in paragraphs 3.3 and 3.4, respectively.

In Scheme 3.3 the complete synthesis of the peracetylated α-Tn antigen mimetic **4** is reported.

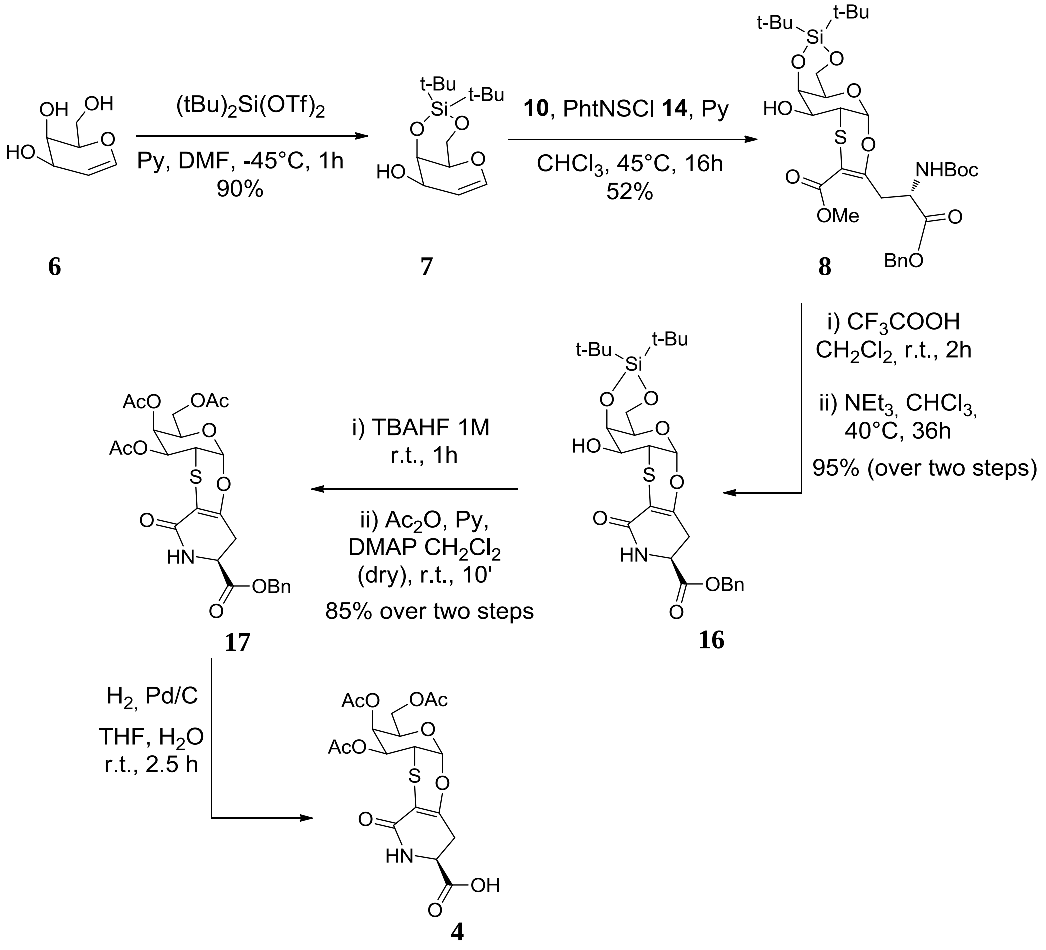

Scheme 3.3 : Complete reaction scheme for the synthesis of the peracetylated α-Tn antigen mimetic 4.

The D-galactal **6** was reacted with di-*tert*-butylsylyltriflate ($(tBu)_2Si(OTf)_2$) affording compound **7** in 90% yield. In this step the hydroxyl groups in positions four and six were simultaneously protected as silyl ether. The hydroxyl in position three was kept unprotected in order to avoid an increase in steric hindrance on the α face of the dienophile that could negatively affect the selectivity in the subsequent cycloaddiction reaction.

The inverse electron-demand Diels Alder reaction that afforded the cycloadduct **8** needs to be discussed in detail. The protected D-galactal **6** represented the electron rich dienophile whereas the electron poor diene **9** was generated *in situ* from its precursor, the β-ketoester, **10**, under the same reaction conditions of the cycloaddiction reaction. Indeed, the α-α'-dioxothione **9** is unstable and hence impossible to isolate. Compound **10** was prepared exploiting the reaction of aspartic acid, **11**, bearing the amine group protected with the *tert*-butyloxycarbonyl group (Boc) and the carboxylic group protected as benzyl ester with the Meldrum acid **12** in the presence of isopropylchloroformiate (IPCF) to form the corresponding adduct **13**. Then by heating **13** in a 4:1 mixture of benzene/methanol, the β-ketoester **10** was obtained (Scheme 3.4) [5].

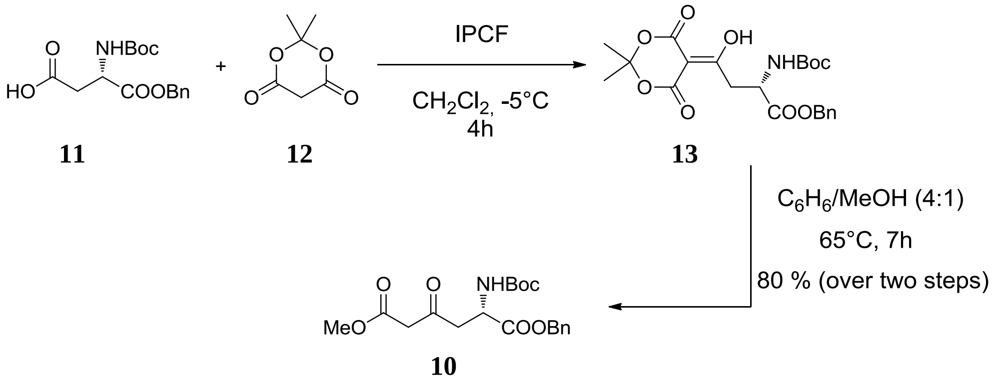

Scheme 3.4 : Synthesis of the β-ketoester 10, precursor of the α-α'-dioxothione 9 acting as electron rich dienophile in the inverse electron-demand Diels Alder reaction.

The formation of the α-α'-dioxothione **9** was thus achieved by reaction of **10** with phthalimidesulfenyl chloride (PhtNSCl) **14** [5] in basic conditions in the presence of the dienophile, that is the experimental condition of the cycloaddiction reaction, as described in the following scheme 3.5:

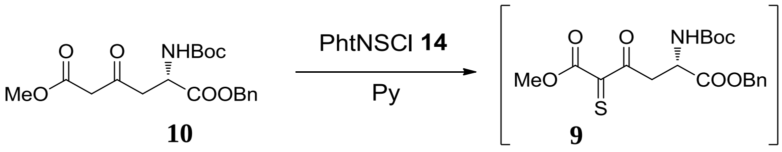

Scheme 3.5 : ***In situ*** **formation of the α-α'-dioxothione 9 in the presence of phtalimidesulfenyl chloride 14 under basic conditions.**

Phthalimidesulfenyl chloride **14** was prepared by heating *N*-*N*'-dithiobisphtalimide **15** with sulfurilchloride.

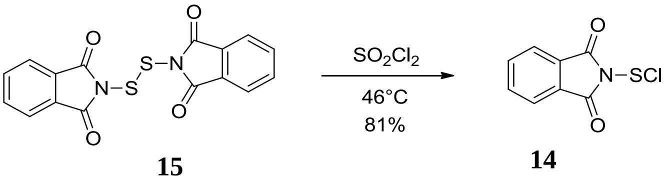

15 **14**

Scheme 3.6 : Preparation of the phtalimidesulfenyl chloride 14.

The Diels Alder reaction between the dienophile **7** and the diene **9** generated *in situ* afforded the pure diasteromeric cycloadduct **8** in 52% yield (Scheme 3.6). This cycloaddition is characterized by:

- chemoselectivity: the α-α'-dioxothione reacts selectively with the C=S and the ketonic C=O;
- regioselectivity: the preferred orbital interactions are those between the C=S and the galactal C-2 and those between the ketonic C=O and the C-1;
- stereoselectivity: the interaction occurs involving the lower face of the dienophile (α face).

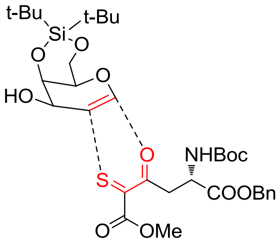

Figure 3.4 : Representation of the regio, chemo and stereo selectivity of the inverse electron-demand Diels Alder reaction.

All these features led to the formation of the oxathiin ring presenting the α-O-glycosidic linkage and a proper orientation of the amino acid moiety with respect to the galactosidic counterpart, which are the main characteristics for the α-Tn antigen mimetic. Then, a treatment of **8** with trifluoroacetic acid enabled the removal of the Boc protecting group without affecting the silylidene protecting group on the galactose moiety, leaving a free amino functionality that under basic conditions (triethylamine, NEt_3) allowed the intramolecular cyclization to give the tricyclic lactam **16** in a 95% yield (calculated over two steps). As a consequence of the formation of the lactam ring, the COOBn group is located in the same portion of space occupied by the carboxylic group of the Ser or Thr in the native α-Tn antigen, confirming the mimetic properties of this tricyclic scaffold.

The compound **16** was first treated with a freshly prepared 1M solution of tetrabutylamonium hydrogen fluoride (TBAHF) in THF in order to remove the sylilidene protecting group [9] and then reacted with acetic anhydride and pyridine to form the peracetylated derivative, **17,** in 85 % yields over the two steps. The final removal of the benzyl ester was performed by palladium catalyzed hydrogenation affording the unprotected carboxyl derivative, **4**. The free carboxylic group will be coupled with the linker **5** which synthesis is described in the following paragraph.

3.3 Synthesis of the linker 5

The choice of hexaethylene glycol **18** as starting material for the synthesis of the linker was dictated by two particular properties:

- it confers good water solubility to the final product [10];
- it ensures an optimal presentation of the α-Tn epitopes towards the external environment after the anchorage to the surface of the MNPs.

The complete synthesis of the linker monoaminohexaethylenglycol **5** is reported in scheme 3.7.

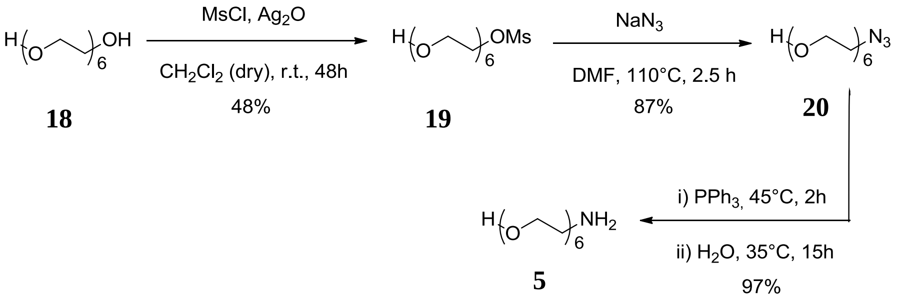

Scheme 3.7 : Scheme of the synthesis of the linker 5.

Compound **19** was prepared from commercially available hexaethylene glycol **18** by reaction with methanesulfonyl chloride (MsCl) using freshly prepared Ag_2O as a base. This procedure led to the formation of the monomesylate derivative as major product, in 48% yield. The azido functional group was inserted by reaction of **19** with sodium azide to form **20** in 87% yield [11]. By reducing the azide **20** under Staudinger conditions, the product **5** was obtained in 97% yield. The so synthesized linker with the free amino group was employed for the coupling reaction with **4**.

3.4 Synthesis of the α-Tn like derivative 3 : coupling reaction and phosphonate insertion

Once the two moieties were prepared, the final step consisted in the coupling between the acetylated α-Tn mimetic **4** and the linker **5** followed by the insertion of the phosphonate group to obtain the derivative **3**, as shown in Scheme 3.8.

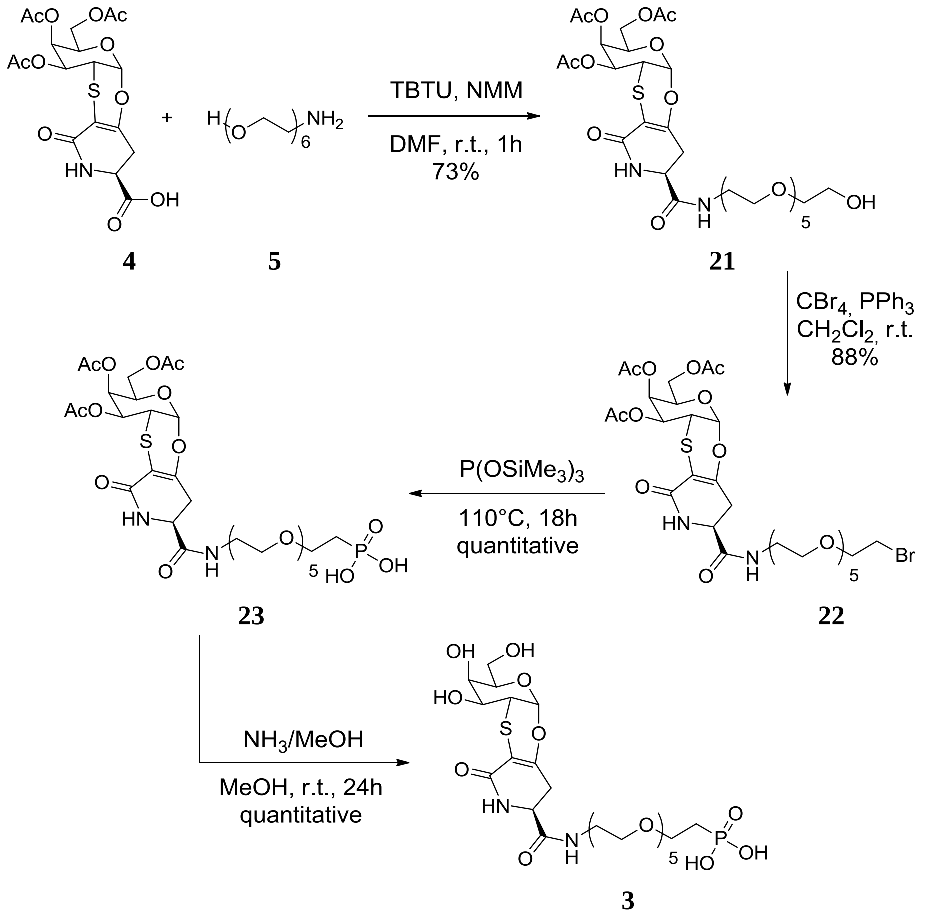

Scheme 3.8 : Synthesis of phosphonate 3.

Compound **4** was reacted with **5** in the presence of *O*-(benzotriazol-1-yl)-*N*,*N*,*N*,*N'*-tetramethyluronium tetrafluoroborate (TBTU) and *N*-methylmorpholine (NMM) to form **21** in 73% yield. By reaction with carbon tetrabromide and triphenylphosphine, the terminal hydroxyl group of **21** was replaced with bromine to give the compound **22** (88%). The presence of the bromine allowed the nucleophilic attack of the phosphite in an Arbuzov reaction for the insertion of the phosphonate functional group [12]. The bromine derivative **22** was thus heated in the presence of tris-trimethyl silyl phosphite ($P(OSiMe_3)_3$) affording **23** in quantitative yield. The deprotection of acetyl group was performed with a solution of ammonia in methanol to give the α-Tn like derivative **3** quantitatively. The so synthesized compound **3** presented all the features necessary for our purposes: the presence of the Tn-like epitope and the polyoxyethylene chain bearing the phosphonate group that will be exploited for the decoration of iron oxide MNPs. All the synthetic procedure and characterizations of the product described above are reported in the experimental section (Chapter 8). The functionalization of MNPs is described in detail in the following paragraph.

3.5 Functionalization of MNPs with the α-Tn antigen mimetic 3

The functionalization of magnetite MNPs, **IAMNP2**, with the α-Tn mimetic **3** was realized by exploiting the high affinity of the phosphonate group at one end of the hexaethylene glycol linker for the iron oxide surface [8]. Thanks to this high affinity a complete replacement of the oleic acid by **3** is expected. Indeed, the carboxylic group of the oleic acid is weakly bound to the inorganic moiety and the formation of covalent linkages with the phosphonate group afford the complete replacement of the former surfactant. The establishment of a stable linkage between the MNPs and the bioactive ligands is fundamental for biomedical application. In fact, the final functionalized MNPs must be stable at physiological conditions and also towards other biological entities as enzymes, that could degrade the molecule.

The replacement of the surfactants with the mimetic **3** was then accomplished by the simple ligand exchange in a chloroform/methanol 10:1 mixture in order to solubilise the two moieties (the mimetic is soluble in methanol but not in chloroform, whereas the MNPs are soluble in chloroform); then, a second exchange process was performed in water in order to increase the functionalization rate exploiting the improved water solubility of the MNPs after the first ligand exchange process. The final product **GMNPs** resulted in a stable black colloidal water solution.

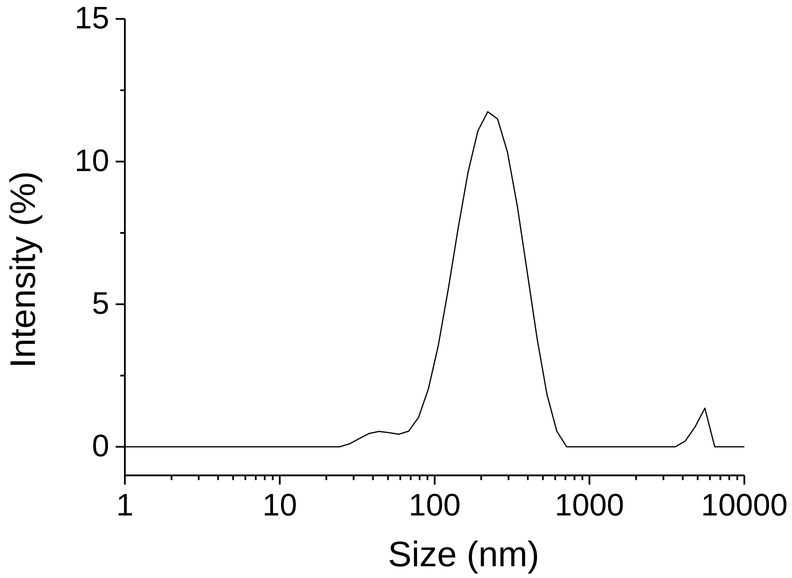

Figure 3.5 : Size distribution by intensity obtained by DLS of GMNPs functionalized with the α-Tn mimetic 3.

DLS measurements (Figure 3.5) revealed the most part of MNPs form aggregates, the average size being 182 nm, the polydispersity index = 0.244 and the Z-potential was -17.4 mV. However, it must be remarked that the measurements were performed after two years. Although after such a long time the most part of NPs form aggregates the final product still appeared as a stable colloidal suspension.

TEM images (Figure 3.6) showed that the inorganic core was unaffected by the functionalization process neither in the dimensions nor in the shape, displaying MNPs with an almost cubic morphology with a mean size of 10.7±1.2 nm (the average size of the oleic acid coated MNPs was 11.3±1.2 nm).

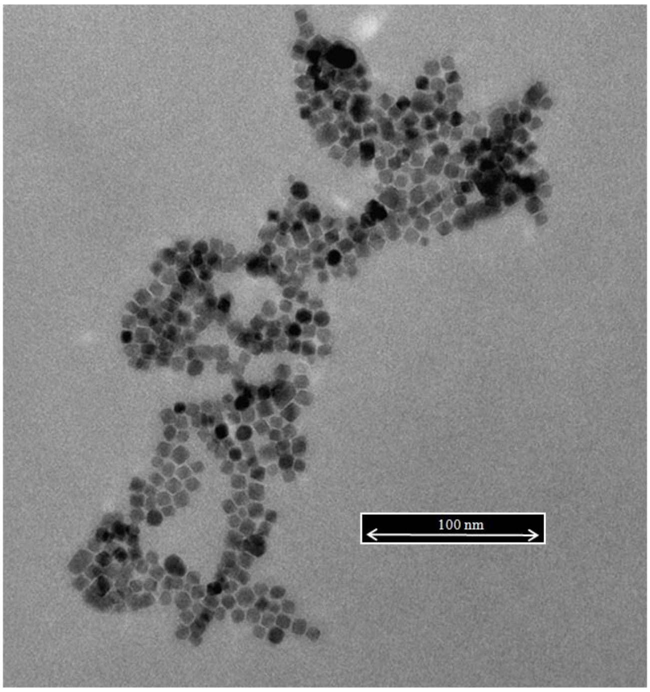

Figure 3.6 : Representative bright field low magnification TEM images of MNPs functionalized with the α-Tn mimetic antigen.

The comparison of the FTIR spectrum of the ligand exchanged product with that of **IAMNP2**, (Figure 3.7), confirmed the substitution of the oleic acid capping agent with the α-Tn mimetic **3**: the two sharp bands at 2922 and 2852 cm^{-1}, observed in the surfactant coated MNPs and attributed to the asymmetric and symmetric CH_2 stretching of the aliphatic chains, respectively, disappeared, while at lower wavenumber (1120 – 950 cm^{-1}) the modes characteristic of the phosphonate group appeared in the spectrum. Of note, the weak band at 990 cm^{-1} which can be attributed to the ν(P-OFe) mode [13] confirmed that the grafting of the mimetic on to the ferrite surface occurred through the phosphonate moiety. The characteristic broad envelop at ca. 580 cm^{-1} related to Fe-O bond vibrations was detected both in the FTIR spectra, indicating the preservation of the iron oxide core after the ligand exchange process.

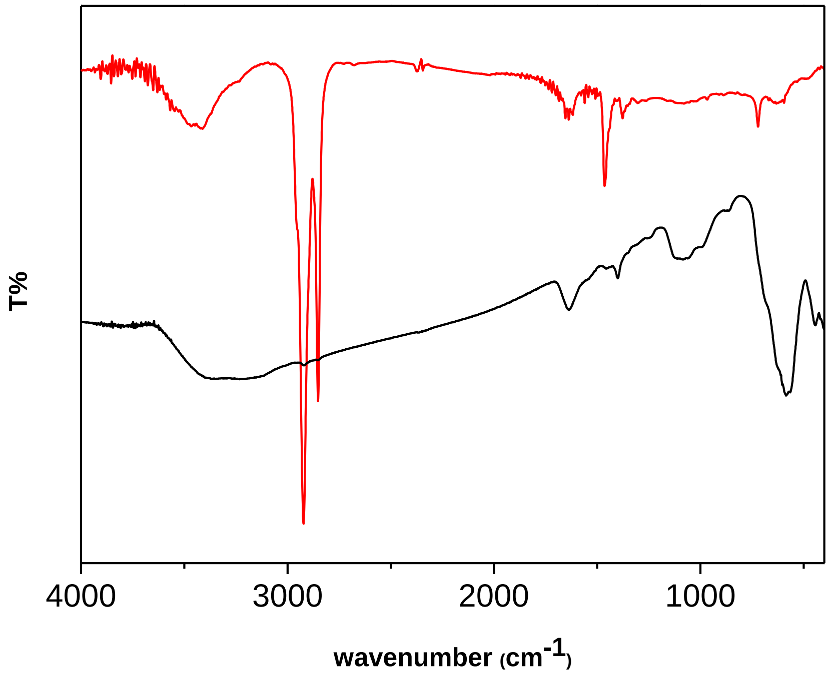

Figure 3.7 : FTIR spectra of the MNPs coated with oleic acid (red line) and after the ligand exchange procedure (black).

The rate of functionalization was estimated on the basis of the phosphorous percentage determined via ICP analysis; it was found equal to $2.01 \cdot 10^{-4}$ mmol/mg of MNPs. Assuming an ensemble of identical MNPs with an average size and morphology, as indicated by TEM images and the density estimated from the XRD pattern, we can assume that on average, each nanoparticle is grafted by 338 α-Tn-like residues, corresponding to a density of 0.84 molecule/nm^2, which is compatible with an almost complete coating of the iron oxide surface.

All together these results confirm the adopted strategy successfully provided a stable suspension of MNPs entirely decorated with the a-Tn antigen mimetic.

References

[1] T. Ju; V. I. Otto; R. D. Cummings, *Angew. Chem. Int. Ed.*, **2011**, *50*, 1770.

[2] S. Ingale; M. A. Wolfert; J. Gaekwad; T. Buskas; G. J. Boons, *Nat. Chem. Biol.* **2007**, *10*, 663.

[3] M. A.Hollingsworth; B. J. Swanson, *Nature Reviews Cancer*, **2004**, *4*, 45.

[4] D. M. Coltart; A. K. Royyuru; L. J. Williams; P. W. Glunz; D. Sames; S. D. Kuduk; J. B. Schwarz; X.-T. Chen; S. J. Danishefsky; D. H. Live, *J. Am. Chem. Soc.* **2002**, *124*, 9833.

[5] (a) F. Venturi; C. Venturi; F. Liguori; M. Cacciarini; M. Montalbano, C.Nativi; *J. Org. Chem.* **2004**, *69*, 6153; (b) G. Capozzi; R. W. Franck; M. Mattioli; S. Menichetti; C. Nativi; G. Valle, *J. Org. Chem.* **1995**, *60*, 6416.

[6] J. Jimenéz-Barbero; E. Dragoni; C. Venturi; F. Nannucci; A. Ardà; M. Fontanella; S. André; F. J. Cañada; H.-J. Gabius; C. Nativi, *Chemistry Eur. J.* **2009**, *15*, 10423.

[7] B. Richichi; B. Thomas; M. Fiore; R. Bosco; H. Qureshi, C. Nativi, O. Renaudet and L. BenMohamed, *Angew. Chem. Int. Ed.*, **2014**, *53*, 11917.

[8] (a) L. Zhou; J. Yuan; Y. Wei, *J. Mater. Chem.*, **2011**, *21*, 2823; (b) T. J. Daou; J. M. Grenèche; G. Pourroy; S. Buathong; A. Derory, C. Ulhaq-Bouillet; B. Donnio; D. Guillon; S. Begin-Colin, *Chem. Mater.*, **2008**, *20*, 5869; (c) Y. Sahoo; H. Pizem, T. Fried; D. Golodnitsky; L. Burstein; C. N. Sukenik; G. Markovich, *Langmuir*, **2001**, *17*, 7907. (d) T. J. Daou; S. Buathong; D. Ung; B. Donnio; G. Pourroy; D. Guillon; S. Bégin, *Sensor Actuator B*, **2007**, *126*, 159.

[9] K. Furusawa, *Chem. Lett.*, **1989,** 509.

[10] (a) J. M. Harris *Poly(ethyleneglycol) chemistry: biotechnical and biomedical applications* Plenum Press, **1992**; (b) J. H. Lee, H.B. Lee, and J. D. Andrade, *Prog. Polym. Sci.* **1995**, *20*, 1043.

[11] F. M. Menger and Hailing Zhang *J. Am. Chem. Soc.*, **2006**, *128*, 1414.

[12] (a) A. K. Bhatacharya, *Chem. Rev.*, **1981**, *81*, 415; (b) L. Lartigue; K. Oumzil; Y. Guari; J. Larionova; C. Guérin; J.-L. Montero; V. Barragan-Montero; C.

Sangregorio; A. Caneschi; C. Innocenti; T. Kalaivani; P. Arosio; A. Lascialfari, *Org. Lett.* **2009**, *11*, 2992.

[13] B. C. Barja; M. I. Tejedor-Tejedor; M. A. Anderson, *Langmuir* **1999**, *15*, 2316.

4. Synthesis of negative control for biological tests on macrophage activation

In Chapter 3 the functionalization of magnetite MNPs with the α-Tn antigen (**GMNPs**) mimetic was described. This nanostructured system was specifically designed to act as immunostimulant, which, as will be described in detail in Chapter 5, was biologically evaluated through *in vitro* tests. In order to clearly assess the properties of the **GMNPs**, three diversely functionalized MNPs, to be used as negative controls, were prepared. These negative controls are essential to quantify the effects induced on cell viability, on cellular uptake and the ability to stimulate immune cell response by **GMNPs**.

The negative controls prepared were the following:

a) MNPs coated with citrate (**CMNPs**): they were synthesized in order to evaluate the biological effect of MNPs decorated with a non-carbohydratic ligand;

b) MNPs coated with methoxy(polyethylenoxy)propyl silane consisting in 9-12 polyethylene units (**PEMNPs**): they were prepared to study the effect of PEG coating on the cellular uptake. As a matter of fact this polymer is known to be "stealth", or rather able to suppress the recognition by the immune system through opsonization [1].

c) MNPs coated with a glucose derivative (**GlcMNPs**): they were employed to compare the biological activity of **GMNPs**, exhibiting the galactosyl epitope of the α-Tn antigen mimetic, with MNPs coated with the glucosyl epitope that should not stimulate any immune response.

In Figure 4.1 an outline of the functionalized MNPs prepared as negative control is reported. In the following paragraphs we report the synthesis of the glucose derivative used for the functionalization of **GlcMNPs** and we discuss the preparation of the three functionalized MNPs samples.

a) Citrate coated MNPs (CMNPs)

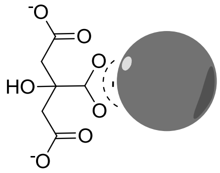

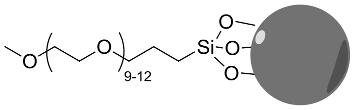

b) PEG coated MNPs (PEMNPs)

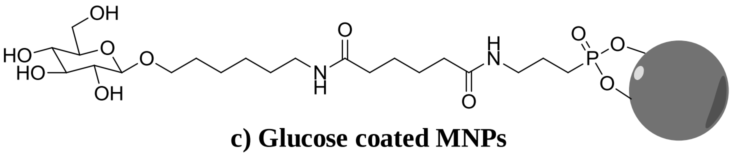

c) Glucose coated MNPs (GlcMNPs)

Figure 4.1 : Functionalized MNPs prepared as negative controls for biological tests.

4.1 Synthesis of the glucose derivative for MNPs functionalization

The coating of MNPs with the glucosyl epitope was accomplished by coupling the glucose derivative **24** bearing the terminal carboxylic group activated as p-nitrophenyl ester with the free amino group presents on the MNPs functionalized with 3-aminopropyl phosphonic acid (APPA), as outlined in Figure 4.2. Details on the synthesis are provided in Chapter 8.

a) Glucose derivative 24

b) MNPs functionalized with APPA

Figure 4.2 : Structures of a) the glucose derivative used for the coupling reaction with b) MNPs functionalized with 3-aminopropylphosphonic acid (APPA).

Hereafter we describe the synthesis of the glucose derivative **24** including the synthesis of products **25** and **26** that will be respectively called "N_3-linker" and "activated linker", whereas the MNPs functionalization step will be described in paragraph 4.2.

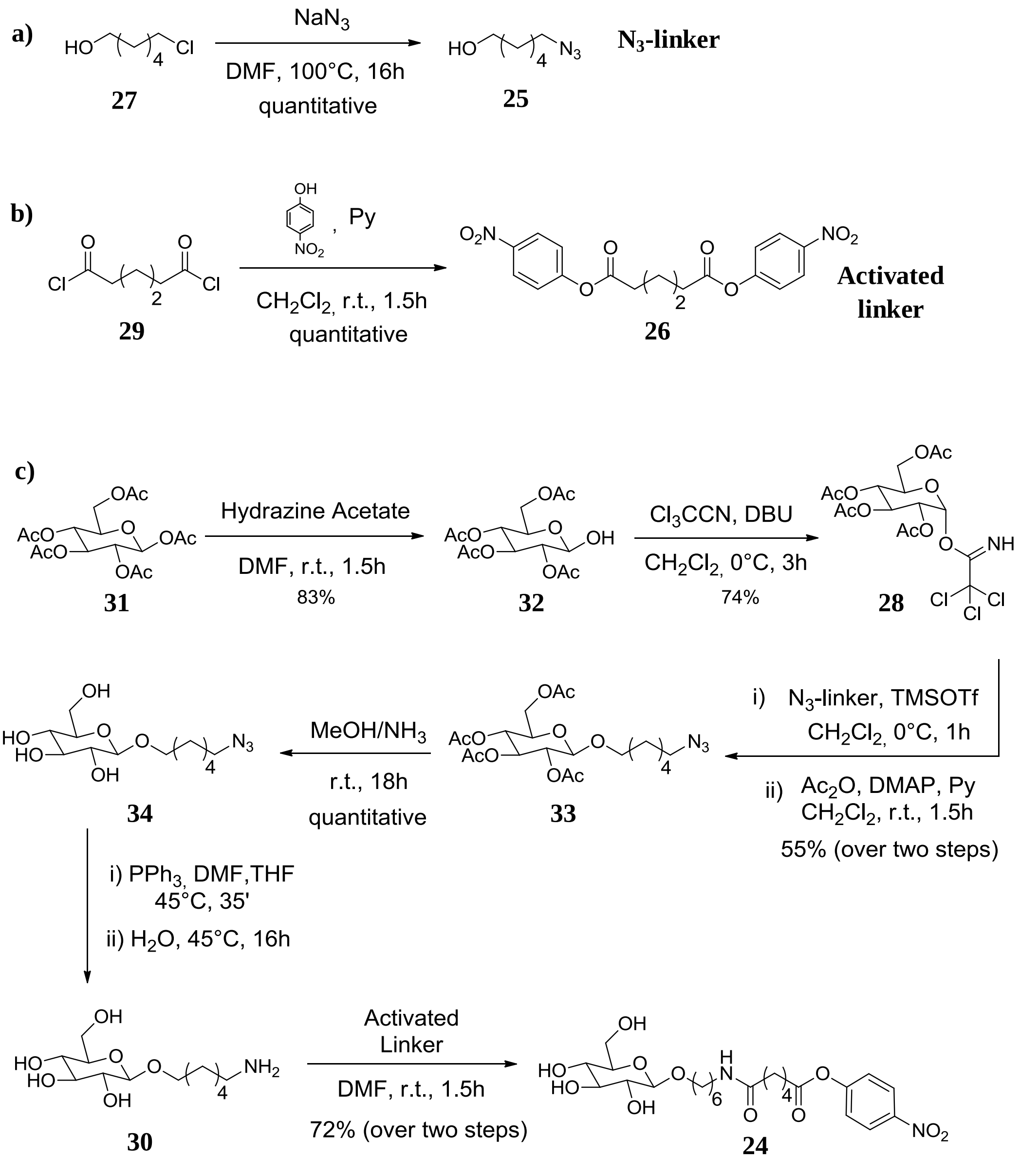

Scheme 4.1 : Synthesis of a) N_3-linker b) activated linker and c) glucose derivative.

The N_3-linker [2] was synthesized in quantitative yield by the reaction of 6-chloro-1-hexanol, **27,** with sodium azide and it was subsequently used in the glycosylation of **28** (Scheme 4.1a).The esterification of adipoyl chloride **29** with p-nitrophenol afforded the activated linker **26** [3] in quantitative yield (Scheme 4.1b) and it will be used in the coupling reaction with **30**.

Concerning the preparation of the carbohydrate moiety the synthesis started from the selective deacetylation of the hydroxyl group in position one of β-D-glucose pentaacetate **31** with hydrazine acetate affording the product **32** in 83% yield (Scheme 4.2).

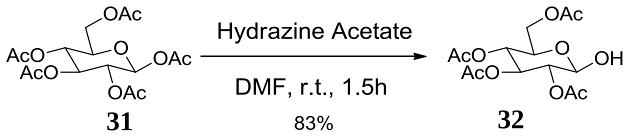

Scheme 4.2 : Selective deacetylation of glucose pentaacetate.

The glycosyl donor **28** was synthesized by a simple base-catalyzed addition of the anomeric hydroxyl group of **32** to trichloroacetonitrile giving the α-glucosyl trichloroacetimidate selectively and in 74%yield (Scheme 4.3).

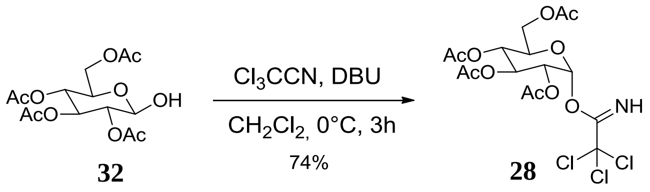

Scheme 4.3 : Synthesis of the α-glucosyl trichloroacetimidate 28.

Then the glycosylation was accomplished by reacting the glucosyl trichloroacetimidate **28** [4] with the N_3-linker **25** in the presence of a catalytic amount of trimethylsilyl trifluoromethanesulfonate (TMSOTf) as Lewis acid. An NMR analysis of the crude product deriving from the glycosylation reaction showed the presence of partially deacetylated side products, hence a following acetylation with acetic anhydride catalyzed by dimethylaminopyridine (DMAP) was performed (Scheme 4.4).

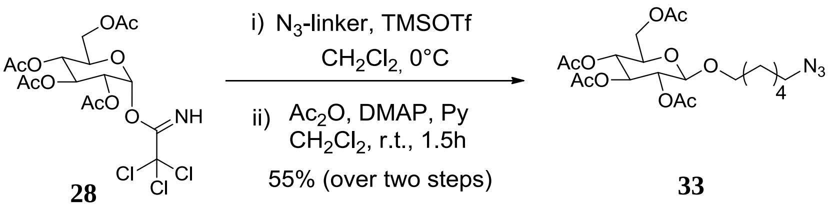

Scheme 4.4 : Glycosylation of the glucosyl trichloroacetimidate with the N_3-linker.

The β-glucosyl derivative **33** was obtained in 55% yield, calculated over two steps; treatment of **33** with a solution of ammonia in methanol gave a complete deacetylation to form **34** in quantitative yield (Scheme 4.5).

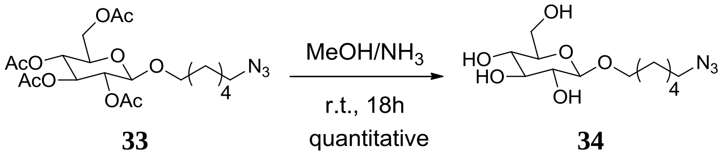

Scheme 4.5 : Deacetylation of the β-glucosyl derivative.

The azide group of **34** was reduced to amine under Staudinger conditions affording **30** (Scheme 4.6) which, in turn, was coupled with the activated linker **26** by the formation of an amidic bond.

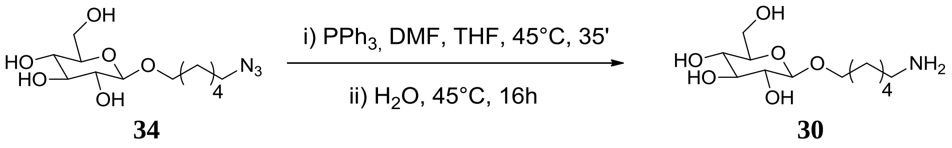

Scheme 4.6 : Azide reduction under Staudinger conditions.

Finally, the glucose derivative **24** with the terminal carboxylic group activated as p-nitrophenyl ester was obtain in 72% yield over two steps (Scheme 4.7).

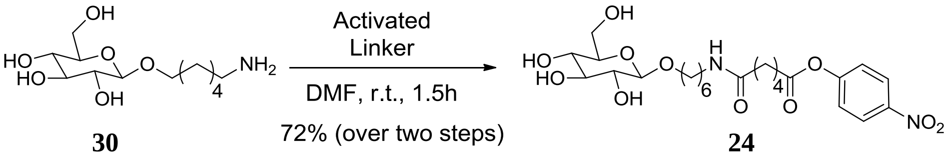

30

24

Scheme 4.7 : Coupling reaction between the glucosyl moiety and the activated linker.

Compound **24** was then used for the functionalization of MNPs exploiting the reactivity of activated ester towards the free amino groups present on the MNPs capped with APPA as described in the following paragraph.

4.2 Functionalization of MNPs with citrate, glucose and PEG

In this paragraph the procedures for the preparation of the previously mentioned three MNPs samples employed as negative controls for biological tests are discussed in detail.

CMNPs were synthesized starting from the same MNPs, **IAMNP2**, used for the functionalization with the α-Tn mimetic by replacing the oleic acid with the citrate ligand. The reaction was carried out by reacting MNPs and monohydrated citric acid in a 1:1 mixture of 1,2-dichlorobenzene-DMF at 100°C for 24h [5]. The resulting **CMNPs** were soluble in water and no remarkable differences in terms of size, size distribution and shape were found, as demonstrated by TEM images; indeed, the average size was 11.3±1.2 nm for oleic acid coated **IAMNP2** and 10.9±1.8 nm for citrate coated MNPs (Figure 4.3).

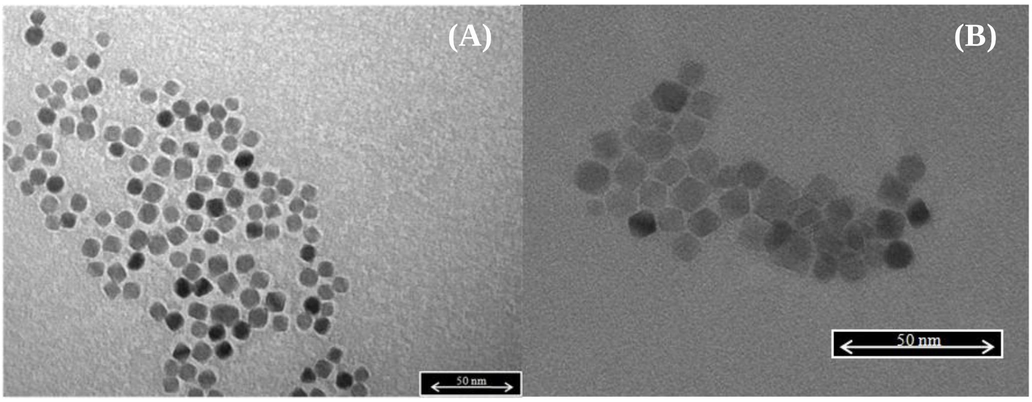

Figure 4.3 : TEM images of (A) IAMNP2, MNPs coated with oleic acid and (B) CMNPs coated with citrate ligand. Size and shape were retained after the ligand exchange process.

In Figure 4.4 the FT-IR spectrum is reported. The intense band at 3300 cm^{-1} was compatible with the presence of non dissociated OH groups of citric acid. The peak at 1630 cm^{-1} could be attributed to the symmetric stretching of carboxylic OH group; the peak at 1400 cm^{-1} was attributed to the asymmetric stretching of the carboxylic CO. Free citric acid has a peak at 1755 cm^{-1} belonging to the carboxylic CO vibration and the peak shift observed in this case confirmed the binding of citrate to the surface of MNPs.

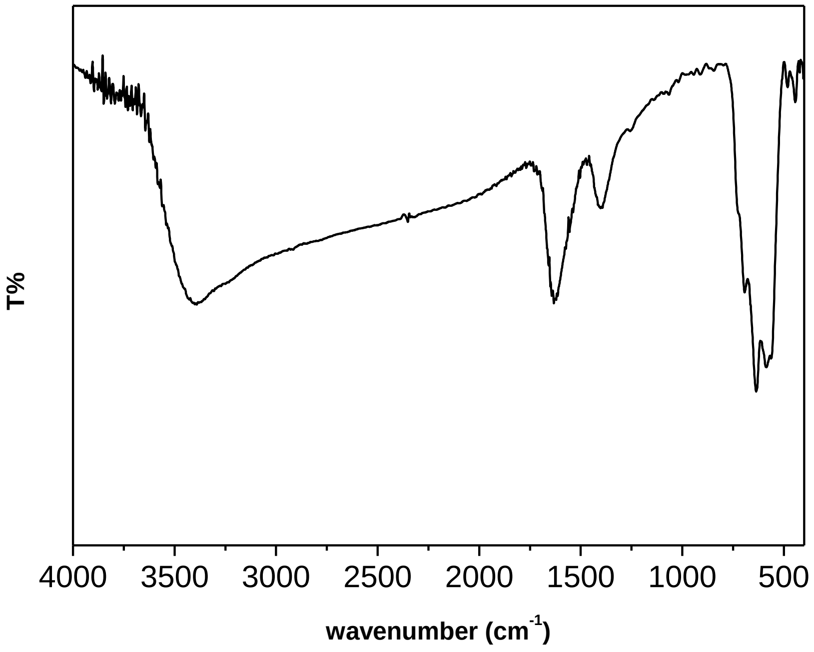

Figure 4.4 : FT-IR spectrum of citrate coated MNPs (CMNPs).

PEMNPs were prepared by a ligand exchange process starting from oleic acid coated MNPs, **IAMNP8**, synthesized starting from iron(III) acetylacetonate [6]. The reaction was accomplished by mixing the nanoparticles with methoxy(polyethylenoxy)propyltrimethoxysilane in a 10:1 hexane-chloroform mixture in the presence of a catalytic amount of acetic acid. After the ligand exchange the MNPs are no longer soluble in hexane but are soluble in ethanol and water confirming a modification of the MNP surface occurred. Also in this case no significant difference in size and shape was observed from TEM micrographs (Figure 4.6). The average size evaluated from a statistical analysis over several micrographs was 12.5±1.6 nm and 12.4±1.8 nm for pristine and PEG coated **PEMNPS**, respectively.

The successful functionalization with the PEG-silane ligand was confirmed by the FT-IR spectrum of **PEMNPs** shown in Figure 4.5, where the appearance of several peaks in the range of 1430-950 cm^{-1} in which all the CH_2-O-CH_2 vibrations related to the PEG chain occurs. The small band at 1020 cm^{-1} was attributed to the Si-O-R stretching whereas the Si-C stretching wad characterized by a peak at 1250 cm^{-1}.

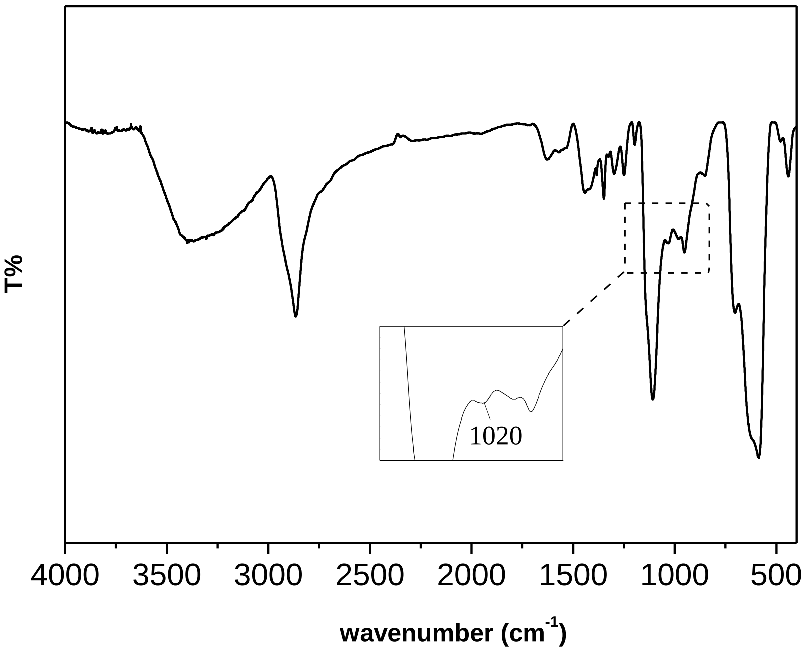

Figure 4.5 : FT-IR spectrum of PEG coated MNPs (PEMNPs)

Finally **GlcMNPs** were prepared starting from the same MNPs batch, **IAMNP8**, Before the functionalization with the glucose residue the oleic acid was replaced with 3-aminopropylphosphonic acid by reacting it with tetramethylammonium 3-aminophosphonate salt in a hexane/dichloromethane/water emulsion mixed by sonication. The bifunctional molecule aminophosphonate was able to anchor the iron oxide surface thanks to the phosphonic group while the amino group was exploited for the following coupling with the activated carboxylic group of the glucose derivative. The functionalization using the tetramethylammonium salt of the phosphonic acid instead of APPA itself proved to be more efficient in terms of solubility and stability of the final MNPs dispersion.

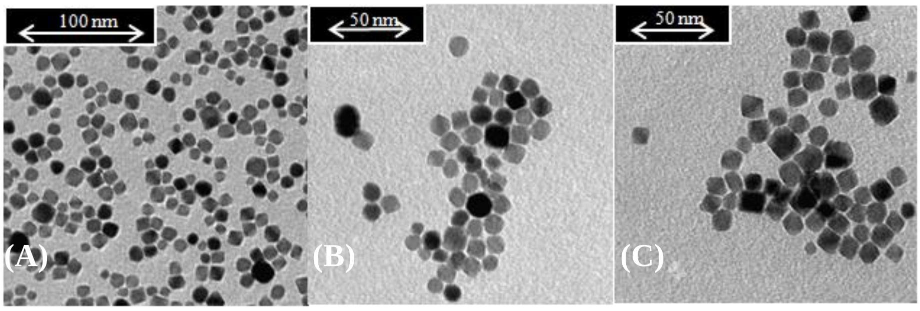

Figure 4.6 : TEM image of (a) IAMNP8 coated with oleic acid d = 12.5±1.6 nm (b) PEMNPs coated with PEG ligand, d = 12.4±1.8 nm and (c) GlcMNPs functionalized with the modified glucose residue, d = 12.9±1.5 nm.

The coupling reaction was carried out by simply mixing the as prepared APPA functionalized MNPs with the glucose derivative **24** in DMF thanks to the formation of the amide bond between the activated carboxylic group of the carbohydrate moiety and the free amino groups present on the surface of the nanoparticles. Of note, the same activated glucose derivative **24** was already exploited with good results in coupling reactions with free amino groups present on ovalbumin with good efficiency (unpublished results).

The so synthesized **GlcMNPs** were purified by magnetic decantation and then dispersed in water. The change in the solubility properties of the MNPs after the reaction and the pale yellow coloration of the supernatant due to the hydrolysis of the p-nitrophenyl ester were indicative that the coupling occurred.

Unfortunately, the IR spectra of **GlcMNPs** (Figure 4.7) are not very informative. Indeed, the most relevant IR peaks of the glucose derivative overlap to those belonging to APPA (figure 4.8), which, considering the small number of glucose unit loaded, makes extremely difficult to detect the carbohydrate moiety. However, the modification of the spectrum occurring in the frequency range characteristic for O-H stretching (3500-3200 cm^{-1}) together with the variation observed in the solubility properties support the formation of the glucose functionalized magnetic nanoparticles.

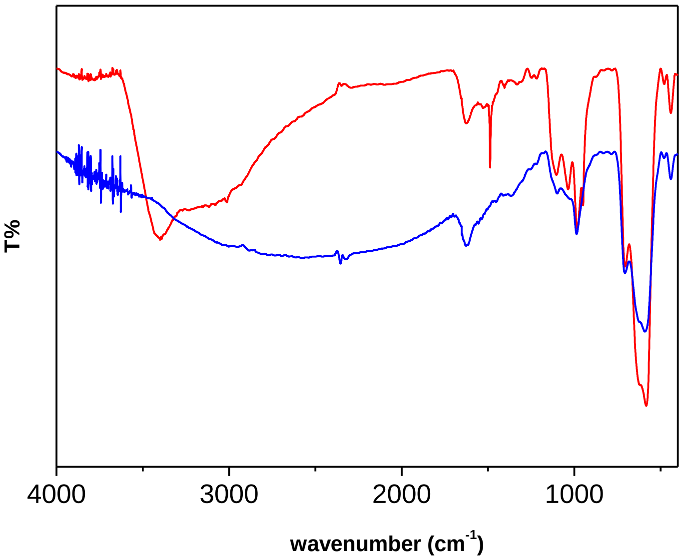

Figure 4.7 : IR spectra of MNPs coated with aminophosphonic acid (APPA) in red and GlcMNPs functionalized with the glucose derivative in blue.

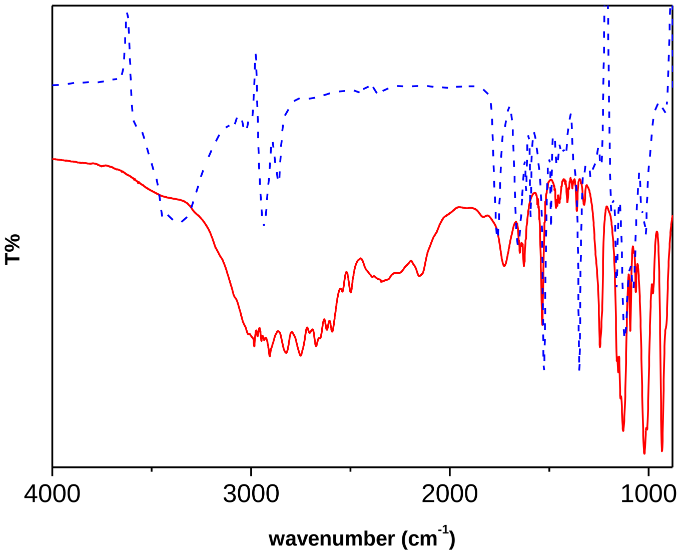

Figure 4.8 : IR spectra in KBr pellet of 3-aminopropylphosphonic acid (red) and glucose derivative 24 (blue dashed).

Concerning the stability of the **GlcMNPs** water dispersion, the DLS analysis, shown in Figure 4.9 gave an average size of 117 nm with a polydispersity index of 0.230, suggesting that the particles formed some aggregates comprising a low number magnetic center. Accordingly, a slow sedimentation of the nanoparticles was observed over long time. However, the presence of this aggregates is not expected to affect in any way the biological test.

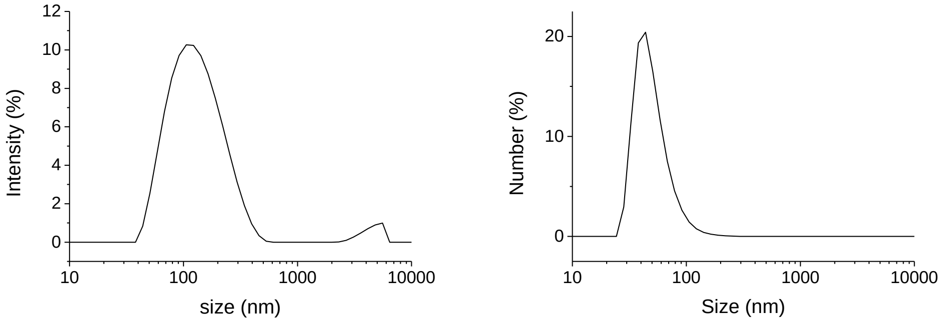

Figure 4.9 : DLS analysis of samples GlcMNPs a) size distribution by intensity and b) size distribution by number.

The small peak observed in the micron range was due to some dust occurring in the sample which was present in a very small percentage and well demonstrated by reporting the weight of each population by number of objects.

In conclusion, the ligand exchange with APPA for the subsequent coupling with the glucose derivative was successful. However, we still need to improve the water solubility and the stability of the aqueous dispersion of the MNPs. To this aim, we explored different functionalization methods changing the linker used in the ligand exchange reaction, as it will be described in detail in Chapter 6.

References

[1] K. Knop; R. Hoogenboom; D. Fischer and U. S. Schubert, *Angew. Chem. Int. Ed.*, **2010**, *49*, 6288.

[2] A. Arcangeli; L. Toma; L. Contiero; O. Crociani; L. Legnani; C. Lunghi; E. Nesti; G. Moneti; B. Richichi; C. Nativi, *Bioconjugate Chem.*, **2010**, *21*, 1432.

[3] X. Wu; C.-C. Ling; D. Bundle, *Org. Lett.*, **2004**, *6*, 4407.

[4] R. R. Schmidt and K.-H. Jung, in *Preparative Carbohydrate Chemistry* Ed. S.Hanessian Marcel Dekker, New York, **1997**, p.283.

[5] M. Lattuada and T. A. Hatton, *Langmuir*, **2007**, *23*, 2158.

[6] R. De Palma; S. Peeters; M. J. Van Bael; H. Van den Rul; K. Bonroy; W. Laureyn; J. Mullens; G. Borghs and G. Maes, *Chem. Mater.*, **2007,** *19*, 1821.

5. Macrophages activation

In Chapter 4 we described the synthesis and the characterization of the MNPs functionalized with the α-Tn antigen mimetic (**GMNPs**) and the MNPs prepared as negative controls for biological tests in order to better evaluate the effect of **GMNP**s on immune cells: **GlcMNPs** (coated with glucose), **CMNPs** (coated with citric acid) and **PEMNPs** (coated with polyethylene glycol, 9-12 PE units). Since macrophages were chosen for the immunoactivity evaluation of our samples, in paragraph 5.1 a brief description of the role played by macrophages in the immune response is given. In paragraph 5.2 the biological tests, performed on MNPs samples mentioned above, are described in detail.

5.1 Macrophage role in the immune response

Macrophages [1] play a critical role in the innate immunity since they provide an immediate response against foreign substances representing our first line of defence against pathogen agents. They are able to engulf what is recognized as non-self in a process called phagocytosis (Figure 5.1).

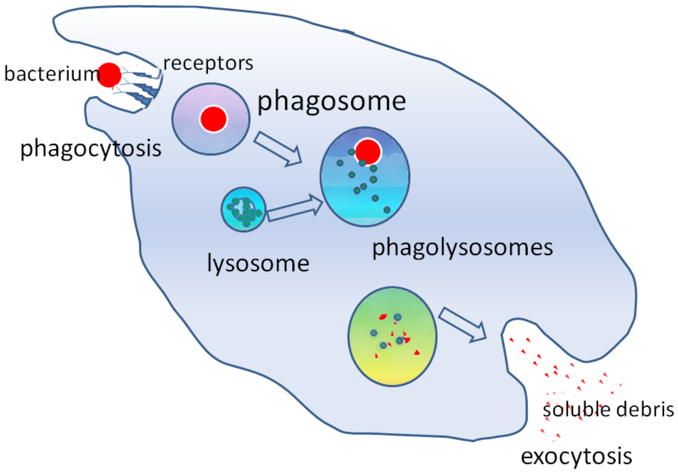

Figure 5.1 : Phagocytosis process and phagolysosomes formation.

When a macrophage ingests a pathogen, the pathogen becomes trapped in an intracellular vesicle called phagosome, which then fuses with a lysosome to form a phagolysosomes. This process activates various enzymes contained in the phagolysosomes, able to produce reactive oxygen species (ROS) and nitric oxide (NO) which have a toxic effect towards pathogen agents. Another class of enzymes activated in this process is represented by the lysosomal proteases responsible of the degradation of microbial proteins.

Besides the ability to engulf and kill microbes, macrophages also help to initiate specific defence mechanisms (adaptive immunity) by recruiting and activating other immune cells such as lymphocytes through the production of cytokines.

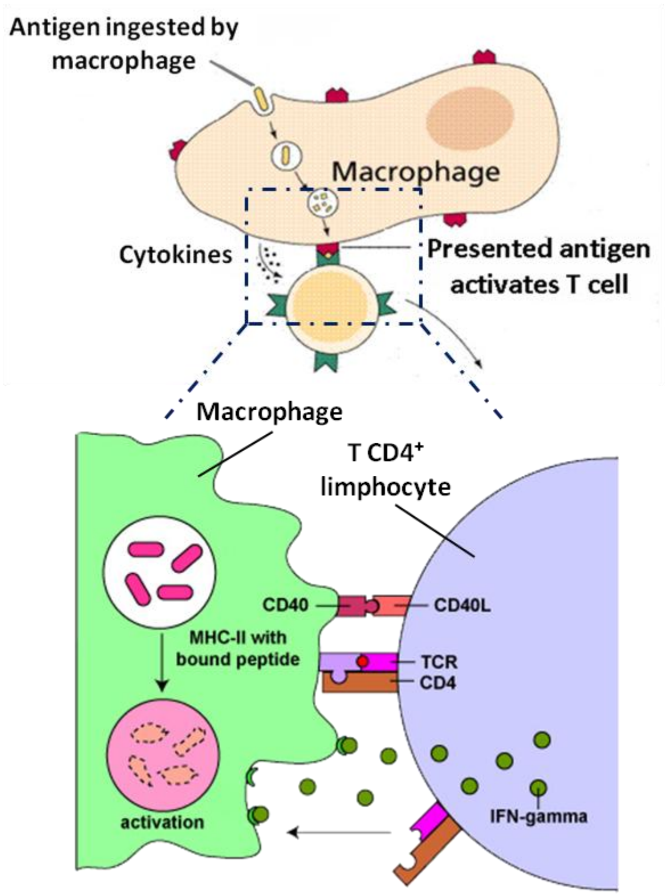

Figure 5.2 : Interaction between a macrophage and a T lymphocyte. After the phagocytosis process the macrophage produces cytokines that activate lymphocytes T CD4$^+$. Lymphocytes T CD4$^+$ interacts with the macrophage MHC II receptor presenting the antigen and in turn produces IFN-γ that improve the macrophage microbial activity.

Moreover, after digestion of a pathogen, a macrophage will present the antigen in association with MHC II receptors to T lymphocytes.

It is worth to note that the antigen is often represented by a fragment of a microbic protein and it is used by the immune system for identification. Once a T cell has recognized its particular antigen on the surface of the macrophage, the T cell becomes an activated effector cell and in turn secretes INF-γ (interferon-γ) that improves the macrophage microbicidal activity (Figure 5.2). This cross-interaction between macrophages and T lymphocytes is an excellent example of the cooperation between the innate immunity and the adaptive immunity, highlighting the crucial importance of macrophages activation in the amplification of the immune response.

5.2 Biological tests

In the previous paragraph we described the importance of macrophages in the immune response, and in this section the biological tests performed are described in detail. In particular, our samples were biologically assessed for purity evaluating the absence of endotoxin contamination; for biocompatibility, analyzing the effects induced on cell viability after 24-72h incubation; for the cellular uptake; for immunoactivity, evaluating the ability to stimulate immune cell responses.

Before biologically testing, each compound was carefully evaluated for purity to rule out the possibility that immune cell responses were due to the presence of endotoxin contaminations, such as lypopolysaccharide (LPS), introduced into the system through chemicals, materials or equipments. Limulus amebocyte lysate (LAL) endochrome assays were, thus, performed in four different batches of each compound and the concentration of LPS measured. LPS concentrations were always below the value of 0.01 ng/ml, which is sufficient to stimulate immune cell responses [2], suggesting that all compounds under testing were LPS-free and biologically evaluable (data not shown).

We, then, studied the effects of **MNPs** on immune cells. For this purpose we decided to use macrophages, since they are potent immune cells providing immediate responses against dangerous molecules and acting as APCs (Antigen Presenting Cells) to stimulate adaptive immune response. Exposure to non-self antigens, indeed, can induce a rapid activation of macrophages, which stops proliferation and acquires effector cell functions [3]. In the present study a mouse monocyte/macrophage quiescent cell line (RAW 264.7) was used, since these cells are a widely recognized model of human macrophages [4] with a good experimental reproducibility.

We analyzed the effects of **GMNPs** and **GlcMNPs** on RAW 264.7 cell viability in comparison to un-functionalized MNPs, **CMNPs,** and **PEMNPs,** (controls) and the monovalent α-Tn mimetic **3**. We used three validated *in vitro* assays (Trypan blue, calcein-AM, MTT) for toxicity measurements, because it has been demonstrated that MNPs can interfere in several of these well-established methods, leading to false-negative results [5]. Cells were exposed to different concentrations (0.01-30 μg/ml) of each compound for 24-72 h; thereafter, cell viability was measured. No toxicity was determined in any of the three considered assays at all the tested concentrations (Figures 5.3), suggesting that all the compounds under evaluation are biocompatible.

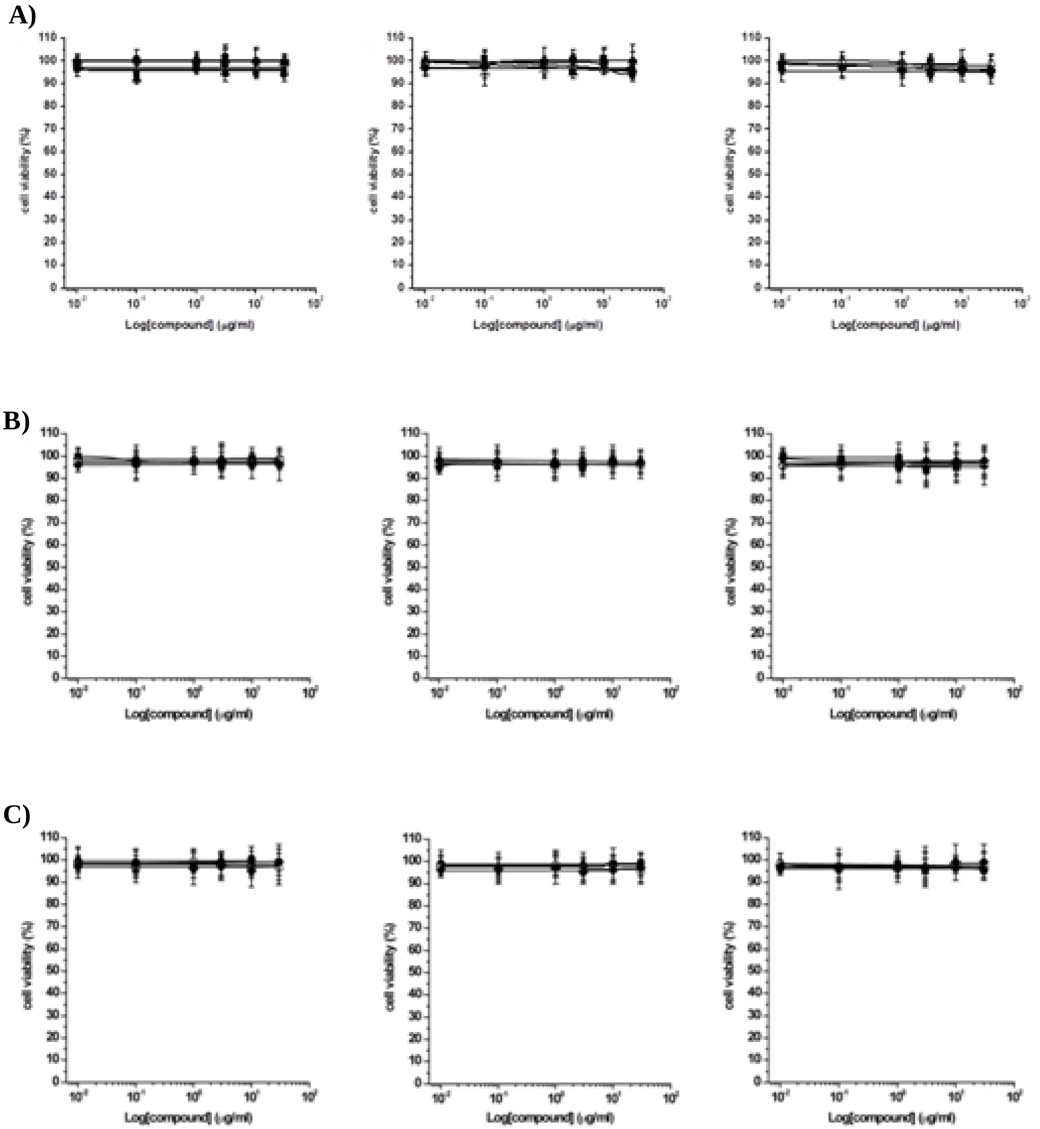

Figure 5.3 : Effects of compound 3, polyethylene glycol-coated MNPs (PEMNPs), citrate-coated MNPs (CMNPs), and glycosyl MNPs (GMNPs and GlcMNPs) on cell viability as a function of the concentration. RAW 264.7 cells were treated with increasing concentrations (0.01-30 µg/ml) of 3 (closed squares), PEMNPs (open triangles), CMNPs (closed circles), GMNPs (closed triangles) or GlcMNPs (closed diamonds) for 24h (left panels), 48h (middle panels) and 72h (right panels). A) Cell viability assessed by MTT. B) Calcein-AM assay C) Trypan Blue exclusion assay. The concentration-response curves show the percentage of cell viability in comparison to controls (compound-untreated cells). The data represent mean ± SEM of at least three independent experiments run in triplicate.

The next step was to qualitatively investigate by Prussian blue staining the cellular uptake of **CMNPs**, **PEMNPs**, **GlcMNPs** and **GMNPs**. The typical Prussian blue staining images of cells treated with **CMNPs** (A), **GMNPs** (B) or **GlcMNPs** (C) showed an intracellular localization of these MNPs, demonstrating that both glycosylated (B and C) and not-glycosylated (A) MNPs, can enter into macrophages (Figure 5.4**). PEMNPs** were not endocyted, while the endocytosis of the α-Tn antigen mimetic **3**, not conjugated to MNPs, cannot be visualized by this method.

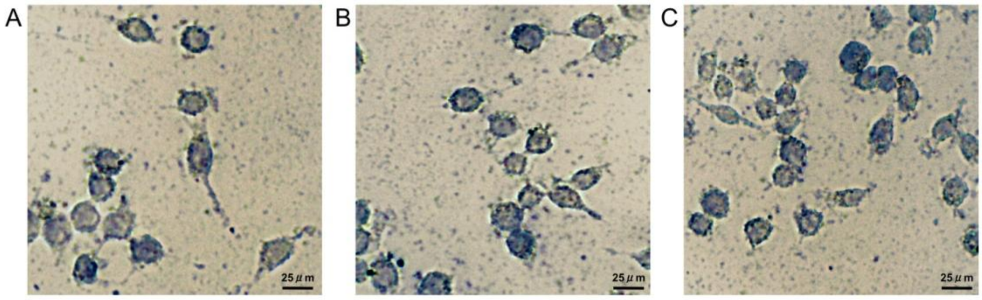

Figure 5.4 : Intracellular MNPs localization. Bright-field images of RAW 264.7 cells treated with 30 µg/ml of CMNPs (A), GMNPs (B), or GlcMNPs (C) for 24h. MNPs were labelled with Prussian blue iron staining and visualized with an optical microscope (objective 40X) equipped with an integrated camera. Images are from a representative experiment carried out three times with similar results (scale bar = 25 µm).

The endocytosis of **3**, **CMNPs**, **PEMNPs**, **GMNPs** and **GlcNMPs** were then quantitatively determined by flow cytometry (FACS). We used side-scattered light (SSC) as an indicator of particle uptake: when particles are endocyted by cells, SSC intensity increases because the cell granularity is enhanced. Figure 5.5 shows that the SSC intensity increased after cell treatment with MNPs, either functionalized or not, suggesting a similar level of cellular uptake occurs independently of the type of carbohydrate attached to the MNP surfaces. In contrast, when the cells were exposed to **PEMNPs** or α-Tn mimetic antigen **3**, not conjugated to MNPs, the SSC intensity did not change, demonstrating that they were not endocyted by macrophages (Figure 5.5).

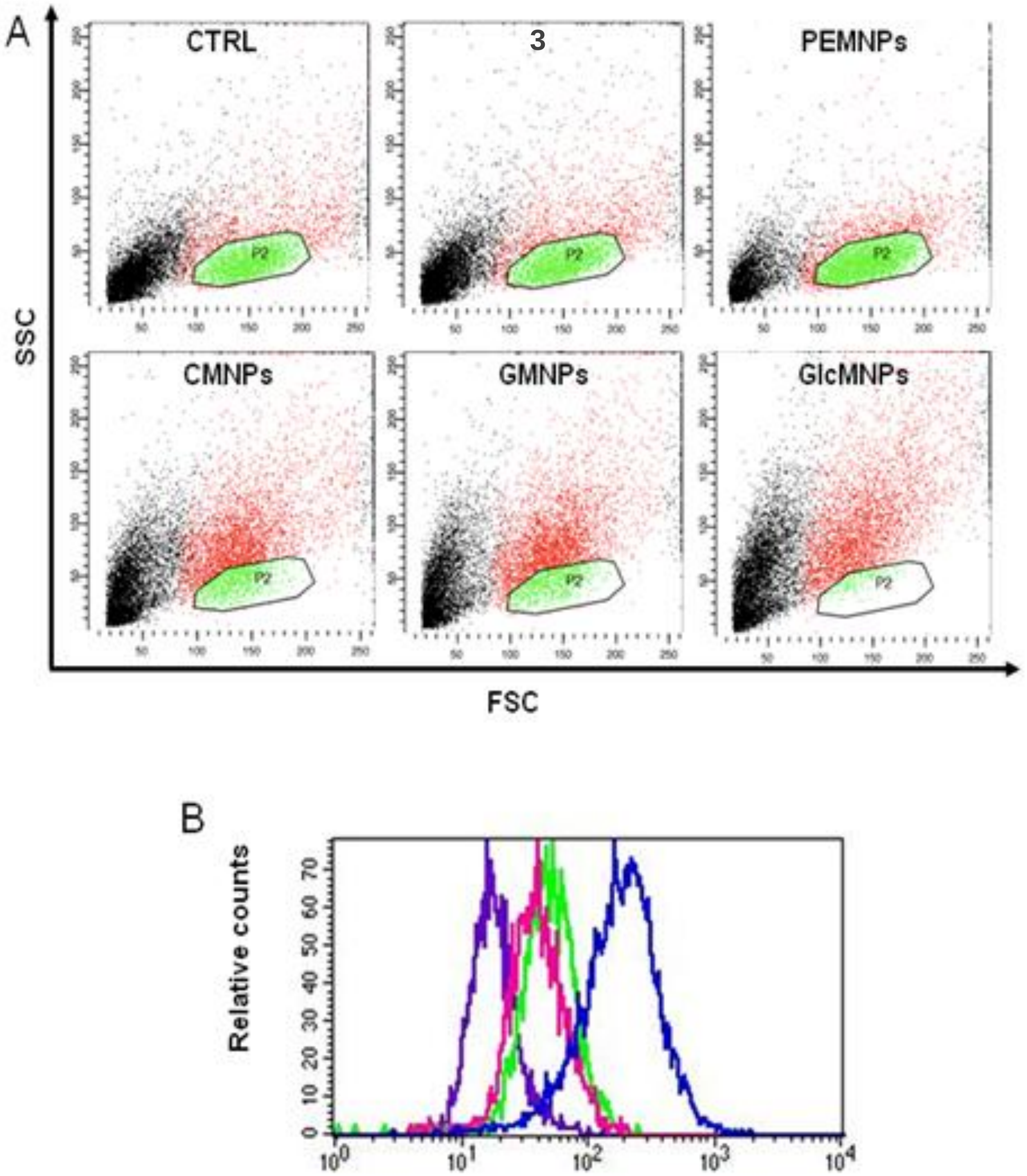

Figure 5.5 : Quantitative evaluation of the 3, PEMNPs, CMNPs, GMNPs, and GlcMNPs uptake. RAW 264.7 cells were treated with 30 µg/ml of 3, CMNPs, PEMNPs, GMNPs, or GlcMNPs for 24h. The compound uptake was determined by measuring the cell granularity by FACS. (A) Representative dot plots showing the effects of compound uptake on granularity (SSC) and size (FSC) of RAW 264.7 cells. Images are from a representative experiment carried out three times with similar results. (B) Overlay plot of the RAW 264.7 cell SSC measured after CMNPs (green), GMNPs (pink), or GlcMNPs (blue) uptake. Untreated cells are shade in violet.

By taking into consideration data reported in the literature [6], our results can be explained by the peculiar surface properties of the MNPs and, in particular, the impact of their charge surface properties on effective phagocytosis. In this sense, the citrate-coated MNPs (**CMNPs**) being negatively charged resulted well internalized by macrophages, while the un-charged polyethylene glycol-coated MNPs (**PEMNPs**) were prevented from cellular uptake. Of note, a multivalent display of the α-Tn mimetic antigen seems to be necessary for macrophage uptake.

Figure 5.6 and 5.7 show the effects of both the concentration and the time of cell exposure to each compound on the levels of MNPs uptake, demonstrating that the type of coating sensibly influences the kinetic of cellular MNPs uptake.

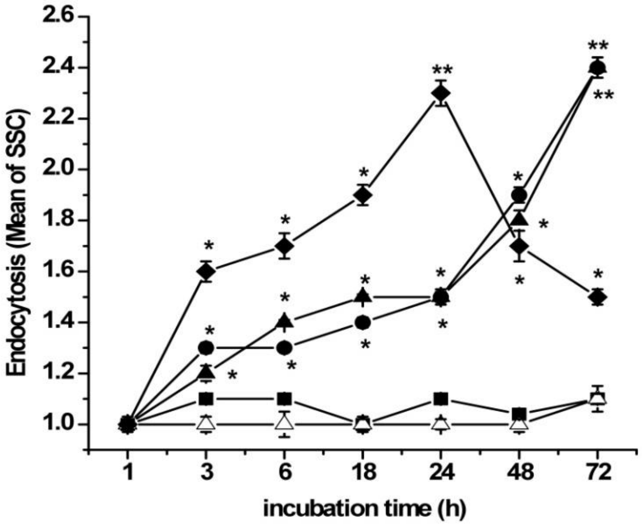

Figure 5.6 : Time-course of 3, PEMNPs, CMNPs, GMNPs and GlcMNPs uptake. RAW 264.7 cells were treated with 30 µg/ml of 3 (closed squares), PEMNPs (open triangles), CMNPs (closed circles), GMNPs (closed triangles) or GlcMNPs (closed diamonds) for up to 72 h. At indicated incubation time points, cells were harvested and analyzed. The compound uptake was quantified by FACS. The data represent mean ± SEM of at least three independent experiments. *p≤ 0.05; **p≤0.01 vs. controls (compound-untreated cells).

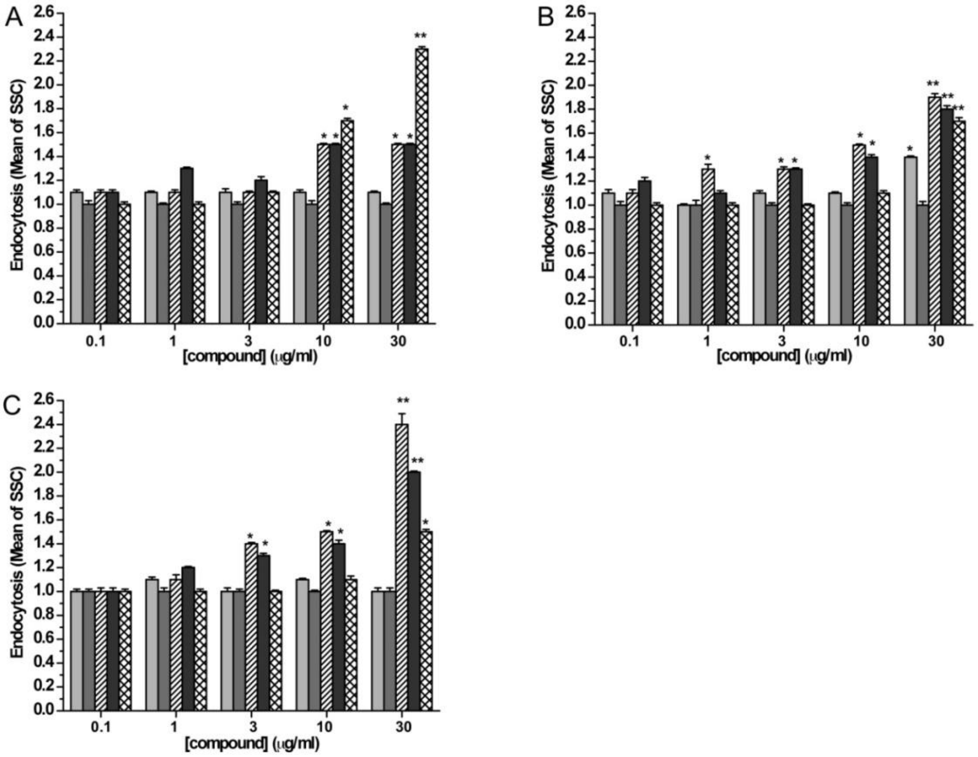

Figure 5.7 : Concentration-dependence of 3, polyethylene glycol-coated MNPs (PEMNPs), citrate-coated MNPs (CMNPs), and glycosyl MNPs (2MNPs and GlcMNPs) uptake. RAW 264.7 cells were treated with increasing concentrations (0.1-30 μg/ml) of 3 (light grey bars), PEMNPs (grey bars), CMNPs (hatched bars), GMNPs (dark grey bars) or GlcMNPs (cross-hatched bars), for 24h (A), 48h (B) and 72 h (C). In each sample, the compound uptake was quantified by FACS. The data represent mean ± SEM of at least three independent experiments. *$p \leq 0.05$; **$p \leq 0.01$ vs. controls (untreated cells).

Finally, we investigated whether MNPs trigger effector functions in the same cells. Figures 5.8 and 5.9 show the effect induced by each compound on the production of a typical pro-inflammatory mediator (TNF-α). Remarkably, only the MNPs functionalized with the α-Tn mimetic antigen (**GMNPs**) are able to induce TNF- α gene expression and protein release at levels similar to those obtained with LPS (0.1 μg/ml), while only a 50% of the TNF-α increase was induced by **GlcMNPs** in comparison to **GMNPs**.

The type of the monosaccharide used in the coating influenced not only the levels, but also the time-course of cytokine production: **GMNPs** determined, indeed, a significant time-dependent increase of TNF-α release, while **GlcMNPs** raised a same level of TNF-α releasing, independently of the time considered.

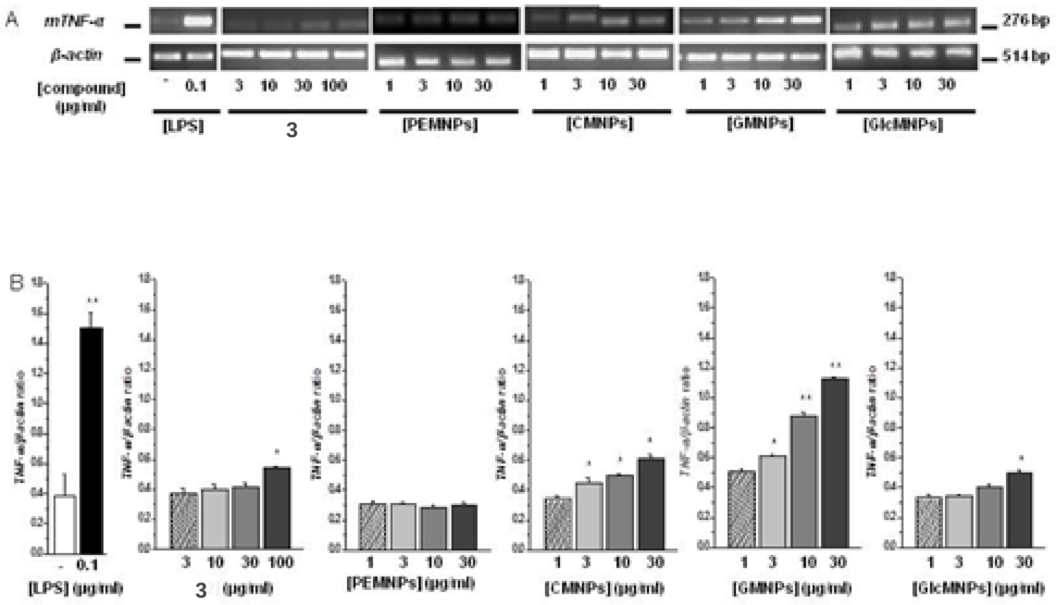

Figure 5.8 : Effects of 3, PEMNPs, CMNPs, GMNPs and GlcMNPs on TNF-α gene expression. RAW 264.7 cells were treated (24h) with increasing concentrations (1-30 µg/ml) of 3, PEMNPs, CMNPs, GMNPs or GlcMNPs. Expression of β-actin was used as a loading control. Compound untreated cells (CTRL) were considered as negative, while 0.1 µg/ml LPS-treated cells as positive controls. (A) Representative results of RT-PCR for the TNF-α and β-actin gene expression. (B) The signals were densitometrically analyzed and data, calculated as mean ± SEM of at least three independent determinations, are expressed as ratio (TNF-α/β-actin) of the signals obtained for each sample divided by that obtained for β-actin in the same sample to permit between-sample comparisons. *$p \leq 0.05$; **$p \leq 0.01$ vs. controls (compound-untreated cells).

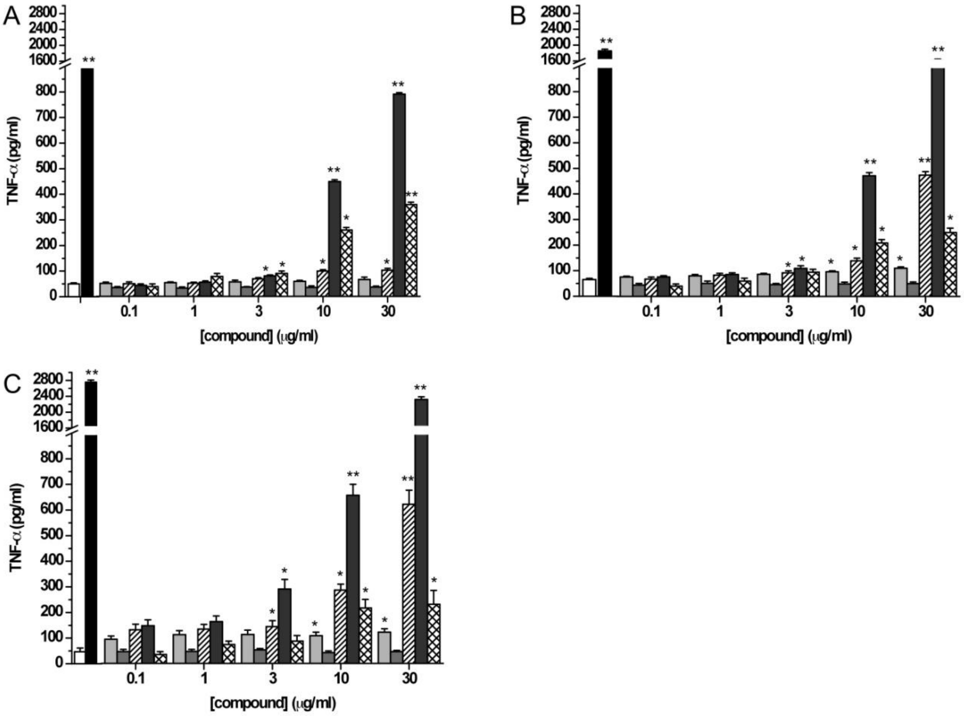

Figure 5.9 : Effects of 3, PEMNPs, CMNPs, GMNPs and GlcMNPs treatment on TNF-α release. RAW 264.7 cells were treated with increasing concentrations (0.1-30 μg/ml) of 3 (light grey bars), PEMNPs (grey bars), CMNPs (hatched bars), GMNPs (dark grey bars) or GlcMNPs (cross-hatched bars) for 24h (A), 48h (B) and 72h (C). Compound untreated cells (white bars) were considered as negative, while 0.1 μg/ml LPS-treated cells (black bars) as positive controls. Supernatants were collected and assayed for TNF-α levels by standard ELISA. The data represent mean ± SEM of at least three independent experiments. *$p \leq 0.05$; **$p \leq 0.01$ vs. controls (compound-untreated cells).

In agreement with data already published by other authors [7], our results showed the biological role played in cellular uptake by the monosaccharide used for the MNPs coating. As a matter of fact, it is known [7] that glucose coated MNPs are mainly internalized by caveolae-mediated endocytosis, while the galactose coated MNPs remain confined on the cell periphery and present a slower internalization kinetic. Although the mechanism of **GMNPs** uptake remains to be clarified, taking into account the structural similarity of the α-Tn mimetic antigen (decorating **GMNPs**) and galactose, it is reasonable to suppose that **GMNPs** may follow a cell entrance pattern and processing similar to galactose coated MNPs.

Overall, these data demonstrate that a multivalent display of α-Tn mimetic antigen is necessary for macrophage activation. Thus, macrophages, after processing MNPs as antigenic molecules, become, as discussed in Paragraph 5.1, active Antigen Presenting Cells, and through the production of various secondary mediators are capable to orchestrate further cell recruitment for immune responses. The macrophages activation is thus a key-point to establish a direct interconnection between innate and adaptive immunity and hence for the amplification of the immune response, making this novel nanostructured system a good candidate for immunotherapy applications.

References

[1] A. K. Abbas; A. H. Lichtman, *Basic Immunology: : Functions and Disorders of the Immune System*, Saunders; 3 edition (February 12, **2010**).

[2] S. Fallarini; T. Paoletti; C. O. Battaglini; P. Ronchi; L. Lay; R. Bonomi; S. Jha; F. Mancin; P. Scrimin; G. Lombardi, *Nanoscale*, **2013**, *5*, 390.

[3] D. O. Adams; T. A. Hamilton, *The cell biology of macrophage activation. Ann. Rev. Immunol.* **1984**, *2*, 283.

[4] T. Paoletti; S. Fallarini; F. Gugliesi; A. Minassi; G. Appendino; G. Lombardi, *Eur. J. Pharmacol.*, **2009,** *620*, 120.

[5] A. Kunzmann; B. Andersson; T. Thurnherr; H. Krug; A. Scheynius; B. Fadeel, *Biochim Biophys Acta*, **2011**, *1810*, 361.

[6] (a) S.Metz; G. Bonaterra; M. Rudelius; M. Settles; E. J. Rummeny; H. E. Daldrup-Link, *Eur. Radiol.* **2004**, *14*, 1851; (b) E. Allard-Vannier; S. Cohen-Jonathan; J. Gautier; K. Hervé-Aubert; E. Munnier; M. Soucé; P. Legras; C. Passirani; I. Chourpa, *Eur. J. Pharm. Biopharm.*, **2012**, *81*, 498.

[7] M. Moros; B. Hernáez; E. Garet; J.T. Dias; B. Sáez; V. Grazú; A. González-Fernández; C. Alonso; J.M. de la Fuente , *ACS Nano.* **2012,** 6, 1565-77.

6. Functionalization of MNPs

In Chapter 3 we described the functionalization of magnetite MNPs with the α-Tn antigen mimetic exploiting a phosphonate group for the anchoring on the iron oxide surface. This anchor group was introduced after the coupling of the mimetic with the monoamino derivative of the hexaethylene linker, treating the carbohydrate moiety with tris(trimethylsilyl) phosphite at a temperature of 100°C for 18h. Since, as a future perspective, we aim at extending the proposed approach to the functionalization of MNPs with other TACAs (tumour associated carbohydrate antigens) and in particular with a mimetic of the GM3 lactone that cannot undergo the harsh reaction conditions adopted for the α-Tn antigen mimetic, we developed different alternative strategies to anchor it to the inorganic core.

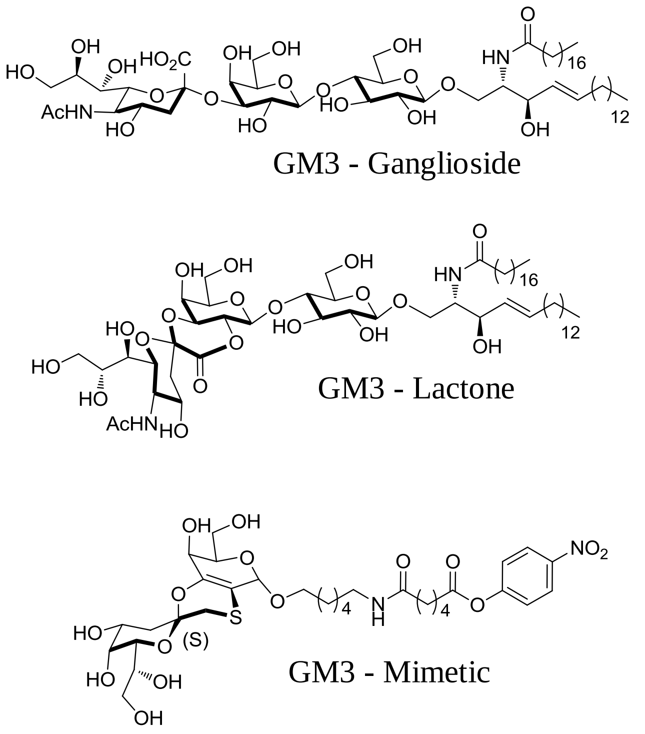

Figure 6.1 : Structures of the native GM3 ganglioside, its lactone form and the GM3 mimetic with a p-nitrophenol activated carboxylic group for the conjugation with free amino groups.

GM3 ganglioside (Figure 6.1) is a TACA overexpressed on melanoma cells with metastatic potential [1] and due to its high density [2] and the lower pH of tumour cells, undergoes lactonization leading to the formation of the GM3 lactone

[3]. It has been demonstrated that GM3 lactone is more immunogenic than GM3 ganglioside [4] but its instability under physiological pH, and thus the decreasing of its immunogenicity, led to the development of a stable mimetic of the GM3 lactone [5]. This mimetic was then modified with a linker bearing an activated carboxylic group for the conjugation to the protein carrier keyhole-limpet hemocyanin (KLH) able to elicit specific antimelanoma antibodies [6]. Further studies on the GM3 mimetic conjugated to complex peptidic structures are currently in progress. Since the coupling reaction between this activated carboxylic group and a free amino group can occur at room temperature in an aqueous medium, the strategy for the functionalization of MNPs was modified as schematically represented in Figure 6.2a. In particular, we prepared water soluble MNPs with free amino groups exposed to the external environment ready to be coupled with a carboxylic group present on the target molecule. These water soluble MNPs may be obtained by replacing the former surfactant with a bifunctional hydrophilic linker able on one side to bind the inorganic moieties and on the other to allow further functionalizations with the bioactive molecule (Figure 6.2b).

In Chapter 4 we have shown that the functionalization of nanoparticles with the bifunctional molecule 3-aminophosphonic acid was not completely satisfactory because of the non-optimal water solubility of the final product and the formation of some aggregates comprising few magnetic centers. In order to improve all of these aspects, two diverse bifunctional linkers were studied. In paragraph 6.1 the experiments concerning the ligand exchange process of oleic acid coated MNPs with an alkoxy silane ligand will be described, whereas the paragraph 6.2 will be focused on the synthesis of an amino-phosphonate bifunctional linker derived from hexaethyleneglycol.

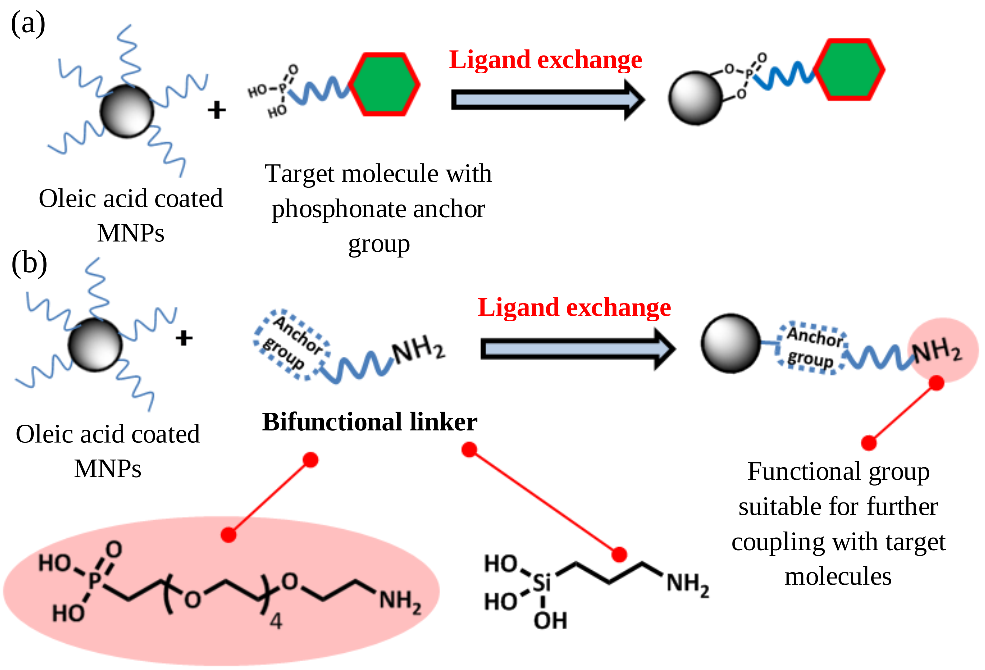

Figure 6.2 : The two strategies followed for the functionalization of MNPs.

6.1 Aminosilane functionalization

A ligand bearing a silane anchor group instead of the phosphonate was tested in order to improve the stability of the water dispersions and the amount of functionalization. Alkoxysilanes are indeed widely used for the functionalization of metal oxide surfaces and in particular for iron oxide nanoparticles as they form relatively strong covalent Si-O-Fe bonds.[7]

The ligand exchange process was performed on highly uniform spherical magnetite MNPs, **OlMNP2@290,** with average size 17 ± 1.4 nm synthesized by thermal decomposition of iron(III) oleate and then oxidized in solution by bubbling air following the same procedure described in Chapter 2.2 (Figure 6.3a). These MNPs were then reacted with 3-aminopropyltrimethoxy silane (APTMS) with catalytic acetic acid [7,8]. Different attempts were performed by varying the type of solvent and by carrying on the reaction with or without the presence of the surfactant. Performing the reaction in hexane without oleic acid it was not possible to obtain an optimal dispersion of the nanoparticles and some aggregates were observed. In fact about an hour after the addition of APTMS, the reaction mixture became turbid and the nanoparticles tended to stick to the flask walls as an effect of the formation of the silane coating. After twenty hours the nanoparticles were purified by magnetic decantation and washed to remove the excess of APTMS and eventual by-products. The final MNPs were not dispersible in water. Moreover, also decreasing the pH to 4-5 by adding a 0.1 M HCl solution in order to protonate the amino group present on the ligand so as to promote electrostatic repulsion, did not improve the solubility of the suspension.

In order to improve the stability of the dispersion of nanoparticles, avoiding the formation of aggregates after the ligand exchange process took place, the reaction was modified by adding oleic acid just before APTMS. In this case the functionalized MNPs resulted more soluble in water after sonication, although the stability was limited to few minutes, also in acidic condition.

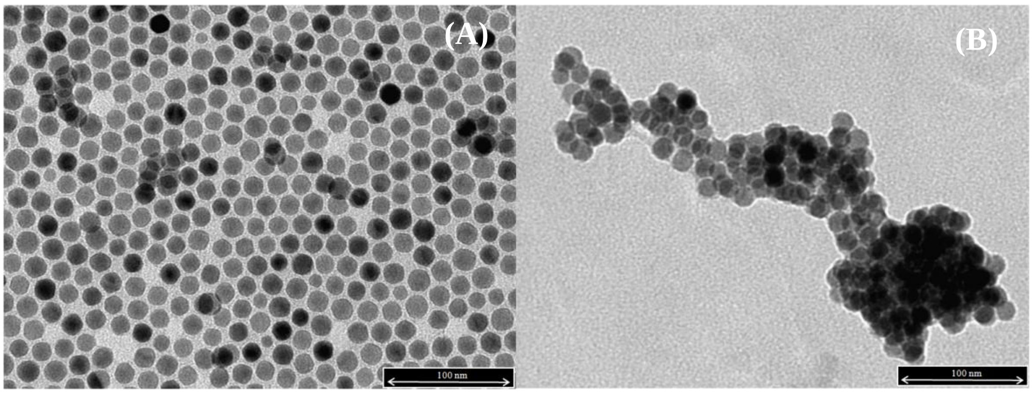

Figure 6.3 : comparison between (A) oleic acid coated MNPs, OlMNP2@290 used for the functionalization with APTMS and (B) the same MNPs after the ligand exchange process in hexane.

In Figure 6.3 the comparison between the MNPs coated with oleic acid (A) and the MNPs after the reaction with APTMS (B) is shown. In the first case the nanoparticles were well separated and each one was distinguishable from each other. In the case of MNPs functionalized with aminosilane, the formation of nanoparticles aggregates embedded in a matrix is clearly observable. In order to verify if the MNPs clusters were formed because of the lack of solubility in the former hexane dispersion, the reaction was repeated in toluene in the presence of oleic acid as surfactant. Using this solvent a more stable dispersion was achieved, suggesting a lower degree of aggregation occurred during the ligand exchange. As a matter of fact the product obtained after the reaction with APTMS was more soluble in water and the dispersion more stable, particularly in acidic conditions, although an aggregation process still occurred starting after about one hour. In Figure 6.4, a TEM image of the MNPs after the ligand exchange in toluene is reported; the image shows a decrease of the degree of aggregation and a smaller thickness of the organic matrix if compared to the sample prepared in hexane.

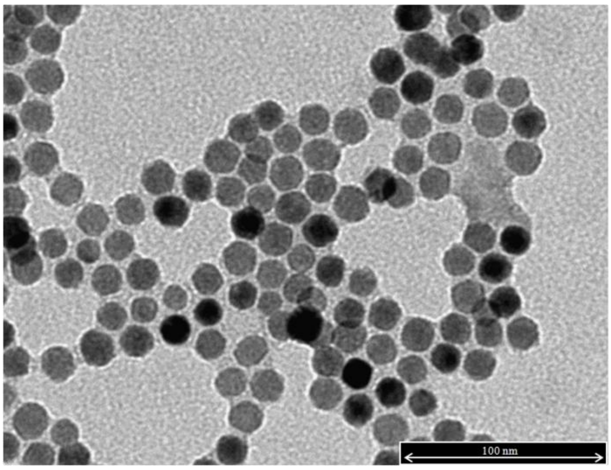

Figure 6.4 : image of MNPs functionalized with aminosilane using toluene as solvent for the ligand exchange process.

In this case the still non-optimal solubility was attributed to an incomplete functionalization of the nanoparticles with the aminosilane ligand. Thus, the functionalization process with APTMS was repeated twice on the same nanoparticles: in the first step a ligand exchange in toluene was performed and in the second step the obtained MNPs were redispersed in a 1:1 ethanol/water mixture and APTMS was added. At the end of each step the samples were purified by dialysis in a cellulose membrane and the process was monitored by elemental analysis, before and after purification in order to evaluate the amount of organic phase (Table 6.1).

	1st Step	**2nd Step**
Solvent	Toluene	1:1 EtOH/H_2O
Aminosilane % Before | After	8.5% | 6%	5.0% | 4.5%

Table 6.1: For each step is displayed the percentage of aminosilane found by elemental analysis before and after the purification by dialysis.

As shown in Table 6.1, a decrease of the organic phase during the whole two steps process is observed and after the purification of the second step the aminosilane percentage decreased from 8.5% to 4.5%, accompanied by a worsening of the water solubility. This result led to the conclusion that most of the functionalization occurred during the first step and the second reaction in polar solvent contributed only in removing the excess of the organic material adsorbed on the MNPs. Furthermore, the second addition of APTMS contributed to the aggregation by interparticle crosslinking as displayed in Figure 6.5 where a representative TEM image of the sample is shown.

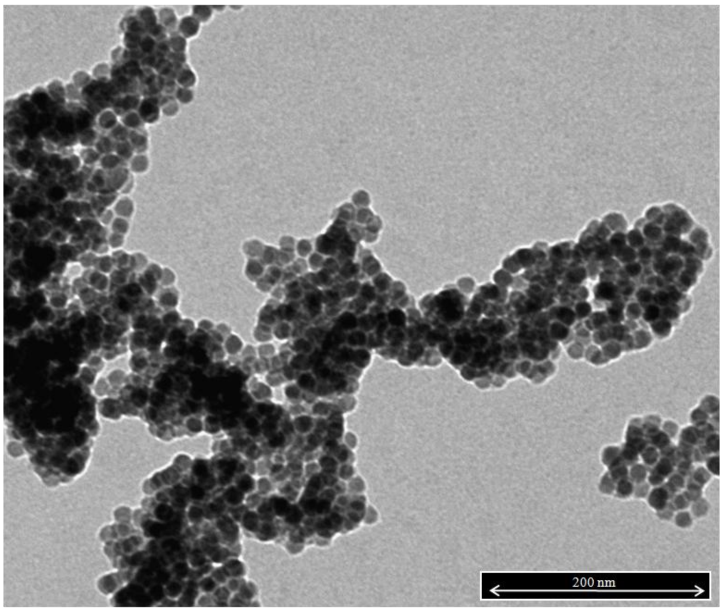

Figure 6.5 : TEM images of the MNPs after the second step of functionalization with APTMS

The explanation of the observed behavior is schematized in Figure 6.6: the APTMS ligand possesses three hydrolyzable alkoxy groups and, if on one hand it can form stable Fe-O-Si bonds with the iron oxide surface, on the other it may olygomerize forming Si-O-Si bonds with other APTMS molecules [9]. This olygomerization will lead to the formation of aggregates of uncontrolled large sizes and hence to the formation of unstable water dispersions.

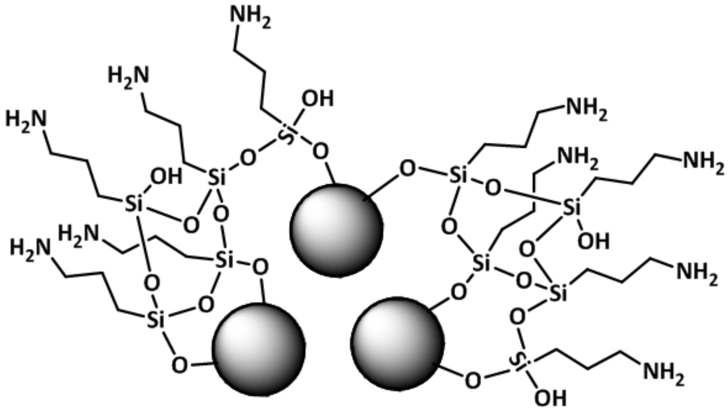

Figure 6.6 : Scheme describing APTMS olygomerization and formation of interparticle crosslinking.

6.2 Synthesis of aminophosphonic linker 39

In order to avoid olygomerization and hence interparticle crosslinking, efforts were directed towards the synthesis of a new ligand derived from hexaethylene glycol in which each of the two hydroxyl endings were substituted by a phosphonate group and an amino group, respectively. Another advantage obtained with this linker is the water solubility of the hexaethylene glycol derivatives that may increase the total water solubility of the MNPs after the ligand exchange. Also the stability of the MNPs dispersions may be positively affected by the length of this linker, longer than that of the other investigated ligands; a thicker organic shell may decrease dipolar interaction avoiding MNPs aggregation. Furthermore, the length of the hexaethylene glycol is necessary to guarantee an optimal presentation of the coupled antigen towards the external environments.

In Scheme 6.1 the synthesis of the amino-phosphonate linker **39** is reported. Details of each step and on the characterization of the intermediates and of the final product are given in experimental section.

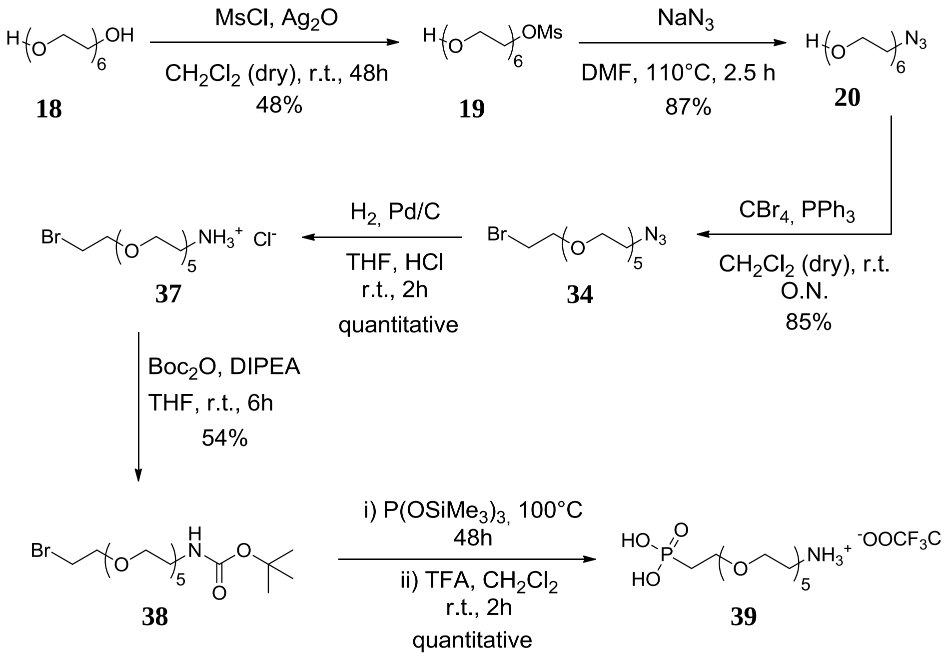

Scheme 6.1 : complete scheme for the synthesis of the amino-phosphonate linker.

For the synthesis of compound **20** was followed the same procedure described in Paragraph 3.3 [10].

The azido derivative **20** was then reacted with carbon tetrabromide and triphenylphosphine (PPh_3) and the free hydroxyl group was substituted with bromine affording **34** in 85% yield (Scheme 6.2).

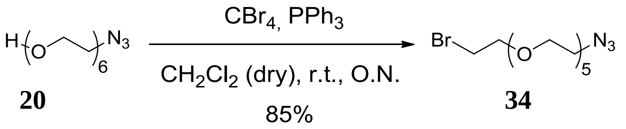

Scheme 6.2 : Synthesis of the bromine-azide derivative.

In order to get the desired ligand we first attempt to substitute the bromine with the phosphonate group, **34** by reaction with tris(trimethylsilyl) phosphite ($P(OSiMe_3)_3$) as reported in Scheme 6.3.

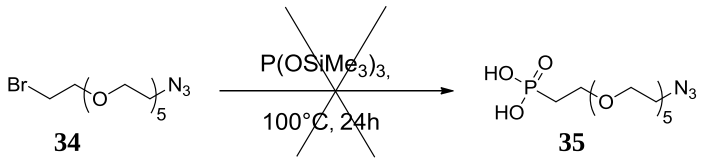

Scheme 6.3 : Reaction of the bromine-azide derivative with tris(trimethylsilyl) phosphite did not afford the desired product.

The reaction was monitored by NMR analysis and ESI-MS spectrometry highlighting the disappearance of the starting material and the appearance of signals belonging to unidentified side products, while no indication on the formation of product **35** was found. The reaction scheme was thus modified reducing the azide group to amine before the reaction with phosphite. The reaction was first performed by reacting the bromine-azide derivative under the Staudinger conditions (PPh_3 followed by aqueous hydrolysis) as shown in Scheme 6.4.

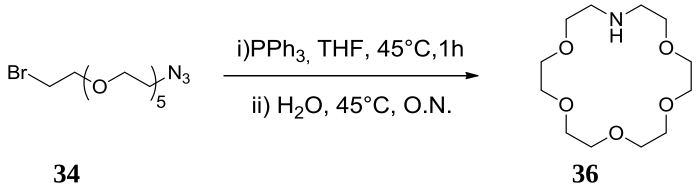

Scheme 6.4 : Attempt to reduce the azide group of 34 to amine under Staudinger conditions.

The monitoring of the reaction by ESI-MS spectrometry revealed a peak at m/z 264 attributed to product **36,** indicating that under this conditions the newly formed amino group led to the nucleofilic attack to the carbon bound to the bromine atom causing the formation of the stable crown ether **36**. In order to avoid the formation of this cyclic compound the reduction was then performed using H_2 with Pd/C catalyst in the presence of HCl in order to protonate the amino group as soon as it is formed, preventing the cyclization reaction (Scheme 6.5).

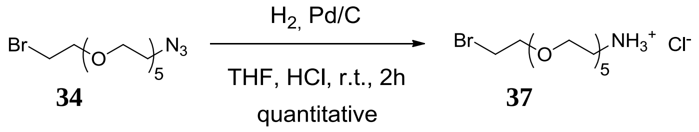

Scheme 6.5 : Successfully reduction of the azide group to amine.

Following this reaction conditions, the product **37** was obtained in quantitative yield. The insertion of the phosphonate group was then attempted using **37** as substrate by reaction with $P(OSiMe_3)_3$ (Scheme 6.6). The reaction was monitored by ESI-MS spectrometry and we observed the progressive disappearance of the starting material and the appearance of a peak at m/z 264 attributed to the compound **36** and others unidentified peaks of side products.

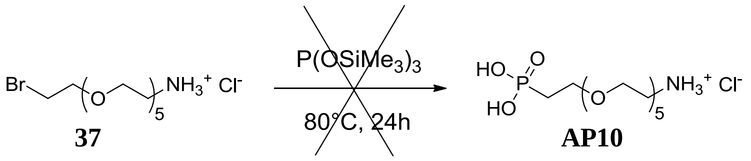

Scheme 6.6 : Attempt of phosphonate insertion starting from the bromine-amino derivative.

In order to avoid this side reactions caused by the presence of the free amino group in the reaction with $P(OSiMe_3)_3$, **37** was reacted with di-*tert*-butyl dicarbonate (Boc_2O) leading to the Boc-protected compound **38** in 54% yield (Scheme 6.7).

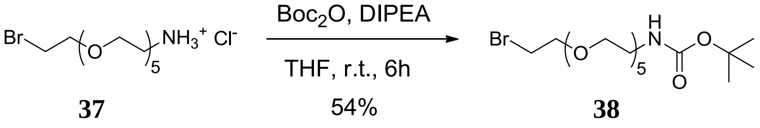

Scheme 6.7 : Protection of amino group with di-tert-butyl carbonate.

The phosphonate insertion was accomplished by heating **38** in the presence of $P(OSiMe_3)_3$. The crude product was treated with trifluoroacetic (TFA) acid in order to remove the Boc protecting group affording the final product **39** in quantitative yield (Scheme 6.8).

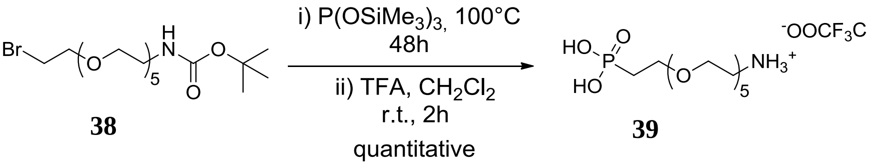

Scheme 6.8 : Synthesis of the final amino-phosphonate linker.

In this case the reaction with phosphite did not lead to the formation of unwanted side products confirming the goodness of the choice of the amine protection with the Boc protecting group. Furthermore, a simple treatment with TFA afforded the linker bearing at the two ends a phosphonate and an amino group necessary for the anchorage to the iron oxide surface of the MNPs and the following coupling reaction with target molecules with an activated carboxylic group.

References

[1] (a) Y. Harada; M. Sakatsume; M. Taniguchi Jpn., *J.Cancer Res.*, **1989**, *80*, 988; (b) M. Tardif; J. Coulombe; D. Soulieres; A.P. Rousseau; G. Pelletier, *Int. J.Cancer*, **1996**, *68*, 97.

[2] Y. Harada; M. Sakatsume; M. Taniguchi, *Jpn. J.Cancer Res.*, **1990**, *81*, 383.

[3] I. Kawashima; M. Kotani; H. Ozawa; M. Suzuki; T. Tai, *Int. J.Cancer*, **1994**, *58*, 263.

[4] (a) G. A. Nores; T. Dohi; M. Taniguchi; S. Hakomori; *J. Immunol.*, **1987**, *139*, 3171; (b) Y. Harada; M. Sakatsume; M. Taniguchi; *Jpn. J. Cancer Res.*, **1990**, *81*, 383.

[5] L. Toma; E. Di Cola; A. Ienco; L. Legnani; C. Lunghi; G. Moneti; B. Richichi; S. Ristori; D. Dell'Atti and Cristina Nativi, *ChemBioChem*, **2007**, *8*, 1646.

[6] A. Arcangeli; L. Toma; L. Contiero; O. Crociani; L. Legnani; C. Lunghi; E. Nesti; G. Moneti; B. Richichi; C. Nativi, *Bioconjugate Chem.*, **2010**, *21*, 1432.

[7] (a) R. De Palma; S. Peeters; M. J. Van Bael; H. Van den Rul; K. Bonroy; W. Laureyn; J. Mullens; G. Borghs and G. Maes, *Chem. Mater.*, **2007,** *19*, 1821; (b) S. Laurent; M. Mahmoudi, *Int. J. Mol. Epidemiol. Genet.*, **2011**, *2(4)*, 367.

[8] (a) Y. Zhang; N. Kohler; M. Zhang, *Biomaterials,* **2002,** *23*, 1553; (b) M. Ma; Y. Zhang; W. Yu; H. Shen; H. Zhang; N. Gu, *Colloids and Surfaces A: Physicochemical and Engineering Aspects*,**2003**, *212,* (2–3), 219.

[9] B. A. Larsen; K. M. Hurst; W. R. Ashurst; N. J. Serkova; C. R Stoldt, *J. Mater. Res.*, **2012**, *27*(14), 1846.

[10] F. Menger, M. Hailing Zhang, *J. Am. Chem. Soc.* **2006**, *128*, 1414.

7. Conclusions and perspectives

The aim of this work was to exploit the inorganic core of magnetite MNPs as a multivalent scaffold for applications in the therapy of diseases, preserving all the advantages offered by their magnetic properties, in addition to those coming from the functionalization with bioactive molecules allowing for specific interactions with target receptors.

In particular, we focused on the development of a nanostructured system composed by magnetite MNPs decorated in a multivalent manner with the α-Tn antigen mimetic **3**, a tumour associated antigen, for application in immunotherapy. The synthesis of MNPs was accomplished by the thermal decomposition of $Fe(acac)_3$ in a high boiling solvent, exploiting the seed mediated growth process to obtain 11 nm MNPs from seeds with a size of 7 nm. The obtained material was highly crystalline, with a narrow size distribution and with good magnetic properties. The functionalization of MNPs was carried out thanks to the presence of the phosphonate group, on the mimetic moiety, which has a great affinity towards iron oxide, leading to a stable bond between the galactosyl epitope and MNPs. *In vitro* tests performed on the α-Tn functionalized MNPs revealed their ability to be engulfed by macrophages and the ability to activate macrophage effector function, inducing gene expression and protein release of TNF-α. Compared to the negative controls, only **GMNPs** was able to induce macrophages activation, demonstrating that a multivalent presentation of the α-Tn epitopes was necessary. The crucial importance of these results rely on the role played by macrophages in the immune response. The cross-interaction between macrophages and T lymphocytes acts like a *bridge* from the innate immunity and the adaptive immunity making a great contribution to the amplification of the immune response. This novel nanostructured system is thus proposed as an original immunoactive tool, which could find practical applications in immunotherapy as well as for a better understanding of the biological properties and clinical applicability of MNPs. Of course, further *in vivo* studies on **GMNPs** are needed in order to fully assess their immunoactivity and to evaluate their biodistribution by MRI.

A further valuable advantage of this nanosystem is undoubtedly provided by the presence of an “active” magnetic core, whose properties can be exploited to enlarge the number of functionalities and its efficiency. To this aim, and also considering the drawbacks which affect the synthetic strategies commonly adopted for the preparation of MNPs, large efforts were devoted to the synthesis of nanomaterials optimized for magnetic fluid hyperthermia. Different procedures for the synthesis of MNPs were thus investigated in order to synthesize larger MNPs (in the 12-15 nm range) in a one step reaction avoiding any seeded process, which affect the magnetic properties of the final product. MNPs with this size will improve their magnetic and hyperthermic properties without affecting their solubility and hence their suitability for further functionalization, essential for biomedical application. We found the best experimental conditions, described in Paragraph 2.3.2 for sample **IAMNP9**, were based on using Fe(acac)$_3$ as metal-organic precursor for thermal decomposition reaction using benzylether as high boiling solvent and oleic acid and oleylamine as surfactants. Indeed, these parameters, along with a specific heating rate ramp led to MNPs of ca. 14 nm with a narrow size distribution, high magnetic moment and a SAR value that could also allow for hyperthermic application. We found that this particular size represents the best compromise between magnetic/hyperthermic properties and colloidal stability, two features which are of fundamental importance for the proposed biomedical application. Hence, these MNPs represent the first building block to be employed as multivalent scaffold for further functionalization with bioactive molecules, for the realization of a novel multifunctional tool for the therapy of tumors.

The final part of this work was aimed at developing a more versatile strategy towards the functionalization of MNPs compared to that exploited for **GMNPs:** instead of modifying the bioactive molecule to be linked to the MNPs moiety, by the insertion of the phosphonate functional group, a more general approach was realized by: i) substitution of the former oleic acid surfactant by a ligand exchange reaction with a bifunctional linker; ii) coupling of the target molecule to MNPs.

To this purpose, a new water soluble bifunctional linker derived from hexaethylene glycol was synthesized. The linker bears a phosphonate group for the anchorage to the MNPs surface at one end, and an amino group for the coupling with the target molecule via amide bond, on the other. MNPs functionalized with this new linker could be coupled with a series of different molecule depending on the final purpose offering a versatile tool for the preparation of targeted MNPs for biomedical application. In particular, as a future perspective, our efforts will be directed towards the functionalization of MNPs with a mimetic of the GM3 lactone, a TACA antigen, related to the development of melanoma (see Chapter 6). The improvements obtained concerning the synthesis of MNPs with suitable size and magnetic properties, and the synthesis of this new bifunctional linker, have represented a first fundamental step towards the development of novel nanostructured systems for theranostic applications. Indeed, we have now all the building blocks to be assembled into a unique system for the desired applications.

Moreover, the preliminary *in vitro* results have shown the potential of MNPs in the realization of multifunctional nanosystems and in particular their versatility in a new field of application such as immunotherapy.

8. Experimental section

Abbreviations

Fe(ole)$_3$:	Iron(III) oleate
Fe(acac)$_3$:	Iron(III) acetyacetonate
DMF:	dimethylformamide
APTMS:	3-aminopropyltrimethoxy silane
Et$_2$O:	diethyl ether
PE:	petroleum ether
EtOac:	ethyl acetate
Ar:	aromatic
TFA:	trifluoroacetic acid
NEt$_3$:	triethylamine
Boc:	*tert*-butyloxycarbonyl
TBTU:	*O*-(benzotriazol-1-yl)-*N,N,N′,N′*-tetramethyluronium tetrafluoroborate
THF:	tetrahydrofurane
DMAP:	dimethyaminopyridine
PhtNSCl:	phthalimidesulfenyl chloride
DIPEA:	*N*,*N*-Diisopropylethylamine
Me:	methyl
Ac:	acetyl
Bn:	benzyl
t-Bu:	*tert*-butyl
Boc:	*tert*-butyloxycarbonyl
m.p.:	melting point
rt:	room temperature

8.1 Synthesis of MNPs

Synthesis of IOMNP1, IOMNP2, IOMNP3, IOMNP4

In a typical thermal decomposition reaction, dried FeOOH fine powder was mixed with oleic acid and 1-octadecene in a three neck round bottom flask equipped with magnetic stirrer, thermocouple and heating mantle. For **IOMNP1** and **IOMNP2** the reaction mixture was purged under nitrogen flow before heating and was maintained under a blanket of nitrogen until the end of the heating ramp; **IOMNP3** was carried out in air atmosphere; for **IOMNP4** a flux of air was bubbled directly in the reaction mixture since the temperature raised to 180°C. The reaction mixture was heated accordingly to the heating rate ramp shown in Figure 8.1. After the last step at 300°C the reaction mixture was cooled to room temperature, diluted with a 2:1 isopropanol-hexane mixture (150 mL), and the precipitated material was recovered with a permanent magnet. The obtained material was purified by several washing steps with isopropanol and ethanol. In Table 8.1 the reagent quantities used in each reaction are reported.

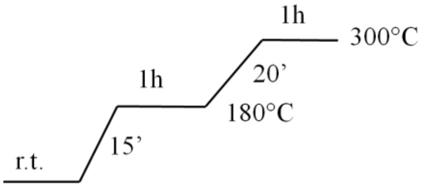

Figure 8.1 : Heating rate ramp for the thermal decomposition reactions of FeOOH.

	FeOOH		Oleic acid		1-octadecene
	G	mmol	g	mmol	V (mL)
IOMNP1	0.712	8.0	8.950	31.7	25
IOMNP2	0.364	4.1	6.214	22.0	50
IOMNP3	0.364	4.1	6. 214	22.0	50
IOMNP4	0.364	4.1	6. 214	22.0	50

Table 8.1 : Reagents quantities used for each reaction with FeOOH.

Synthesis of $Fe(ole)_3$

A solution of $FeCl_3·6H_2O$ (2.22 g, 8.23 mmol) and sodium oleate (7.54 g, 24.8 mmol) in a 1:1.33:2.33 mixture of ethanol-water-hexane, was heated at 70°C under magnetic stirring for 4h. The reaction mixture was then washed with water (3x6 mL) in a separatory funnel and the organic phase dried with anhydrous Na_2SO_4 and concentrated to dryness to give $Fe(ole)_3$ as a red-brownish waxy solid.

Synthesis of OlMNP1, OlMNP1@290, OlMNP2, OlMNP2@290

In a typical thermal decomposition reaction, a solution of $Fe(ole)_3$ (2.310 g, 2.6 mmol) and oleic acid (2.440 g, 7.8 mmol), in 1-octadecene (20 mL) was purged under nitrogen flow for 15' and then heated according to the heating rate ramp reported in Figure 8.2 (t_r=4h for **OlMNP1** and t_r=1.5h for **OlMNP2**) . The reaction mixture was then cooled to room temperature, diluted with isopropanol (100 mL) and the precipitated material was recovered with a permanent magnet. The black material recovered was purified first by dissolving in hexane and precipitating with isopropanol and then by several washing steps with isopropanol and ethanol. The obtained **OlMNP1** and **OlMNP2** were then oxidized by dissolving in 1-octadecene (50 mL) and oleic acid (3.00 g, 10.6 mmol) and heating up the reaction mixture to 290°C for 15' with a flux of air bubbled in the reaction mixture. After cooling to room temperature the reaction mixture was diluted with isopropanol (100 mL) and the MNPs were recovered with a permanent magnet and washed with isopropanol and ethanol giving product **OlMNP1@290** and **OlMNP2@290**.

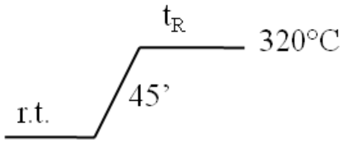

Figure 8.2 : Heating rate ramp. t_r=4h for OlMNP1 and t_r=1.5h for OlMNP2.

Synthesis of IAMNP1 and IAMNP2

Magnetite MNPs **IAMNP2** were synthesized using a seed-mediated growth process based on the Sun's method [1]. A solution of iron (III) acetylacetonate (0.96 g, 2.73 mmol), oleylamine (2.20 g, 8.21 mmol), oleic acid (2.33 g, 8.25 mmol) and 1,2-hexadecanediol (3.53 g, 13.65 mmol) in 1-octadecene (20 mL) was stirred at rt under a nitrogen flow for 1h, then heated to reflux (ca. 320°C) at a rate of 5°C/min and maintained at that temperature for 3h. The mixture was cooled to rt and diluted with a 1:1 toluene/heptane solution (10 mL). The mixture was treated with a 1:1 ethanol/isopropanol solution and the precipitated material was recovered using a permanent magnet. The obtained black powder was washed several times with ethanol and then re-dispersed in heptane. This solution was centrifuged at 2500 rpm for 15 min. Ethanol was added to the supernatant and 7 nm MNPs were separated using a permanent magnet and then vacuum dried giving product **IAMNP1**. The obtained **IAMNP1** were used as seeds to grow larger MNPs in a second thermal decomposition reaction: the MNPs (0.080 g) were mixed with iron (III) acetylacetonate (0.601 g, 1.68 mmol), oleylamine (1.92 g, 7.18 mmol), oleic acid (1.58 g, 5.59 mmol) and 1,2-hexadecanediol (2.22 g, 8.60 mmol) in 1-octadecene (20 mL). Larger particles, **IAMNP2**, were obtained following the same procedure described above.

Synthesis of IAMNP3, IAMNP4, IAMNP5, IAMNP6, IAMNP7, IAMNP8

In a typical reaction, a solution of Fe(acac)$_3$ (0.354 g, 1.0 mmol), oleic acid (1.284 g, 4.5 mmol), oleylamine (0.936 g, 3.5 mmol) in benzylether (50 mL for **IAMNP3, IAMNP4**, and 25 mL for **IAMNP5, IAMNP6, IAMNP7, IAMNP8**) was purged under nitrogen flow for 15' and then heated according to the heating rate ramp reported in Figure 8.3a for **IAMNP3, IAMNP4** and Figure 8.3b for **IAMNP5, IAMNP6, IAMNP7, IAMNP8**. The reaction mixture was then cooled to rt and diluted with ethanol (250 mL). The precipitated material was recovered using a permanent magnet and washed several times with ethanol. The black powder obtained was then vacuum dried.

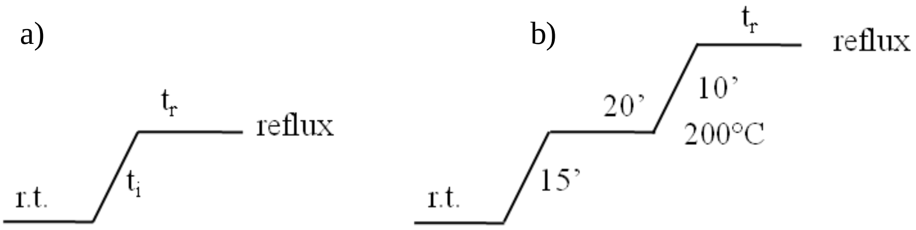

Figure 8.3 : Heating rate ramp a) t_i=50',t_r=50' for IAMNP3, t_i=20',t_r=40' for IAMNP4; b) t_r=15' for IAMNP5, t_r=40' for IAMNP6, t_r=1.5h for IAMNP7, t_r=11' for IAMNP8.

Synthesis of IAMNP9

A solution of Fe(acac)$_3$ (0.706 g, 2.0 mmol), oleic acid (2.542 g, 9.0 mmol) and oleylamine (1.873 g, 7.0 mmol) in benzylether (30 mL) was purged under nitrogen flow for 15' and then heated according to the heating rate ramp reported in Figure 8.4. The reaction mixture was then cooled to rt and diluted with ethanol (250 mL). The precipitated material was recovered using a permanent magnet and washed several times with ethanol. The black powder obtained was then vacuum dried.

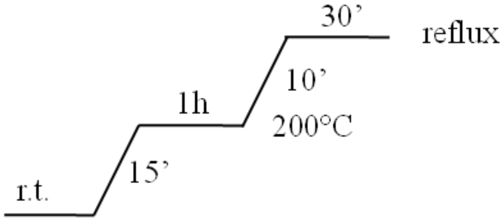

Figure 8.4 : Heating rate ramp exploited for the synthesis of sample IAMNP9.

8.2 Functionalization of MNPS

Synthesis of GMNPs

MNPs **IAMNP** (47.2 mg) were added to a solution of **3** (25 mg, 0.038 mmol) in 4.4 mL of 10:1 chloroform/methanol, and the mixture was mechanically stirred at 48°C for 48h. Methanol was then added to the mixture causing precipitation of MNPs. The product was washed with methanol and chloroform in order to remove unbound ligand and oleate-coated MNPs and then was vacuum dried. The product was dispersed in water by sonication. The solution was separated from the precipitate in order to collect only the water soluble MNPs. The recovered solution was then freeze-dried leading to a black-brown powder of glycosylated MNPs, **GMNPs**. In order to improve the water solubility of the MNPs, 1.5 mg of **GMNPs** were mixed with phosphonate **3** (1 mg, 0.0015 mmol) in mQ water (0.8 mL) and stirred at 45°C for 48h. MNPs were magnetically decanted and washed twice with water to remove the unbound ligand.

Synthesis of CMNPs

In a round bottom flask a 1:1 solution of 1,2-dichlorobenzene/DMF (2.5 mL) was stirred under a nitrogen flow for 30’, then **IAMNP** (19.3 mg) and monohydrated citric acid (20 mg, 0.05 mmol) were added. The reaction mixture was stirred under a blanket of nitrogen at 100°C, for 23h. After cooling at rt, ethyl ether was added and the dark-brown material was magnetically decanted. The as obtained **CMNPs** were washed three times with acetone and then vacuum dried.

Synthesis of GlcMNPs

To a suspension of **IAMNP8** (11.4 mg) in hexane (0.16 mL), an emulsion of tetramethyammonium aminopropylphosphonate salt (0.022 g) in a mixture of dichloromethane (2 mL) and water (0.05 mL), was added. The reaction mixture was sonicated for 30' and then the MNPs were recovered with a permanent magnet and washed with isopropanol. To a suspension of the as obtained MNPs in a 1:20 water/DMF mixture, a solution of **24** in DMF (1 mL**)** was added. The reaction mixture was stirred at rt for 24h and then diluted with a 1:1 isopropanol/hexane mixture. The as obtained **GlcMNPs** were recovered with a permanent magnet, washed with ethanol and dispersed in water (1.5 mL).

Synthesis of PEMNPs

A toluene solution of **IAMNP** (2 mL, 10 mg/mL) was diluted in hexane (50 mL) and mixed with a solution of methoxy(polyethylenoxy)propyltrimethoxysilane 9-12 PE units (300 µL) in a 5:1 hexane/chloroform solution (30 mL). Glacial acetic acid (8 µL, 0.14 mmol) was added to the reaction mixture and the solution was stirred at rt for 15h. MNPs were separated from the supernatant. The product was washed with chloroform and precipitated with hexane with the assistance of a permanent magnet. After the washing step the as obtained **PEMNPs** were dispersed in water (10 mL).

Functionalization with APTMS

Here we describe the reaction condition employed for the functionalization of MNP with APTMS discussed in Chapter 6.

Experiments were performed: i) in hexane without oleic acid; ii) in hexane with oleic acid; iii) in toluene with oleic acid. Typically, 10 mg of **OlMNP2@290** were suspended in hexane or toluene (50 mL). When the reaction was performed in the presence of the surfactant, oleic acid (0.025 g) was added to the suspension. Then glacial acetic acid (5µL, 0.08 mmol) and APTMS (250 µL, 1.4 mmol) were added. The reaction mixture was stirred for 24h, then the MNPs were recovered with a permanent magnet and washed twice with hexane and twice with ethanol.

In the case of the further reaction step in water/ethanol: 65 mg of MNPs treated with APTMS in toluene with oleic acid, as described above, were dispersed in a 1:1 water/ethanol mixture, then glacial acetic acid (85 µL, 1.36 mmol) and APTMS (500 µL, 2.8 mmol) were added. The reaction mixture was stirred at rt for 24h, then the MNPs were recovered with a permanent magnet and washed with ethanol.

8.3 Synthesis of linker 5

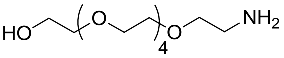

5

Monomesylatedhexaethyleneglycol **19** and monoazidehexaethyleneglycol **20** were prepared following a reported procedure [2]. Triphenylphosphine (0.480 g, 1.83 mmol) was added to an ice-cooled solution of **20** (0.271 g, 0.88 mmol) in dry THF (2.5 mL). The solution was warmed at 45°C for 2h then H_2O (130 μL) was added. The reaction mixture was stirred for 15 h at 35°C then diluted with H_2O (6 mL) and washed with toluene (2 x 4 mL). Evaporation of the aqueous layer under reduced pressure gave **5** (0.240 g, 97%) as a pale yellow oil. The spectroscopic and analytical data were in agreement with those reported previously [2].

^{1}H NMR (400 MHz, $CDCl_3$) δ: 3.66-3.46 (m, 22H); 2.80 (t, J= 5.1 Hz, 2H)

^{13}C NMR (100 MHz, $CDCl_3$) δ: 77.3, 77.0, 76.6, 73.0, 72.8, 70.6, 70.5, 70.4, 70.2, 70.1, 61.4, 41.5.

8.4 Synthesis of α-Tn antigen mimetic 3

Synthesis of 7

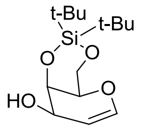

7

To a solution of D-(+)-galactal (1.00 g, 6.88 mmol) in dry DMF (27 mL) cooled to -45°C, *tert*-$Bu_2Si(OTf)_2$ (2.5 mL, 7.72 mmol) was slowly added. The solution was stirred at -45 °C for 1 h and then anhydrous pyridine (1.50 mL, 18.05 mmol) was added. The mixture was warmed to 0°C and a saturated solution of $NaHCO_3$ was added until pH=6. The mixture was diluted with Et_2O and washed with water (3x25 mL). The organic layer was dried over Na_2SO_4, filtered, and the solvent was removed under vacuum to give **7** (1.77 g, 90%) as a white solid, and used for the following reaction without further purification. The spectroscopic and analytical data were in agreement with those reported previously [3].

p.f. 103-105°C

^{1}H NMR (200 MHz, $CDCl_3$) δ: 6.29 (dd, 1H, $J_{1,2}$= 6.2 Hz, $J_{1,3}$= 1.4 Hz, H-1); 4.70 (dt, 1H, $J_{2,1}$= 6.6 Hz, H-2); 4.41-4.31 (m, 2H, H-3, H-4); 4.24-4.26 (m, 2H, CH_2-6); 3.87 (bs, 1H, H-5); 2.74 (d, 1H, J= 11.4 Hz, OH); 1.07-1.00 (m, 18H, CH_3 t-BuSi).

Synthesis of 8

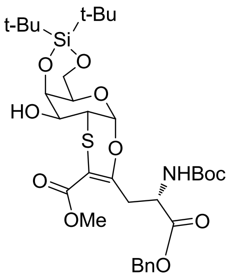

8

To a solution of **7** (0.50 g, 1.75 mmol) in $CHCl_3$ (2.5 mL), the β-chetoester [4] **10** (0.797 g, 2.10 mmol), pyridine (1.7 mL, 21.01 mmol) and PhtNSCl **14** [4] (1.16 g, 5.50 mmol) were added. The mixture was heated to 45 °C and stirred for 16 h, then it was diluted with CH_2Cl_2 (42 mL) and washed with a saturated solution of NH_4Cl (3x17 mL). The organic layer was dried over Na_2SO_4 and the solvent was removed under vacuum. After crystallization from Et_2O and removal of phtalimmide the filtrate was concentrated to dryness and the residue was purified by flash chromatography on silica gel (PE/EtOAc 4:1, Rf = 0.53) to afford **8** (0.628 g, 0.90 mmol, 52%) as a pale yellow solid. The spectroscopic and analytical data were in agreement with those reported previously [3].

p.f. 85-86°C

^{1}H NMR (200 MHz, $CDCl_3$) δ: 7.38-7.30 (m, 5H, Ar); 5.63 (d, 1H, , $J_{1,2}$=2.8 Hz, H-1); 5.39 (bd, 1H, NH); 5.22-5.07 (m, 2H, CH_2 Bn); 4.70-4.57 (m, 1H, H-4'); 4.38 (m, 1H, H-4); 4.31-4.16 (m, 2H, CH_2-6); 4.04 (bs, 1H, H-5); 3.74 (s, 3H, OCH_3); 3.74-3.56 (m, 2H, H-3, H-3'); 3.24 (dd, 1H, $J_{2,1}$= 3.0 Hz, $J_{2,3}$= 10.6 Hz, H-2); 2.86 (B part of an ABX system, 1H, J_{AB}= 14.0 Hz, J_{BX}= 4.4 Hz, H_B-3'); 2.65 (bd, 1H, J= 10.0 Hz, OH); 1.41 (s, 9H, 3 CH_3 t-Bu Boc); 1.05 (s, 9H, 3 CH_3 t-BuSi); 1.04 (s, 9H, 3 CH_3 t-BuSi).

Synthesis of 16

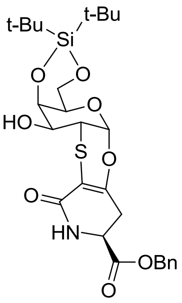

16

To a solution of **8** (0.983 g, 1.41 mmol) in dry CH_2Cl_2 (35 mL), TFA (3.2 mL, 41.58 mmol) was slowly added at 0 °C. The solution was stirred at rt for 2 h, then the mixture was concentrated to dryness. The solid obtained was re-dissolved in $CHCl_3$ and NEt_3 (3.4 mL, 24.64 mmol) was added. The mixture was heated to 40°C and stirred for 36h, then it was diluted with $CHCl_3$ (200 mL) and washed with water (1x25 mL), with a saturated solution of NH_4Cl (2x30 mL) and brine (2x30 mL). The organic layer was dried over Na_2SO_4 and the solvent was removed under vacuum to afford **16** (0.753 g, 95% yield over two steps) as a white solid, and used for the following reaction without further purification. The spectroscopic and analytical data were in agreement with those reported previously [3].

m.p.: dec. T>210°C

^{1}H NMR (200 MHz, $CDCl_3$) δ: 7.38-7.30 (m, 5H, Ar); 5.97 (bs, 1H, NH); 5.63 (d, 1H, $J_{1,2}$= 2.6 Hz, H-1); 5.30-5.22 (m, 2H, CH_2 Bn); 4.51 (d, 1H, $J_{4,3}$= 2.6 Hz, H-4); 4.35-4.25 (m, 3H, H-5’, CH_2-6); 3.99 (bs, 1H, H-5); 3.66-3.74 (m, 1H, H-3); 3.47 (dd, 1H, $J_{2,1}$= 2.6 Hz, $J_{2,3}$= 10.6 Hz, H-2); 2.79 (d, 3H, J= 8.8 Hz, CH_2-6’+ bd OH); 1.07-1.05 (m, 18H, CH_3 tBuSi).

Synthesis of 17

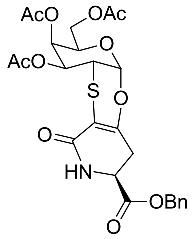

17

The glycosylsilylidene **16** (0.753 g, 1.34 mmol) was dissolved into a freshly prepared solution of tributylamine hydrofluoride in THF (14.0 mL, 1M). The reaction mixture was stirred for 1 h at rt and then concentrated to dryness. The residue was dissolved in CH_2Cl_2 (8 mL) and then pyridine (3.3 mL, 40.2 mmol), acetic anhydride (1.27 mL, 13.4 mmol) and 4-dimethylaminopyridine (33 mg, 0.27 mmol) were added. The reaction mixture was stirred at rt for 10’ and then diluted with CH_2Cl_2 (200 mL) and washed with water (2 x 20 mL), with a 3% solution of HCl (2 x 20 mL) and with a saturated solution of Na_2CO_3 (2 x 20 mL). The organic phase was dried over Na_2SO_4, filtered and concentrated to dryness. The crude was purified by flash column chromatography on silica gel (CH_2Cl_2/Acetone, 7/1) to give **17** (0.618 g, 85%) as a white solid.

m.p.: 173-175°C

$[\alpha]_D^{25}$ = + 89.3 (c 0.75, $CHCl_3$);

^{1}H NMR (400 MHz, $CDCl_3$) δ: 7.41-7.32 (m, 5H, Ph), 5.97 (bs, 1H, NH), 5.66 (d, $J_{1,2}$ = 2.8 Hz, 1H, H_1), 5.42 (dd, $J_{4,3}$ = 3.2 Hz, $J_{4,5}$ = 1.2 Hz, 1H, H_4), 5.26-5.23 (A part of an AB system, J_{AB} = 12.0 Hz, 1H, CH_2Ph), 5.22-5.19 (B part of an AB system, J_{BA} = 12.0 Hz, 1H, CH_2Ph), 5.06 (dd, $J_{3,2}$ = 11.6 Hz, $J_{3,4}$ = 2.8 Hz, 1H, H_3), 4.43 (at, J = 6.8 Hz, 1H, H_5), 4.43-4.34 (m, 1H, $H_{5'}$), 4.14-4.13 (m, 2H, H_{6a}, H_{6b}), 3.62 (dd, $J_{2,3}$ = 11.6 Hz, $J_{2,1}$ = 2.4 Hz, 1H, H_2), 2.91-2.85 (A part of an ABX system, J_{AB} = 17.6 Hz, J_{AX} = 6.0 Hz, 1H, $H_{4a'}$), 2.83-2.75 (B part of an ABX system, J_{BA} = 16.8 Hz, J_{BX} = 11.2 Hz, 1H, $H_{4b'}$), 2.16 (s, 3H, $COCH_3$), 2.06 (s, 3H, $COCH_3$), 2.02 (s, 3H, $COCH_3$)

^{13}C NMR (100 MHz, $CDCl_3$) δ: 170.5 (Cq), 170.1 (Cq), 169.9 (Cq), 169.1 (Cq), 164.3 (Cq), 154.0 (Cq), 134.7 (Cq), 129.0 (CH, Ph), 128.9 (CH, Ph), 128.6 (CH, Ph), 98.2 (Cq), 95.9 (C_1), 69.1 (C_5), 68.1 (CH_2Ph), 67.2 (C_4), 65.7 (C_3), 61.6 (C_6), 51.5 ($C_{5'}$), 36.6 (C_2), 30.9 ($C_{4'}$), 20.8 ($COCH_3$), 20.7 ($COCH_3$)

ESI-MS: m/z 571.84 $[M+Na]^+$, 585.83 $[M+K]^+$

Elemental Analysis for $C_{25}H_{27}NO_{11}S$: calc. C 54.64, H 4.95, N 2.55; found C 54.32, H 4.80, N 2.

Synthesis of 4

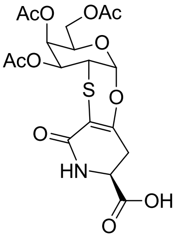

4

To a solution of **17** (0.201 g, 0.36 mmol) in THF (14 mL), H_2O (0.200 ml) and 10% Pd/C (140 mg, 0.04 mmol) were added. The mixture was stirred at rt under H_2 atmosphere for 2.5 h and then filtered through a pad of Celite®. Evaporation of the solvent under vacuum gave 185 mg of crude **4** which was used for the following reaction without any further purification.

Synthesis of 21

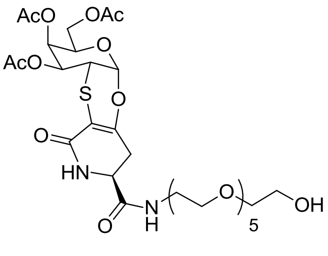

21

To a stirred solution of TBTU (0.234 g, 0.73 mmol) in dry DMF (7 mL), 4-methylmorpholine (80 µL, 0.73 mmol) was added. The solution was stirred for 20 minutes at rt, then a solution of **4** (185 mg) in dry DMF (3.6 mL) was added. The reaction mixture was stirred for 20' at rt then a solution of linker **5** (0.100 g, 0.360 mmol) in dry DMF (1.6 mL) was added. The reaction mixture was stirred for 1h at rt then concentrated to dryness. The crude was purified by flash chromatography on silica gel ($CHCl_3$/MeOH, 12/1 → 9/1) to give **21** (0.192 g, 73% over two steps) as a pale yellow oil.

$[\alpha]_D^{25}$: + 84.3 (c 0.65, $CHCl_3$)

^{1}H NMR (400 MHz, $CDCl_3$) δ: 7.56-7.54 (m, 1H, CON*H*CH_2), 6.99 (d, *J* = 2.8 Hz, 1H, CON*H*CH), 5.68 (d, $J_{1,2}$ = 2.8 Hz, 1H, H_1), 5.42 (dd, $J_{4,3}$ = 3.1 Hz, $J_{4,5}$ = 1.3 Hz, 1H, H_4), 5.00 (dd, $J_{3,2}$ = 11.6 Hz, $J_{3,4}$ = 2.8 Hz, 1H, H_3), 4.44 (at, *J* = 6.8 Hz, 1H, H_5), 4.22 (atd, *J* = 6.8 Hz, *J* = 2.4 Hz, 1H, $H_{5'}$), 4.17-4.00 (m, 2H, H_{6a}, H_{6b}), 3.74-3.50 (m, 24H, CH_2O, H_2, $H_{1''}$), 3.44-3.36 (m, 1H, $H_{1''}$), 2.99-2.93 (A part of an ABX system, J_{AB} = 16.7 Hz, J_{AX} = 7.3 Hz, 1H, $H_{4a'}$), 2.92-2.86 (B part of an ABX system, J_{BA} = 16.7 Hz, J_{BX} = 6.9 Hz, 1H, $H_{4b'}$), 2.79 (bs, 1H, OH), 2.16 (s, 3H, COCH_3), 2.06 (s, 3H, COCH_3), 2.02 (s, 3H, COCH_3)

^{13}C NMR (50 MHz, $CDCl_3$) δ: 170.4 (Cq), 170.2 (Cq), 170.0 (Cq), 169.9 (Cq), 164.3 (Cq), 154.8 (Cq), 97.5 (Cq), 96.0 (C_1), 72.9 (*C*H_2O), 70.7 (*C*H_2O), 70.4 (*C*H_2O), 69.6 (*C*H_2O), 69.1 (C_5), 67.4 (C_4), 66.2 (C_3), 61.8 (C_6), 61.7 ($C_{12''}$), 52.4 ($C_{5'}$), 40.0 ($C_{1''}$), 36.6 (C_2), 31.0 ($C_{4'}$), 20.7 (CO*C*H_3)

ESI-MS: *m/z* 745.28 $[M+Na]^+$

Elemental Analysis for $C_{30}H_{46}N_2O_{16}S$: calc. C 49.85, H 6.42, N 3.88; found C 49.79, H 5.68, N 4.22.

Synthesis of 22

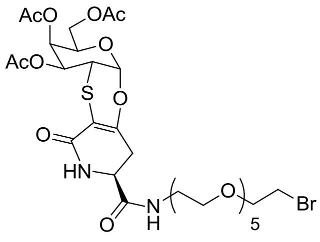

22

To a stirred solution of **21** (0.049 g, 0.068 mmol) in dry CH_2Cl_2 (2 mL), triphenylphosphine (0.025 g, 0.095 mmol) and CBr_4 (0.027 g, 0.081 mmol) were added. The mixture was stirred at rt overnight then concentrated to dryness. The crude was purified by flash chromatography on silica gel ($CHCl_3$/MeOH, 30/1 → 9/1) to give **22** (47 mg, 88%).

$[\alpha]_D^{25}$ = + 70.1 (c = 0.76, $CHCl_3$)

^{1}H NMR (400 MHz, $CDCl_3$) δ: 7.18 (t, $J = 5.2$ Hz, 1H, CON*H*CH_2), 6.73 (d, 1H, J = 2.4 Hz, 1H, CON*H*CH), 5.69 (d, $J_{1,2} = 2.7$ Hz, 1H, H_1), 5.43-5.42 (m, 1H, H_4), 5.01 (dd, $J_{3,2} = 11.6$ Hz, $J_{3,4} = 3.2$ Hz, 1H, H_3), 4.44 (at, $J = 6.4$ Hz, 1H, H_5), 4.19-4.13 (m, 3H, $H_{5'}$, H_{6a}, H_{6b}), 3.80-3.76 (m, 3H, CH_2O), 3.75-3.58 (m, 18H, CH_2O, H_2), 3.49-3.45 (m, 4H, $H_{12''}$, $H_{1''}$), 3.00-2.94 (A part of an ABX system, $J_{AB} = 16.7$ Hz, $J_{AX} = 7.4$ Hz, 1H, $H_{4a'}$), 2.92-2.86 (B part of an ABX system, $J_{BA} = 16.7$ Hz, J_{BX} = 6.8 Hz, 1H, $H_{4b'}$), 2.16 (s, 3H, $COCH_3$), 2.07 (s, 3H, $COCH_3$), 2.02 (s, 3H, $COCH_3$)

^{13}C NMR (100 MHz, $CDCl_3$) δ: 170.4 (Cq), 170.0 (Cq), 169.9 (Cq), 164.2 (Cq), 154.6 (Cq), 97.3 (Cq), 95.7 (C_1), 71.1 (CH_2O), 70.5 (CH_2O), 70.44 (CH_2O), 70.41 (CH_2O), 70.39 (CH_2O), 70.36 (CH_2O), 70.30 (CH_2O), 69.4 (CH_2O), 68.9 (C_5), 67.1 (C_4), 66.0 (C_3), 61.5 (C_6), 52.2 ($C_{5'}$), 39.9 ($C_{1''}$), 36.3 (C_2), 30.7 ($C_{4'}$), 30.4 ($C_{12''}$), 20.68 ($COCH_3$), 20.63 ($COCH_3$), 20.5 ($COCH_3$)

ESI-MS: *m/z* 785.31 $[M+H]^+$, 807.49 $[M+Na]^+$

Elemental Analysis for $C_{30}H_{45}BrN_2O_{15}S$: calc. C 45.86, H 5.77, N 3.57; found C 46.23, H 5.82, N 3.17.

Synthesis of 23

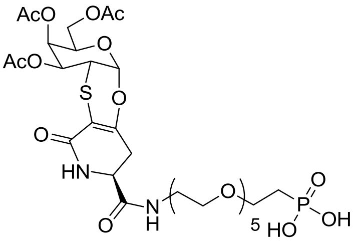

23

Compound **22** (0.094 g, 0.12 mmol) was dissolved in tris-trimethysilylphosphite (1.0 mL, 2.99 mmol) under N_2 atmosphere. The reaction mixture was warmed at 110°C and stirred for 18h, then concentrated to dryness to give **23** (95 mg, quantitative) as a glassy white solid.

$[\alpha]_D^{25}$ = + 77.9 (c 0.28, MeOH)

^{1}H NMR (400 MHz, $CDCl_3$) δ: 8.33 (bs, 1H, CON*H*CH), 7.80 (bs, 1H, CON*H*CH_2), 5.70 (d, $J_{1,2}$ = 2.8 Hz, 1H, H_1), 5.41 (bs, 1H, H_4), 4.98 (dd, $J_{3,2}$ = 11.6 Hz, $J_{3,4}$ = 3.0 Hz, 1H, H_3), 4.44 (at, J = 6.5 Hz, 1H, H_5), 4.22-4.13 (m, 3H, $H_{5'}$, H_{6a}, H_{6b}), 3.84-3.46 (m, 25H, CH_2O, H_2, $H_{1''}$, $H_{11''}$, O*H*, O*H*), 3.07-3.01 (A part of an ABX system, J_{AB} = 16.8 Hz, J_{AX} = 6.0 Hz, 1H, $H_{4a'}$), 2.98-2.92 (B part of an ABX system, J_{BA} = 16.8 Hz, J_{BX} = 7.3 Hz, 1H, $H_{4b'}$), 2.18-2.10 (m, 2H, $H_{12''}$), 2.15 (s, 3H, $COCH_3$), 2.06 (s, 3H, $COCH_3$), 2.02 (s, 3H, $COCH_3$)

^{13}C NMR (50 MHz, $CDCl_3$) δ: 170.4 (Cq), 170.2 (Cq), 169.9 (Cq), 169.8 (Cq), 165.8 (Cq), 156.1 (Cq), 96.1 (Cq), 95.8 (C_1), 70.3 (CH_2O), 69.9 (CH_2O), 69.7 (CH_2O), 69.3 (CH_2O), 68.8 (C_5), 67.1 (C_4), 65.9 (C_3), 65.2 (CH_2O), 61.5 (C_6), 51.8 ($C_{5'}$), 39.7 ($C_{1''}$), 36.1 (C_2), 29.9 (C4’), 27.79 (d, J_{C-P} = 137.2 Hz, $C_{12''}$), 20.6 ($COCH_3$)

^{31}P NMR (81 MHz, $CDCl_3$) δ: 29.84 (s)

HRMS: (*m/z*) calcd for $[M+H]^+$ $C_{30}H_{48}O_{18}N_2PS$ 787.23550, found 787.23590.

Synthesis of 3

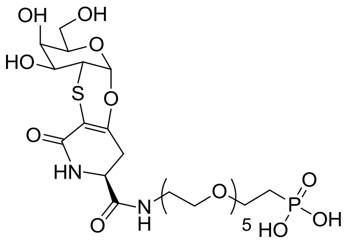

3

To a stirred solution of **23** (0.095 g, 0.120 mmol) in MeOH (10 mL), a 2.0 M solution (4 mL) of NH_3 in MeOH was added. The reaction mixture was stirred at rt for 24h, then concentrated to dryness to give **3** (79 mg) as a white hygroscopic solid. Phosphonate **3** was used for the following reaction without any further purification.

^{1}H NMR (400 MHz, CD_3OD) δ: 5.68 (d, $J_{1,2}$ = 2.8 Hz, 1H, H_1), 4.24 (at, J = 6.7 Hz, 1H, $H_{5'}$), 4.04 (at, J = 5.9 Hz, 1H, H_5), 3.97 (bs, 1H, H_4), 3.78-3.71 (m, 4H, H_{6a}, H_{6b}, CH_2O), 3.65-3.56 (m, 19H, CH_2O, H_3), 3.47-3.40 (m, 3H, $H_{1''}$, H_2), 2.99-2.93 (A part of ABX system, J_{AB} = 16.8 Hz, J_{AX} = 6.8 Hz, 1H, $H_{4a'}$), 2.81-2.75 (B part of ABX system, J_{BA} = 16.8 Hz, J_{BX} = 6.8 Hz, 1H, $H_{4b'}$), 1.95-1.87 (m, 2H, $H_{12''}$)

^{13}C NMR (50 MHz, CD_3OD) δ: 172.9, 167.6, 157.9, 98.3, 96.6, 74.9, 71.3, 71.1, 70.8, 70.3, 70.2, 68.3, 67.1, 62.5, 53.2, 40.5, 40.4, 31.9, 30.84 (d, J_{C-P} = 130.5 Hz);

^{31}P NMR (81 MHz, $CDCl_3$) δ: 20.04 (s)

HRMS: (*m/z*) calcd for $[M+H]^+$ $C_{24}H_{42}O_{15}N_2PS$ 661.20380, found 661.20272.

8.5 Synthesis of glucose derivative 24

Synthesis of 33

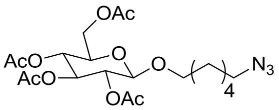

33

To an ice-cooled solution of **28** [5] (1.173 g, 2.38 mmol) and **25** [6] (0.452 g, 3.16 mmol) in CH_2Cl_2 (12 mL) trimethylsilyl trifluoromethanesulfonate (90 µL, 0.5 mmol) was added dropwise. The reaction mixture was stirred at 0°C for 1h, then neutralized with triethylamine (100 µL, 0.72 mmol), diluted with CH_2Cl_2 (230 mL) and washed with a saturated solution of NH_4Cl (2 x 10 mL) and brine (1 x 20 mL). The organic phase was dried over Na_2SO_4, filtered and concentrated to dryness. The crude product (1.55 g) was dissolved in CH_2Cl_2 (10 mL) and then DMAP (0.24 mmol, 30 mg), acetic anhydride (1.13 mL, 11.9 mmol) and pyridine (1 mL, 11.9 mmol) were added. The reaction mixture was stirred at rt for 1.5h, then diluted with CH_2Cl_2 (220 mL) and washed with a saturated solution of NH_4Cl (3 x 15 mL). The organic phase was dried over Na_2SO_4 filtered and concentrated to dryness. The crude was purified by flash column chromatography on silica gel (petroleum ether/ethyl acetate 3:1) to afford **33** (0.615 g, 55%) as a white sticky solid.

$[\alpha]_D^{25}$ = - 11.7 (c 0.31, $CHCl_3$)

^{1}H NMR (200 MHz, $CDCl_3$) δ: 5.24-4.93 (m, 3H), 4.48 (d, *J* = 8.0 Hz, 1H), 4.30-4.22 (A part of an ABX system, $J_{A,B}$ = 12.3 Hz, $J_{A,X}$ = 4.6 Hz, 1H), 4.16-4.08 (B part of an ABX system, $J_{B,A}$ = 12.3 Hz, $J_{B,X}$ = 2.6 Hz, 1H), 3.92-3.81 (m, 1H), 3.72-3.63 (m, 1H), 3.52-3.41 (m, 1H), 3.25 (t, *J* = 6.7 Hz, 2H), 2.07-1.99 (m, 12H), 1.64-1.51 (m, 4H), 1.39-1.31 (m, 4H).

^{13}C NMR (50 MHz, $CDCl_3$) δ: 170.7, 170.4, 169.5, 169.3, 100.9, 73.0, 71.9, 71.5, 70.0, 68.6, 62.1, 51.4, 29.3, 28.9, 26.5, 25.5, 20.8, 20.7.

Elemental analysis for $C_{20}H_{31}N_3O_{10}$: calc. C 50.73, H 6.60, N 8.87; found C 50.14, H 6.80, N 9.09.

Synthesis of 34

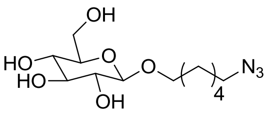

34

To a solution of **33** (0.579 g, 1.22 mmol) in CH_3OH (2.5 mL), 10 mL of an ammonia solution in methanol (2M) was added. The reaction mixture was stirred at rt for 18h and then concentrated to dryness. The crude was filtered on a pad of silica gel (eluent: ethyl acetate) to give compound **34** (0.365 g, quantitative) as a colorless sticky solid.

$[\alpha]_D^{25}$ = - 31.2 (c 0.9, $CHCl_3$);

^{1}H NMR (200 MHz, $CDCl_3$) δ: 5.89 (bs, 1H), 5.42 (bs, 1H), 5.15(bs, 1H), 4.67 (bs, 1H), 4.30 (d, *J* = 7.5 Hz, 1H), 3.92-3.78 (m, 3H), 3.65-3.47 (m, 3H), 3.39-3.24 (m, 4H), 1.73-1.53 (m, 4H), 1.46-1.36 (m, 4H).

^{13}C NMR (50 MHz, $CDCl_3$) δ: 102.9, 75.7, 73.5, 70.3, 69.5, 61.4, 51.4, 29.5, 28.8, 26.6, 25.5.

Elemental Analysis for $C_{12}H_{23}N_3O_6$: C 47.20, H 7.59, N 13.76; found C 47.32, H 7.89, N 13.76.

Synthesis of 30

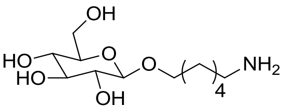

30

To a stirred solution of **34** (0.083 g, 0.27 mmol) in a mixture DMF:THF (1:10, 5.5 mL) triphenylphosphine (0.147 g, 0.56 mmol) was added. The reaction mixture was stirred at 45°C for 35', cooled to rt and then H_2O (40 µL, 2.22 mmol) was added. The solution was stirred at 45°C for 16h and then concentrated to dryness. The crude product **30** was used for the following reaction without any further purification.

Synthesis of 24

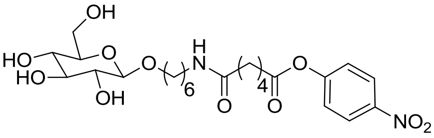

24

To a stirred solution of crude **30** (0.240 g) in DMF (0.4 mL), a solution of **26** [7] (0.423 g, 1.09 mmol) in DMF (2.25 mL) was added dropwise. The reaction mixture was stirred at rt for 1.5 h then concentrated to dryness. The crude **16** was treated with CH_3OH and then filtered. The filtrate was concentrated to dryness and the crude was purified by flash chromatography on silica gel (CH_2Cl_2/CH_3OH 9/1 → 8/1) to give compound **16** in 72% yield over 2 steps as a pale yellow sticky solid.

$[\alpha]_D^{25}$ = - 11.2 (c 0.52, CH_3OH)

^{1}H NMR (200 MHz, CD_3OD) δ: 8.32 (d, *J* = 9.2 Hz, 2H), 7.39 (d, *J* = 9.2 Hz, 2H), 4.26 (d, *J* = 7.9 Hz, 1H), 3.94-3.87 (m, 2H), 3.70-3.67 (m, 1H), 3.57-3.53 (m, 1H), 3.38-3.25 (m, 3H), 3.22-3.17 (m, 3H), 2.69 (t, *J* = 7.0 Hz, 2H), 1.93 (t, *J* = 6.9 Hz, 2H), 1.83-1.72 (m, 4H), 1.67-1.61 (m, 2H), 1.56-1.51 (m, 2H), 1.46-1.35 (m, 4H).

^{13}C NMR (50 MHz, CD_3OD) δ: 175.4, 172.4, 156.9, 146.6, 126.0, 123.8, 104.2, 78.0, 77.8, 75.0, 71.6, 70.6, 62.7, 40.3, 36.6, 34.5, 30.6, 30.3, 27.7, 26.7, 26.3, 25.2.

HRMS: (m/z) calcd for $[M+H]^+$ $C_{24}H_{37}N_2O_{11}$ 529.23919, found 529.23949.

8.6 Synthesis of amino-phosphonate linker 39

Synthesis of 34

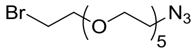

34

Monomesylatedhexaethyleneglycol **19** and monoazidehexaethyleneglycol **20** were prepared following a reported procedure [2]. To a solution of **20** (0.128 g, 0.42 mmol) in anhydrous CH_2Cl_2 (9 mL), CBr_4 (0.167 g, 0.50 mmol) and triphenylphosphine (0.155 g, 0.59 mmol) were added. The reaction mixture was stirred at rt overnight and then concentrated to dryness. The crude product was purified by flash chromatography on silica gel ($CH_2Cl_2/(CH_3)_2CO$ 10:1) to give product **34** (0.131 g, 85%) as a pale yellow oil.

^{1}H NMR (500 MHz, $CDCl_3$) δ: 3.81 (t, *J* = 6.4 Hz, 2H), 3.69-3.64 (m, 18H), 3.47 (t, *J* = 6.4 Hz, 2H), 3.38 (t, *J* = 5.2 Hz, 2H).

^{13}C NMR (125 MHz, $CDCl_3$) δ: 71.3, 70.85, 70.83, 70.81, 70.78, 70.73, 70.6, 50.8, 30.4.

ESI-MS: *m/z* 392.11 $[M+Na]^+$, 408.10 $[M+K]^+$

Synthesis of 37

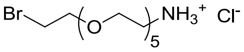

37

To a solution of **34** (50 mg, 0.13 mmol) in distilled THF (4 mL), an aqueous solution of HCl (4.9 M, 55 µL) and 10% Pd/C (58 mg, 0.027 mmol) were added. The mixture was stirred at rt under H_2 atmosphere for 2 h and then filtered through a pad of Celite®. Evaporation of the solvent under vacuum gave product **37** (51 mg, quantitative) as a green-yellow oil.

^{1}H NMR (500 MHz, CD_3OD) δ: 3.85-3.79 (m, 2H), 3.77-3.72 (m, 2H), 3.71-3.60 (m, 16H), 3.57-3.48 (m, 2H), 3.15 (br, 2H).

^{13}C NMR (125 MHz, CD_3OD) δ: 72.3, 71.4, 71.3, 71.2, 71.1, 70.9, 67.9, 40.7, 31.5.

ESI-MS: *m/z* 344.25 $[M+H]^+$

Synthesis of 38

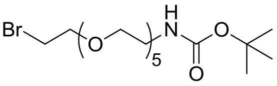

38

To a solution of **37** (0.103 g, 0.30 mmol), and di-*tert*-butyl dicarbonate (0.160 g, 0.73 mmol) in distilled THF, DIPEA (53 µL, 0.30 mmol) was added. The reaction mixture was stirred at rt for 6h and then diluted with CH_2Cl_2 and washed with brine (3x10 mL) and water (3x10 mL). The organic phase was dried over Na_2SO_4, filtered and concentrated to dryness. The crude was purified by flash column chromatography on silica gel (CH_2Cl_2/$(CH_3)_2CO$ 4:1) to afford **38** (72 mg, 54%) as a pale yellow oil.

^{1}H NMR (500 MHz, $CDCl_3$) δ: 3.83 (t, *J* = 6.4 Hz, 2H), 3.71-3.61 (m, 18H), 3.55 (t, *J* = 5.1 Hz, 2H), 3.49 (t, *J* = 6.4 Hz, 2H), 3.38-3.26 (br, 1H), 1.46 (s, 9H).

^{13}C NMR (125 MHz, $CDCl_3$) δ: 156.1, 79.2, 71.5, 71.3, 70.8, 70.7, 70.6, 70.3, 40.5, 30.4, 28.5.

ESI-MS: *m/z* 466.15 $[M+Na]^+$, 482.05 $[M+K]^+$

Synthesis of 39

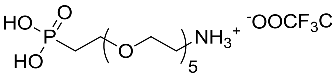

39

Tris(trimethylsilyl) phosphite (0.9 mL, 2.7 mmol) was added to product **38** (60 mg**,** 0.13 mmol), and the reaction mixture was stirred at 100°C, for 48h. The mixture was cooled to rt and concentrated to dryness. The colourless oil obtained was then dissolved in CH_2Cl_2 (5 mL) and TFA (210 µL, 27 mmol) was added. The solution was stirred at rt for 2h and then concentrated to dryness to afford **39** (62 mg, quantitative) as a colourless oil.

^{1}H NMR (500 MHz, CD_3OD) δ: 3.82-3.75 (m, 4H), 3.74-3.64 (m, 16 H), 3.18-3.14 (m, 2H), 2.12-2.05 (m, 2H).

^{13}C NMR (125 MHz, CD_3OD) δ: 71.4, 71.3, 71.26, 71.21, 71.1, 70.9, 70.8, 67.9, 66.7, 40.5, 39.6, 28.5.

^{31}P NMR (200 MHz, CD_3OD) δ: 24.24 (s)

HRMS: (*m/z*) calcd for $[M+H]^+$ $C_{12}H_{29}NO_8P$ 346.16253, found 346.16154.

8.7 Biological tests on macrophages activation

Biological tests on macrophages activation were performed in collaboration with Prof. G. Lombardi, Dipartimento di Scienze del Farmaco, Università del Piemonte Orientale "Amedeo Avogadro".

To measure the biological effects of MNPs, either functionalized or not functionalized with the α-Tn mimetic antigen, the concentration of each compound was expressed as μg/ml. To allow an easy comparison among compounds the correspondence between mass and mole concentrations was also calculated (see Table 8.2).

	Compound (μg/ml)	**α-Tn-epitope mimetic (μM)**
3	1	1.5
CMNPs	1	—
GMNPs	1	0.2

Table 8.2 : Relationship between mass and mole concentrations of the tested compounds

Cell culture

The RAW 264.7 murine macrophage cell line (ATCC TIB-71; American Type Culture Collection, Manassas, VA, USA) was cultured in high glucose (4.5 g/l) Dulbecco's modified Eagle's medium (DMEM) supplemented with 10% heat-inactivated fetal bovine serum (FBS), 2mM L-glutamine, 100 IU/ml penicillin and 100 μg/ml streptomycin (Lonza, Milan, Italy) and kept in a 37 °C incubator with 5% CO_2. Cells were grown in 75-cm^2 flasks and sub-cultured by scraping when they reached 90% confluence with a 1:5 or 1:10 ratio in fresh medium. Before each experiment, viable cell count was assessed by trypan blue staining; thereafter cells were seeded and rendered quiescent by 18h serum deprivation.

Limulus amebocyte lysate (LAL) assay

LPS levels in each compound were measured in duplicate in serial 1:10 dilutions of each sample made with pyrogen-free water using a chromogenic LAL assay (Lonza, Basel, Switzerland), according to the manufacturer's protocol. The sensitivity of the LAL assay was 0.01 ng/ml.

MTT assay

Cell viability was measured by the 3-(4,5-dimethylthiazol-2-yl)-2,5-diphenyl-tetrazolium bromide (MTT) assay. Briefly, RAW 264.7 cells were seeded in 24-well plates and treated with increasing concentrations (0.01-30 μg/ml) of **3**, **PEMNPs**, **CMNPs**, **GMNPs** or **GlcMNPs** for 24, 48 and 72 h at 37° C in a 5% CO_2 humidified incubator. The percentage of cell viability was calculated as (x × 100)/y, where x, and y were the absorbance read in compound-treated, and compound-untreated cells, respectively.

Calcein-AM assay

RAW 264.7 cells were labelled with 1 μM Calcein-AM (CAM) (Molecular Probes, Invitrogen) in serum-free PBS for 15 min at 37° C in the dark. After being washed, labelled cells were seeded in 24-well plates and allowed to adhere overnight at 37° C in a humidified incubator. The day after, RAW 264.7 cells were treated with increasing concentrations (0.01-30 μg/ml) of **3**, **PEMNPs**, **CMNPs**, **GMNPs** or **GlcMNPs** for 24, 48 and 72 h at 37° C in a 5% CO_2 humidified incubator. After incubation time the cells of each well were harvested, washed, labelled with propidium iodide (PI), and the viability was measured by flow cytometry. Lived cells were identified as CAM^{high}/PI^- population whereas dead cells were CAM^{low}/PI^+. Viability was calculated by FACSDiva software and expressed as the percentage of CAM^{high}/PI^- population relative to untreated cells.

Trypan blue-exclusion assay of cell viability

RAW 264.7 cells were seeded in 24-well plates and treated with increasing concentrations (0.01-30 μg/ml) of **3**, **PEMNPs**, **CMNPs**, **GMNPs** or **GlcMNPs**, for 24, 48 and 72 h at 37° C in a 5% CO_2 humidified incubator. After incubation time cells were harvested, stained with a trypan blue solution and counted under an inverted microscope. The percentage of cell viability was calculated as (x × 100)/y, where x, and y were the number of live and total cells in the same sample, respectively.

Qualitative study of MNPs uptake

RAW 264.7 cells (5×10^4 cells/well) were allowed to adhere overnight on sterile glass cover slips in 24-well culture plates and treated with **PEMNPs**, **CMNPs**, **GMNPs** or **GlcMNPs** (30 μg/ml) in complete medium for 24h at 37°C, 5% CO_2. The cover slips were washed twice with ice-cold PBS to remove unbound MNPs and cells were fixed with 4% paraformaldehyde for 15 min at 4° C. After two additional PBS washing, cells on the cover slips were stained with fresh prepared Prussian blue reagent (2% potassium ferrocyanide [Sigma Aldrich]/12% HCl, 1:1, v/v) for 30 min. The cells were washed five times with PBS, and subsequently the cover slips were mounted on glass slides by SlowFade® reagent (Invitrogen, Milano, Italy). Cells were then observed by an inverted optical microscope (objective x 40) with an integrated camera (Motic AE2000 with integrated Moticam 3.0).

Quantitative study of MNPs uptake

RAW 264.7 cells were seeded (1 x 10^5 cells/well) in 12-well culture plates and treated with **3**, **PEMNPs**, **CMNPs**, **GMNPs** or **GlcMNPs** (30 μg/ml) for 24 h at 37° C in a 5% CO_2 humidified incubator. Following incubation, cells were washed twice with cold PBS to remove unbound MNPs, gently scraped from the culture plates on ice, and centrifuged (900 rpm, 5 min, 4°C). Cell pellets were resuspended in 200 μl PBS containing 2% FBS and analyzed by FACScalibur (FACS-Vantage, BD Bioscience, Milan). A total of 5000 viable cells were collected for each sample. For calculation cell debris and free particles were excluded by an electronical gate containing RAW 264.7 cells of all size and granularities in a FSC-SSC-histogram. Univariant histograms of SSC determined the mean of cell granularity used as measure of uptake by RAW 264.7 cells. Data were analyzed by using FACSDiva software (BD Bioscience, Milan).

For uptake time-course determination, RAW 264.7 cells were seeded (1 x 10^5 cells/well) in 12-well culture plates and incubated with **3**, **PEMNPs**, **CMNPs**, **GMNPs** or **GlcMNPs** (30 μg/ml) for up to 72 h at 37° C in a 5% CO_2 humidified incubator. At different incubation times (1, 3, 6, 18, 24, 48 and 72h) cell samples were harvested, prepared and analyzed by FACS, as described above.

To explore the relationship between cellular uptake and compound concentration RAW 264.7 cells were seeded in 12-well culture plates and incubated with increasing concentrations (0.1-30 μg/ml) of **3**, **PEMNPs**, **CMNPs**, **GMNPs** or **GlcMNPs** for 24, 48, and 72 h at 37° C in a 5% CO_2 humidified incubator. Following incubation cell samples were harvested, prepared and analyzed by FACS, as described above.

RT-PCR

RAW 264.7 cells were seeded (1 x 10^6 cells/well) in 6-well culture plates and treated with increasing concentrations (1-30 μg/ml) of **3**, **PEMNPs**, **CMNPs**, **GMNPs** or **GlcMNPs** for 24 h at 37° C in a 5% CO_2 humidified incubator. Bacterial LPS (0.1 μg/ml) -treated and -untreated cells were used as positive and standard controls, respectively, for RT-PCR analysis. Total RNA was isolated using the GenElute^{TM} mammalian total RNA kit (Sigma Aldrich, Milan) and reverse-transcribed to cDNA using ThermoScript RT-PCR^{TM} kit (Invitrogen, Milan, Italy), according to the manufacturer's instructions. For amplification, 3 μl of cDNA were added to GoTaq FlexiDNA Polymerase (Promega, Milan, Italy) in 25 μl reaction buffer, containing 0.5 μM of forward and reverse primers (Table 1S, Supplementary Information). Amplification products were resolved in 1% agarose gel by electrophoresis and visualized with ethidium bromide. Signals were quantified with densitometric analysis software (NIH Image 1.32; Bethesda, MD, USA). Data were expressed as the ratio of the signals obtained for each gene in one sample divided by that obtained for the reference gene (mouse β-actin) in the same sample.

TNF-α release

RAW 264.7 cells were seeded in 24-well culture plates and treated with increasing concentrations (0.1-30 μg/ml) of **3**, **PEMNPs**, **CMNPs**, **GMNPs** or **GlcMNPs** for 24, 48 and 72 h at 37° C in a 5% CO_2 humidified incubator. Bacterial LPS (0.1 μg/ml)-treated cells, and -untreated cells were used as positive and standard controls, respectively, of TNF-α release. At the end of each experiment, supernatants were collected and stored at −20 °C until assays. The amounts of TNF-α in cell culture media were assayed using enzyme-linked immunosorbent assay (ELISA) kits (Biolegend, San Diego, USA), according to the manufacturer's instructions. The concentrations of TNF-α in the samples were determined by extrapolation from specific reference standard curves.

Statistical analysis

Results were expressed as means ± SEM of at least three independent experiments run in triplicate. Statistical significance was evaluated by the one-way ANOVA followed by Student's t-test for unpaired populations (Graph Pad Software, Inc., San Diego, USA). Differences were considered statistically significant when $p \leq 0.05$.

8.8 Structural characterization of MNPs

X-ray diffraction (XRD)

Powder X-ray diffraction (XRD) measurements were carried out using a Bruker D8 Advance diffractometer equipped with Cu Kα (1.54178 Å) radiation and operating in θ−2θ Bragg−Brentano geometry at 40 kV and 40 mA. Lattice parameters were evaluated on averaging over (400), (511) and (440) peaks. The determination of the mean crystallite diameter, *d*, was performed using the Scherrer equation,$d = (0.9\lambda)/(\beta \cos\theta)$, where λ is the wavelength of the incident X-ray (1.54178 Å), θ the diffraction angle, and β the full-width at half-maximum. The quantification of the phase percentage was obtained analyzing the diffraction pattern by the Rietveld method with TOPAS software.

TEM

Average diameter and size distribution of the MNPs were determined by transmission electron microscopy (TEM), using a CM12 PHILIPS transmission electron microscope operating at 100 kV. Samples were prepared by drop drying a dilute suspension of MNPs in the proper solvent (heptane, hexane or water) onto 200 mesh carbon-coated copper grids. The recorded micrographs were further analyzed with the Image Pro-Plus® and ImageJ® software. The mean diameter and size distribution of each sample were obtained from a statistical analysis over ca. 300-700 MNPs depending on the sample.

ICP-AES

The determination of Fe, S and P content was performed on a Optima 2000 Perkin Elmer Inductively Coupled Plasma (ICP) Optical Emission Spectrophotometry (OES) Dual Vision. Before analysis, about 1 mg of sample was weighted in PE vials and digested on hot plate at 80 °C for 24 hours with 2 mL of aqua regia (HCl suprapure grade and HNO_3 sub-boiled in 3:1 ratio) and 0.05 mL of H_2O_2 suprapure grade. After the digestion, the samples were diluted to 20 mL with ultrapure water ($\geq$18 MΩ).

FT-IR

FTIR spectra were collected on a Perkin Elmer Spectrum BX. The sample powders were ground with KBr and pressed into a pellet.

8.9 Magnetic and hyperthermic characterization

Magnetic Measurements

Magnetic measurements were performed using a Quantum Design MPMS SQUID magnetometer operating in the 1.8 – 400 K temperature range with a magnetic field up to ± 5 T. Measurements on **IAMNP2** were performed on a dispersion in heptane hosted in a hydrophilic capsule. For the other samples, powder MNPs were hosted in a Teflon sample holder and then pressed in a pellet. All data were corrected for the diamagnetic contribution of the sample holder and of the solvent, which were separately measured. ZFC-FC curves were recorded in the 2.5 – 300 K temperature range using a 5 mT probe field. AC susceptibility curves were recorded with a 24 A/m field amplitude between 2.5 and 300 K in the 1 – 1000 Hz frequency range.

Hyperthermic characterization

In paragraph 2.2 we described how to evaluate SAR values from calorimetric measurements and here is described the experimental setup used in this work, that is based on a home-assembled instrument composed of different elements (Figure 8.5):

- A power supply of 6 kW working in the frequency range of 50 – 400 kHz;
- an induction coil connected to the power supply and cooled with water. The working frequency can be selected by selecting the proper combination of coil (there are two different coils, made by 2 and 6 windings, respectively) and capacitor;
- a water cooling system;
- an optical fiber thermometer connected to a digital temperature recorder (Fotemp)

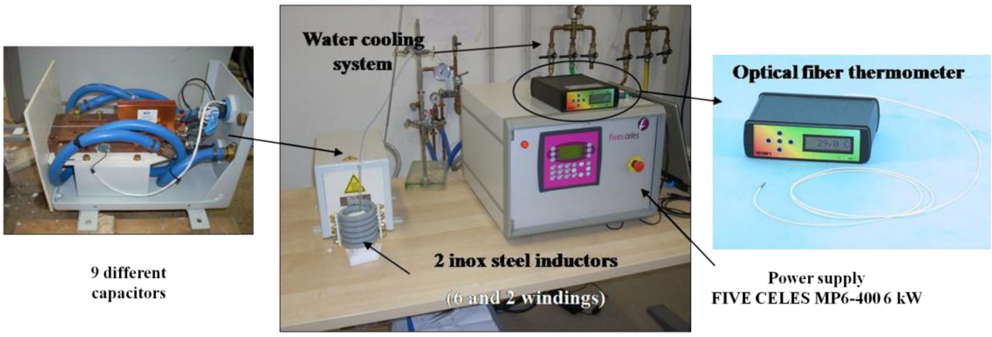

Figure 8.5 : Power supply MP6-400 6kW®, Fives Celes Inc. and optical fiber thermometer.

Measurements are performed on ca. 400 mL of solution. Typical concentrations are in the range 1-10 mg/mL of metal ion. For the temperature measurement, the optical fiber is dipped in the sample through a hole in the screw cap of the plastic sample holder, which is hosted in a polystyrene support. In order to achieve a better thermal isolation from the surroundings and minimize the heat exchange the polystyrene holder is placed inside the internal cavity of a thermostated system. It is composed by a glass container in which ethylene glycol flows, while a thermostat station keeps the desired temperature (Figure 8.6).

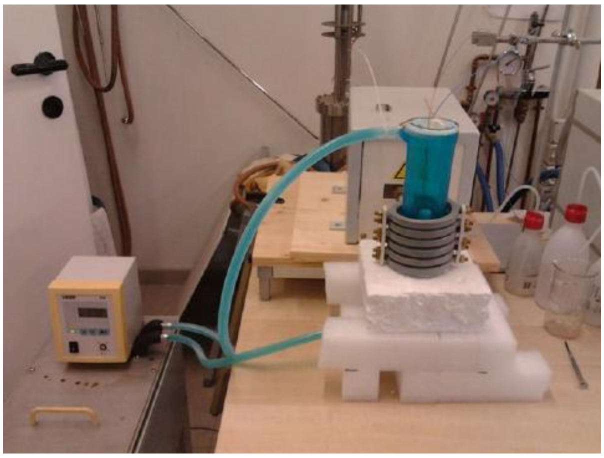

Figure 6 : Ethylene glycol thermostated system.

8.10 Characterization of organic compounds

NMR characterization

NMR spectra were recorded on a Varian Gemini 200 MHz, on a Varian Gemini 300 MHz, on a Varian Inova 400 MHz, on a Varian Mercury 400 MHz, and on a Bruker Avance 500 MHz spectrometers. The NMR spectra were referenced to solvent.

ESI-MS

Mass spectra were recorded on an LCQ-FLEET ion trap Thermo Fischer mass spectrometer. ESI-MS analysis was performed both in positive or negative ion mode.

Optical rotation

Optical rotation measurements were carried out on a Jasco DIP-370 polarimeter.

Melting point

Melting points were measured on a Melting point Büchi 510.

References

[1] S. Sun, H. Zeng, *J. Am. Chem. Soc.* **2002**, *124*, 8204.

[2] F. Menger, M. Hailing Zhang, *J. Am. Chem. Soc.* **2006**, *128*, 1414.

[3] J. Jimenéz-Barbero, E. Dragoni, C. Venturi, F. Nannucci, A. Ardà, M. Fontanella, S. André, F.J. Cañada, H.-J. Gabius, C. Nativi, *Chem. Eur. J.* **2009**, *15*, 10423.

[4] F. Venturi, C. Venturi, F. Liguori, M. Cacciarini, M. Montalbano, C. Nativi, *J. Org. Chem.* **2004**, *69*, 6153.

[5] R. R. Schmidt, K.-H. Jung, in *Preparative Carbohydrate Chemistry* Ed. S.Hanessian Marcel Dekker, New York, **1997**, p.283.

[6] A. Arcangeli, L. Toma, L. Contiero, O. Crociani, L. Legnani, C. Lunghi, E. Nesti, G. Moneti, B. Richichi, C. Nativi, *Bioconjugate Chem.* **2010**, *21*, 1432.

[7] X. Wu; C.-C. Ling; D. Bundle, *Org. Lett.*, **2004**, *6*, 4407.